Durham E-Theses

Photoelectron spectroscopy of (C6F6)n- and (C6F6)I- clusters in a novel instrument

ROGERS, JOSHUA,PETER

How to cite:

ROGERS, JOSHUA,PETER (2017) *Photoelectron spectroscopy of (C6F6)n- and (C6F6)I- clusters in a novel instrument*, Durham theses, Durham University. Available at Durham E-Theses Online: http://etheses.dur.ac.uk/12364/

Use policy

The full-text may be used and/or reproduced, and given to third parties in any format or medium, without prior permission or charge, for personal research or study, educational, or not-for-profit purposes provided that:

- a full bibliographic reference is made to the original source
- a link is made to the metadata record in Durham E-Theses
- the full-text is not changed in any way

The full-text must not be sold in any format or medium without the formal permission of the copyright holders.

Please consult the full Durham E-Theses policy for further details.

Academic Support Office, Durham University, University Office, Old Elvet, Durham DH1 3HP
e-mail: e-theses.admin@dur.ac.uk Tel: +44 0191 334 6107
http://etheses.dur.ac.uk

Photoelectron spectroscopy of $(C_6F_6)_n^-$ and $C_6F_6 \cdot I^-$ clusters in a novel instrument

A thesis submitted for the degree of
Doctor of Philosophy in Chemistry

Joshua P Rogers
Ustinov College
University of Durham

7th November 2017

The capabilities of a new photoelectron spectrometer are characterised in the study of $(C_6F_6)_n^-$ and $C_6F_6 \cdot I^-$ clusters. The photoelectron spectrometer consists of a series of vacuum chambers that facilitate a molecular beam of gas-phase anions. These anions and clusters are generated at the point of intersection between an electron beam and the supersonic expansion produced by a high temperature Even-Lavie pulsed valve. The anions are extracted orthogonally and mass-separated in a Wiley-McLaren time-of-flight mass spectrometer. The analyte is addressed by a laser pulse produced by either a tuneable nanosecond OPO for one-photon frequency-resolved measurements or a femtosecond pump-probe regime for two-photon time-resolved measurements. The kinetic energy of the resulting photoelectrons are measured in a velocity-map imaging spectrometer.

$C_6F_6^-$ is of interest due to the prediction that it ought to host a meta-stable binding mode of the excess electron known as a correlation-bound state (CBS). Similar to other non-valence binding modes, such as the dipole-bound state, this CBS is thought to act as a doorway state in the mechanism of low energy electron capture.

The CBS is characterised by a large and diffuse orbital in which the excess electron is bound primarily through charge:induced-dipole interactions with the molecule's valence orbital system. In the CBS, $C_6F_6^-$ is predicted to adopt a planar geometry like that of the neutral species, in contrast to the buckled geometry adopted when the excess electron occupies a valence orbital.

Frequency- and time-resolved measurements of the anion were made in an effort to generate and observe the CBS. Initially, frequency resolved measurements of $(C_6F_6)_n^-$ revealed a vertical detachment energy of 1.60 ± 0.07 eV for n = 1, increasing by ~ 200 meV per additional cluster unit up to $n = 5$. The broad shape of the direct detachment peak confirms the disparity in geometry between the anion and neutral species. However, no evidence of the CBS was evident in these data.

In subsequent explorations, an in-situ electron donor was employed to mimic the electron impact process. An I^- ion was introduced to the neutral C_6F_6 molecule to produce clusters of $C_6F_6 \cdot I^-$. Frequency-resolved measurements of this cluster revealed a mechanism for electron loss below the threshold for the single-photon direct detachment process. This suggested the presence of a charge-transfer channel centred around $hv = 3.3$ eV.

Time-resolved measurements of $C_6F_6 \cdot I^-$ confirmed the presence of the charge-transfer state and revealed an instantaneous and coherent transfer of the electron onwards into the valence orbital system of the C_6F_6 molecule. This transfer of charge causes the molecule to vibrate as its geometry changes from planar to buckled. The oscillations observed in the photoelectron spectra are coherent and sinusoidal and have a frequency of 121 ± 2 cm^{-1}. This compares very favourably to the frequency of 122 cm^{-1} calculated by time-dependent density functional theory for the bending mode of C_6F_6 along the coordinate between the planar and buckled geometries. I argue that this charge-transfer state exhibits the predicted characteristics of a CBS.

Contents

Acronyms & Abbreviations

ADE adiabatic detachment energy

$(\mathbf{H_2O})_n^-$ water cluster anions

BBO β-barium borate

BNC bayonet Neill-Concelman

CBS correlation-bound state

CCD charge-coupled device

CF conflat

CTS charge-transfer state

CTTS charge-transfer to solvent

CW continuous wave

DBS dipole-bound state

DEI Directed Energy Inc

DFT density functional theory

DNA deoxyribonucleic acid

EA electron affinity

$\mathbf{e}_{\mathrm{aq}}^-$ hydrated electron

eBE electron binding energy

eKE electron kinetic energy

FFT fast Fourier transform

FWHM full-width half-maximum

HOMO highest occupied molecular orbital

HV high voltage

IR infrared

LED light emitting diode

LUMO lowest unoccupied molecular orbital

MCP microchannel plate

MS mass spectrometry

m/z mass:charge ratio

NMR nuclear magnetic resonance

NVR no-voltage return

OPO optical parametric oscillator

PAD photoelectron angular distribution

PES photoelectron spectroscopy

PID proportional-integral-derivative

PLA polylactic acid

PMT photomultiplier tube

POP 8.5 polar onion-peeling algorithm v8.5

QBS quadrupole-bound state

RGA residual gas analysis

SHV safe high voltage

SO-HOMO singly-occupied highest occupied molecular orbital

TD-DFT time-dependent density functional theory

TOF time-of-flight

turbo turbomolecular pump

UV ultraviolet

VBS valence-bound state

VDE vertical detachment energy

VI virtual instrument

VMI velocity-map imaging

Chapter 1

Introduction

The question of how individual molecules capture electrons to form anions is of growing interest in a number of contexts. Non-valence binding modes been invoked to explain low energy electron damage to DNA in the field of radiation chemistry[1,2]; it has been suggested that they play a critical role in reaction networks in the interstellar medium and have even been assigned to certain spectral features[3,4]; and non-valence binding modes have been proposed as important intermediates in the formation of chemically significant reagents in the upper atmosphere[5] and on reactive interfaces such as water clusters[6,7]. A growing body of work is providing evidence for mechanisms that require non-valence binding modes of the excess electron to provide the initial interaction that subsequently results in the production of valence-bound molecular anions. In order to understand the role of these non-valence electronic states, it is first necessary to understand some of the properties of molecular anions more generally.

1.1 Molecular anions

Each electron within the valence system of a neutral molecule experiences a net attractive potential. This is due to the fact that each electron sees one more proton than other electrons in the molecule. At long range, when the electron-electron exchange interaction is negligible, the outermost electron in a neutral molecule experiences a purely Coulombic attractive potential, V, that scales with $V \propto -Ze^2/r$, where Z is the + 1 net positive charge, e is the electronic charge and r is its radial separation. Given that its operator contains the Laplacian, ∇^2, the radial kinetic energy, r^{-2}, decreases faster than the attractive potential, r^{-1}, and therefore neutral molecules are able to host an infinite series of bound electronic excited states[8].

When a free electron approaches a neutral molecule, it experiences a potential that arises from various interactions with different parts of the molecule. At long range, there is a net zero Coulomb interaction as there is no net charge on the molecule. However, there is a small attractive potential that arises from interactions with the molecule's permanent dipole ($V_{\text{dipole}} = -\mu e \cos(\theta)/r^2$), quadrupole ($V_{\text{quad}} = -Q(3\cos^2(\theta) - 1)/3r^3$) and induced-dipole ($V_{\text{correlation}} = -\alpha/r^4 - \beta/r^8$), where μ is the magnitude of the dipole moment of the molecule, Q is its quadrupole moment, α is the polarisability of a spherically symmetrical molecule[9], r and θ are the polar spatial coordinates and β is a fitting parameter.

At close range, the Coulomb interactions with the nuclei and valence electrons, which were indistinguishable at long range, become distinct. The repulsive Coulombic and exchange interactions with the valence electrons form a steep potential barrier into which the electron cannot penetrate. However, the electron may experience an attractive potential if there are regions of space around the molecule where Coulombic interaction with the nuclei is not completely shielded or negated by repulsive interactions with the other valence electrons. Therefore, whether or not an excess electron can become part of the valence system of a molecule to form a valence-bound state (VBS) depends on the shape and size of the molecule and its existing valence electron system. For this reason, not every molecule is able to form a stable anion and those that do typically have a low electron affinity (EA) (< 1.0 eV, although a few have an EA of up to 4.0 eV)[8].

In neutral molecules, there is an infinite series of bound electronic excited states. At high energies, they are referred to as Rydberg states[10], which converge to the ionisation energy. This infinite series is a consequence of the kinetic energy ($T \propto r^{-2}$) decreasing quicker than the Coulombic attraction ($V \propto r^{-1}$) at long range. Conversely, the outermost electron in an anion experiences no net Coulomb attraction at long range but rather the potential it experience arises from charge:dipole, charge:quadrupole and charge:induced-dipole interactions ($V \propto r^{-2}, r^{-3}, r^{-4}$ respectively). Each of these attractions falls away at least as fast as, if not faster than, the kinetic energy. Therefore, far from an infinite series, bound electronic excited states of anions are relatively rare owing to the relatively small energy with which the excess electron is bound, even in the ground state.[8].

There are a number of challenges to consider when studying molecular anions. The low EA of most molecules generates a number of complications, including:

- Bound excited states of the anion may only be bound by a few vibrational levels, which may lead it to couple to a neutral state, resulting in vibration-induced autodetachment of the excess electron[11]. Therefore, it can be difficult to generate and maintain anion excited states for long enough to probe experimentally.
- The EA of anions may change dramatically – even from negative to positive – in the presence of a stabilising solvent. The study of isolated gas-phase molecular anions may bear no resemblance to chemically important solution-phase species and vice-versa.
- With regard to theoretical treatment by density functional theory (DFT) and *ab initio* calculations, low binding energies give rise to extended charge distributions that require the use of large basis sets or custom diffuse orbitals[8]. However, a detailed discussion of calculations and theoretical methods will not be made here.

1.1.1 Non-valence binding modes

1.1.1.1 The dipole-bound state

The question of electron capture by neutral molecules necessitates the consideration of long-range potentials between the free electron and the neutral species. In the absence of a Coulombic potential, the interactions that remain are comparatively weak at long-range. The longest-range is the charge:dipole interaction, which falls away according to r^{-2}. Indeed for molecules with a sufficiently large dipole moment, it has been demonstrated that this interaction alone is sufficient to bind an excess electron in a state referred to as a dipole-bound state (DBS). Due to its low binding energy, the DBS is characterised by the excess electron occupying a large and diffuse orbital, largely external to the valence orbital system, providing minimal perturbation to the nuclear and valence structure and usually localised around the end of the molecule that contains the positive end of the dipole moment[12].

The theoretical absolute minimum dipole moment required for binding an excess electron in a s- or σ-like DBS is 1.625 D[13–15]. This result was derived from calculations that modelled the purely attractive potential experienced by an electron in the field generated by a point-dipole and predicts an unphysical infinite series of bound DBSs. It is only when the shorter-range repulsive potential of the valence system is accounted for that the number of bound states becomes finite[16,17]. Similarly, when appropriate corrections are applied to the Born-Oppenheimer approximation and vibrational and rotational motion of the molecule is considered[18], the minimum dipole moment required for a stable DBS increases by a few tenths of a Debye and varies depending on the moment of inertia of the molecule[12]. Calculations incorporating these corrections better reflect real systems but still leave much to be desired with respect to predicting the binding energy of the excess electron. Despite the spatial segregation of the excess electron in the DBS and the molecule's valence electrons, dispersion interactions between them have been shown to be important enough to require consideration in order to calculate quantitatively accurate binding energies[19,20].

The DBS is a well-documented phenomenon investigated in many theoretical and experimental studies. It was initially postulated by theoretical investigations[21–26] and the first experimental evidence was provided by electron scattering studies in the range $0.0 \leq$ electron kinetic energy (eKE) ≤ 10.0 eV[27,28]. Resonances were observed in both the elastic and vibrational cross sections of CO, HCl and HF, implying temporary binding of the electron by the dipole moment of the molecule. Subsequent photodetachment studies on the molecular anions of acetophenone[29], substituted acetophenone enolate[30] and acetaldehyde enolate[31,32] revealed a series of narrow peaks in the photodetachment cross-section just above threshold. These were attributed to resonances with DBSs that undergo autodetachment, which will be discussed in Section 1.2.1.2.

More recently, the DBS has been shown to participate in electron capture in molecules that are able to host both a DBS and VBS of the excess electron. This has been demonstrated by a series of studies revealing it to be an intermediate in intra-cluster charge-transfer mechanisms[1,33].

1.1.1.2 The quadrupole-bound state

In the absence of a permanent dipole, an excess electron can still be bound in a non-valence state by shorter-range interactions with the quadrupole moment, Q, of the molecule. This is known as a quadrupole-bound state (QBS). Like the DBS, the stronger the moment, the larger the binding energy. However, unlike the DBS, the QBS does not have a minimum moment required in order to bind the excess electron in the case of a point-quadrupole core. Instead, because of the r^{-3} attraction between the excess electron and Q, whether or not a stable QBS can form is not just dependent on the magnitude of Q. Rather, it also depends on the extent of the valence electron system, r_c, of the molecule, which constitutes the repulsive core of the overall potential that the excess electron experiences. In order for the electron to experience an attraction beyond r_c, Q must be large. For a given Q, the smaller r_c is, the more likely the molecule will host a stable QBS. Similarly, for a given r_c, the larger Q is, the more likely a stable QBS will occur.

However, identifying a QBS is less straightforward than for a DBS. $(BeO)_2$ has been predicted to host a QBS[34,35] but the extent to which the binding of the excess electron is attributed to the charge:quadrupole interaction is disputed[8]. As with the DBS, physically meaningful binding energies can only be calculated when dispersion interactions between the excess electron and the valence system are considered. The first experimental observation of a QBS was documented recently in cryogenically cooled 4-cyanophenoxide anions[36].

1.1.1.3 The correlation-bound state

In the absence of a sufficiently large permanent dipole or quadrupole moment, an excess electron may still be bound to a molecule in a non-valence state by dispersion forces. This is known as a correlation-bound state (CBS). The strength of the charge:induced-dipole interaction between the excess electron and the molecule is determined not by a multipole moment but rather by the polarisability of the molecule. The potential modelled for this interaction varies. In some studies[9] it has a r^{-4} or r^{-6} dependency but is invariably shorter-range than even the charge:quadrupole interaction. Therefore, in order to form a CBS, the extent of the repulsive core of the overall potential must be smaller than the range of the attractive dispersion interaction.

Similar to the DBS and QBS, the excess electron in the CBS is weakly-bound and resides in a large and diffuse orbital that overlaps very little with the valence orbital system. However, unlike in the DBS, the large orbital of the CBS is not localised at the end(s) of a multipole but is more uniformly distributed, enveloping the entire molecule's valence electron system. The theoretical basis for CBS arose from the dispersion and electron correlation corrections that were applied to the model of the DBS in order to produce more quantitatively accurate predictions of binding energies[12,19,20,37].

Species such as C_{60}^-[9], other anionic spherical fullerenes[38] and clusters of $(NaCl)_n^-$[39] have been predicted to host CBSs. The earliest experimental evidence for the CBS was the observation of Xe_n^- clusters in a mass spectrum[40].

Being a noble gas, there is no means by which the excess electron may be bound in a valence orbital and no permanent multipole of the cluster to which it might be attracted. However, Xe has a large polarisability[41] and would therefore enjoy a reasonably large charge:induced-dipole interaction with an electron in its proximity. More recently, the first spectroscopic observation of a CBS was made in the trimer cluster anion of *para*-toluquinone[42], which was shown to have too small a permanent dipole to host a DBS. In this instance, the CBS was accessed by internal conversion after the cluster was photoexcited into a π^* state. The excess electron subsequently autodetached as the CBS vibrationally coupled with the ground electronic state of the neutral cluster.

These non-valence binding modes of the excess electron in molecular anions have a number of things in common. In each case, the excess electron is weakly bound and occupies a large orbital that experiences minimal spatial overlap with the valence system of the molecule. DFT and *ab-initio* calculations on these states require special treatment using extra-diffuse orbitals and custom basis sets[8]. Experiments have confirmed that these states can act as doorway states for an excess electron joining or leaving a molecule and therefore prove to be chemically interesting. However, it has been surmised that these states occur infrequently in condensed-phase environments but instead probably play a crucial role in a variety of gas-phase chemistry[8]. The CBS in particular may prove to be instrumental in the propagation of chemical pathways through electron capture by molecules lacking a sufficient permanent multipole moment in contexts such as the interstellar medium[3,4], the ionosphere[5], reactive interfaces[6,7] and in radiation chemistry[2].

1.2 Photoelectron spectroscopy

Photoelectron spectroscopy (PES) is a technique for probing the electronic structure of gas-phase atoms and molecules. It relies on the photoelectric effect[43–45], a phenomenon in which electrons can be removed from the surface of a material when an incident photon imparts more energy than that with which the electrons are bound, referred to as the work function. By using a known photon energy and measuring the velocity (speed and direction) distribution of the resulting photoelectrons[46–48], information can be gathered about the electronic structure of the material. In practical terms, the photoelectrons are usually measured either by a hemispherical electron energy analyser[49], a magnetic bottle spectrometer[50] or by velocity-map imaging (VMI)[51]. The resulting spectrum is a distribution of the number of photoelectrons produced as a function of their electron kinetic energy (eKE). Section 2.1.2.4 contains the details of the experimental apparatus used to perform VMI in these studies.

1.2.1 Information encoded in the photoelectron kinetic energy spectra

The principle of conservation of energy underlies the primary measurement derived from PES. The photoelectric effect is described by,

$$\text{eKE} = h\nu - \phi, \tag{1.1}$$

where $h\nu$ is the energy of the incident photon, ϕ is the work function of the material and eKE is the kinetic energy of the outgoing photoelectron. In the studies detailed in this thesis, the material analyte was invariably gas phase molecular or atomic anions. As mentioned in Section 1.1, those molecules with a positive EA are typically in the range $0 < \text{EA} \leq 4$ eV. Therefore, photons with at least as much energy in the near-infrared (IR), visible, near-ultraviolet (UV) and mid-UV ranges are usually sufficient to photodetach the excess electron from the anion.

However, it is an oversimplification to substitute ϕ with EA in Equation 1.1. Instead, electron binding energy (eBE) is used. This term can account for any energy that is retained by the analyte, which may be electronically and/or rovibrationally excited following photodetachment.

Photoelectron emission can be subdivided into two types:

1.2.1.1 Prompt direct detachment

Direct detachment is an instantaneous process that reveals the energy separation between the initial state of the anion before photodetachment and the final state of the neutral analyte in the same nuclear geometry. In the case of atomic anions, the nuclear geometry of the anion and neutral species are always the same because there are no bonds to stretch or bond angles to bend. The EA therefore corresponds to the smallest photon energy, $h\nu$, that produces photoelectrons by a single-photon direct detachment process.

However, it is not always so simple for molecular anions. In order to obtain a direct measurement of the EA of a molecule by PES, both the initial state of the anion and the final state of the neutral must be their respective ground electronic states *and* the geometry of the two must be similar enough to observe a direct $\nu' = 0 \leftarrow \nu = 0$ vibrational transition. The conditions under which the studies in this project were undertaken ensure that the initial state of the anion is always the ground electronic and vibrational state. However, whether the equilibrium geometries of the anion and neutral species are similar enough to measure the EA in this way is molecule-dependent and cannot be controlled by experimental conditions.

A consequence of the Franck-Condon principle[52] is that the extent to which the wavefunctions of the initial vibrational state in the anion and final vibrational state in the neutral overlap determines the cross section of the photodetachment process. This is described by the reflection principle represented in Figure 1.1. Where the geometry of the anion and neutral species are similar, the Franck-Condon overlap between the lower vibrational levels of the two states is significant. Where the overlap is favourable and the energy resolution of the detector permits, the individual vibrational levels of the neutral's accessible electronic states will be evident in the photoelectron spectrum, as demonstrated by the M^{0*} A state in Figure 1.1. For each such electronic state of the neutral, there will be a series of narrow peaks that can be assigned to the $\nu' = n \leftarrow \nu = 0$ transitions. The intensity of each peak is determined by the Franck-Condon overlap between the initial and final wavefunctions and its width is usually limited by the detector's resolution.

Where the Franck-Condon overlap is poor, the geometry of the anion will correspond to a point on the neutral's potential energy surface far from equilibrium. Therefore, the $\nu' = 0 \leftarrow \nu = 0$ transition may be inaccessible and the photon energy required to directly detach the excess electron will be higher

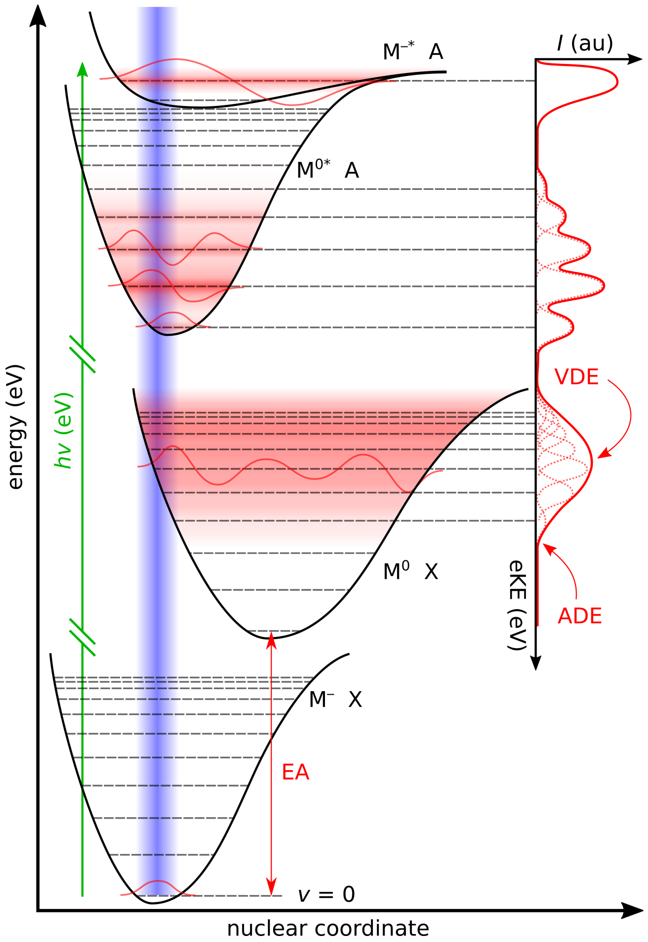

Figure 1.1: The reflection principle describes how different features in a photoelectron spectrum may arise. The blue column represents the projection of the anion's ground state wavefunction on the various final states of the molecule. Where the Franck-Condon overlap between the initial and final states is favourable, the photodetachment cross section is high and the corresponding feature on the photoelectron spectrum is large – shown to the right of the diagram. If the overlapping vibrational levels in the neutral electronic state are close together, as seen in the M^0 X state, the corresponding feature in the spectrum will be broad and devoid of structure. Where overlap occurs with vibrational levels that are well-separated at the bottom of the potential well, such as the M^{0*} A state, each vibrational state may be resolved in the spectrum. Where the incident photon may be resonant with an unbound or quasi-bound electronic excited state of the anion, such as the M^{-*} A state, the electron may boil off with low eKE as the anion changes shape and couples to a neutral state. The corresponding feature in the spectrum is a relatively broad peak at low eKE.

than the EA. Furthermore, due to anharmonicity in the potential and the multiplicity of vibrational modes that may incorporate the original geometry of the anion, the vibrational levels in the neutral state that are accessible will be closely spaced and may not be resolved in the spectrum. The result is that for each such electronic state of the neutral accessible by direct detachment, the spectrum will yield a single broad peak with a Gaussian profile. This process is represented by the state labelled M^0 X in Figure 1.1.

However, the photoelectron need not be removed from the highest occupied molecular orbital (HOMO) of the anion. If $h\nu$ is sufficient to remove a more tightly-bound electron from a lower-lying orbital, the neutral species is left in an electronic excited state, such as the M^{0*} A state in Figure 1.1. Information about the energetics and geometry of this state can be extracted in exactly the same manner as for the ground electronic state of the neutral.

1.2.1.2 Delayed autodetachment and thermionic emission

Compared to the infinite series of electronic excited states of neutral atoms and molecules, anions do not necessarily have bound excited states. Those that do may only bind the excess electron by a few vibrational energy levels. However, bound or not, excited states may still be accessible via photon excitation. If the incident photon is resonant with an unbound excited state, the molecule will undergo nuclear motion before coupling to an electronic state of the neutral molecule, thereby releasing the electron with lower eKE than the corresponding direct detachment process to that neutral electronic state[8]. Similarly, suppose there exists an excited state of the anion that is bound by only a few vibrational levels, such as the M^{-*} A state in Figure 1.1. A photon resonant with such an excited state may access one of its higher vibrationally levels if the Franck-Condon overlaps dictate. Sufficiently energetic vibrations of the excited state may cause the anion to couple to a neutral electronic state, thereby 'boiling off' the electron with low eKE as in the case of an unbound state[11]. The remainder of the photon energy remains in the molecule as vibrational energy.

Autodetachment can be a delayed process as it may require the molecule to change shape before the electron is released. In such cases, it appears on the photoelectron spectrum as a low energy peak with a maximum at eKE > 0 eV or as a lump on the low eKE side of a direct detachment peak. When $h\nu$ is varied, an autodetachment feature only appears in the energy range where the photon is resonant with the electronic transition.

Thermionic emission is a similar process to autodetachment. The difference is that anion undergoes internal conversion, non-radiatively decaying back into a vibrationally hot ground state before the electron is boiled off[53]. This requires that the excess electron in the anion be more weakly bound than the nuclear bond energy such that the molecule may vibrate enough to throw off the excess electron without itself breaking. Thermionic emission is a statistic process and the shape of the feature differs from autodetachment in that it takes the form of an exponential decay at low eKE that can be modelled[54] by,

$$I(\mathrm{eKE}) = e^{\frac{-\mathrm{eKE}}{k_{\mathrm{B}}T}}, \tag{1.2}$$

where $k_{\mathrm{B}}T$ is a measure of the internal energy of the hot molecule. Thermionic emission is also a delayed process as it requires the anion to undergo internal conversion before the electron is released.

The shape of the photoelectron spectrum therefore contains a large amount of information about the electronic structure and relative geometries of the anion and neutral species. However, additional information can also be gleaned from the image generated by the photoelectrons incident on the position-sensitive detector in the VMI process.

1.2.2 Information encoded in the photoelectron angular distribution

In addition to the energetics derived from the eKE spectrum, the photoelectron angular distribution (PAD) produced in the VMI process contains information about the photodetachment process. For photoelectrons generated in a single-photon process by linearly polarised light, the PAD has the general form[55],

$$I(\theta) = \frac{\sigma}{4\pi}(1 + \beta_2 \mathrm{P}_2 \cos(\theta)), \tag{1.3}$$

where θ is the angle relative to the polarisation axis, σ is the total photodetachment cross section, $\mathrm{P}_2 \cos(\theta)$ is the second-order Legendre polynomial and β_2 is the anisotropy parameter. The β_2 parameter is constrained between the bounds of -1 and $+2$. It contains information about the angular momentum of the photoelectrons and by extension the atomic or molecular orbital from which the photoelectron came.

A single photon imparts an angular momentum change of ±1. Therefore, if the laser is linearly polarised and the photoelectron came from an orbital for which l is a good quantum number, the outgoing photoelectron distribution will have angular momentum of $l \pm 1$. An s- or σ-like atomic or molecular orbital will yield an outgoing p-wave and the β_2 parameter of the cumulative PAD will be positive, up to $+2$. Conversely, photoelectrons emanating from a p- or π-like

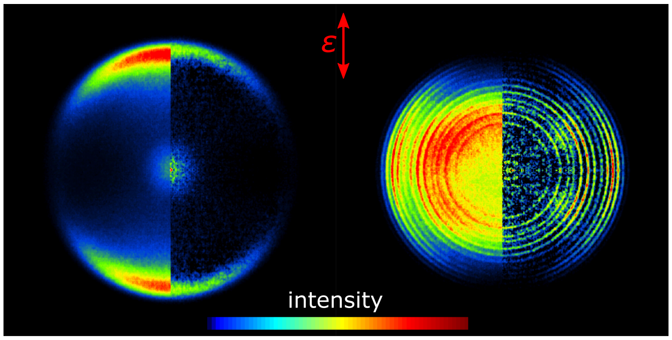

β_2 = + 2.0 β_2 = – 1.0

Figure 1.2: Example VMI heat maps with opposite PADs. On the left is the image of $C_6F_6^-$ at $h\nu = 3.9$ eV and on the right, O_2^- at $h\nu = 2.95$ eV. The left half of each image is the raw data and the right is the reconstructed central slice of the photoelectron Newton sphere that contains the velocity information. The polarisation of the laser is indicated by the red arrow. Where the north and south poles of the image are most intense, the β_2 parameter is positive and indicates that the orbital from which the electron cam is s- or σ-like. Where the east and west poles are most intense, the β_2 parameter is negative and indicates that the orbital from which the electron cam is p- or π-like.

atomic or molecular orbital will yield a combination of outgoing s- and d-waves and the β_2 parameter will be negative, down to − 1. This is demonstrated by the examples shown in Figure 1.2.

The Wigner threshold law[56] applied to PES dictates that the cross section, σ, for photodetachment of the excess electron near threshold can be expressed as,

$$\sigma \propto \mathrm{eKE}^{l+1/2}, \tag{1.4}$$

where l is the angular momentum of the outgoing photoelectron wave[57]. Therefore, if the outgoing wave has components with different angular momenta, those with the lowest l will be most prevalent at low eKE. Consequently, for p- or π-like orbitals, outgoing s-waves prevail over d-waves at low eKE and therefore those features look more isotropic than those at high eKE. Conversely, for s- or σ-like orbitals, the outgoing electron must be a p-wave and therefore anisotropy is expected even at low eKE.

In general the information gathered from the PADs in PES is rarely quantitatively useful. The qualitative insight is usually sufficient to complement or confirm the interpretation of the photoelectron spectra[58,59]. Recently, however, it has also been shown that PADs are sensitive to phenomena such as excited state resonances[60], population dynamics[61] and molecular conformations of the parent anion[62]. PADs are therefore a useful indicator not only of the symmetries of the relevant atomic or molecular orbitals but also of potentially interesting dynamics.

1.2.3 Frequency-resolved photoelectron spectroscopy

In 1992, a PES study[63] was undertaken of the phenide, benzyl and phenoxide anions at $h\nu = 3.53$ and 3.41 eV. A series of unidentified peaks present in the spectrum at $h\nu = 3.53$ eV were absent in the spectrum obtained at the reduced photon energy. This difference was attributed to the presence of a resonant metastable electronic excited state of the anion 1.06 eV above the ground state of the neutral that subsequently undergoes autoionisation. Similarly, in a study in 1999, anion excited states of *para*-benzoquinone were deduced from the resonances observed in photoelectron spectra measured at different photon energies[64]. More recently, a series of electronic excited states and subsequent autodetachment pathways of the *para*-methylphenoxide anion were evident in its photoelectron spectra as the energy of the incident photon was varied[65]. The discovery that the energy of the photon in PES is sensitive to these kinds of molecular dynamics provided the motivation to develop frequency-resolved PES as a technique.

Sometimes referred to as ‘one-colour’ PES (as opposed to two-colour time-resolved PES), frequency-resolved PES involves acquiring photoelectron spectra at discreet intervals over a range of photon energies. Although all of the direct detachment features in the spectrum can be identified simply using the greatest possible photon energy, some delayed detachment processes such as autodetachment will only be evident when the photon is resonant with an excited state transition. Therefore, by scanning the photon energy and recording the photoelectron spectrum at regular intervals, points at which photoinduced molecular dynamics occur can be identified. The Verlet group has been at the forefront of the ongoing development of this technique since 2013, using a continuously tuneable light source (described in Appendix A.2.1) to probe the intrinsic dynamics of systems such as *para*-benzoquinone, tetracene and menadione[62,66–74].

Frequency-resolved PES can be reported in a false colour plot where the spectra are normalised and aligned on a common eKE axis with an orthogonal $h\nu$ abscissa. An example is shown in Figure 1.3. Direct detachment features, such as features (*i*) and (*ii*), appear as diagonal lines where the peak eKE increases commensurately with $h\nu$. The vertical detachment energy (VDE) is derived from the photon energy at which the maximum of the first direct detachment peak appears. This corresponds to the energy difference between the anion and neutral ground electronic states in the equilibrium geometry of the anion. As described in Section 1.2.1.1, the EA is not necessarily available in the spectrum but where the Franck-Condon overlap is favourable, will coincide with the adiabatic detachment energy (ADE), its closest substitute. This is derived from the photon energy at which the onset of the first direct detachment peak appears. This corresponds to the energy difference between the anion and neutral ground electronic states in the geometry accessible to the anion that closest resembles that of the equilibrium geometry of the neutral. In some cases, the equilibrium geometries of the anion and of the neutral will be reasonably similar and the ADE will be close to the EA.

The frequency-resolved spectra may contain features that point to the occurrence of dynamic processes. Given a laser pulse of sufficient intensity and/or duration, multi- or multiple-photon processes are possible. Multi-photon refers to the simultaneous incidence of two or more photons on a single molecule, the likelihood of which grows with increasing laser intensity. Multiple-photon refers to the sequential incidence of two or more photons, the likelihood of which grows with increasing laser pulse intensity and may change with the laser pulse duration depending on how the molecule changes in the time between the successive arrival of the photons. In each case, the total energy injected is the sum of the component photons and therefore may result in spectral features at higher eKE than the neutral ground state direct detachment feature. These processes are most likely to occur where there is a resonant excited state of the anion, which may undergo some evolution. Similarly, the presence of peaks that do not follow the aforementioned diagonal path indicates that the energy injected by the photon is driving other processes in the system, namely some form of nuclear motion.

While the electronic structure of molecules is of some interest, often their intrinsic dynamics provide a deeper insight into their chemical properties. These dynamics identified in the frequency-resolved spectra are therefore of interest and time-resolved PES must be employed to probe the exact mechanism.

1.2.4 Time-resolved photoelectron spectroscopy

Although frequency-resolved PES can demonstrate that there may be some active dynamics at a particular photon excitation energy, the technique provides no temporal resolution with which to probe them. Time-resolved PES achieves this by acquiring photoelectron spectra using two femtosecond laser pulses of different energies delivered to the analyte with a variable time delay between them. The ‘pump’ pulse is tuned to be resonant with an electronic excited state of the anion identified in the frequency-resolved spectra. The ‘probe’ pulse arrives after a specified delay to photodetach the electron from the excited state of

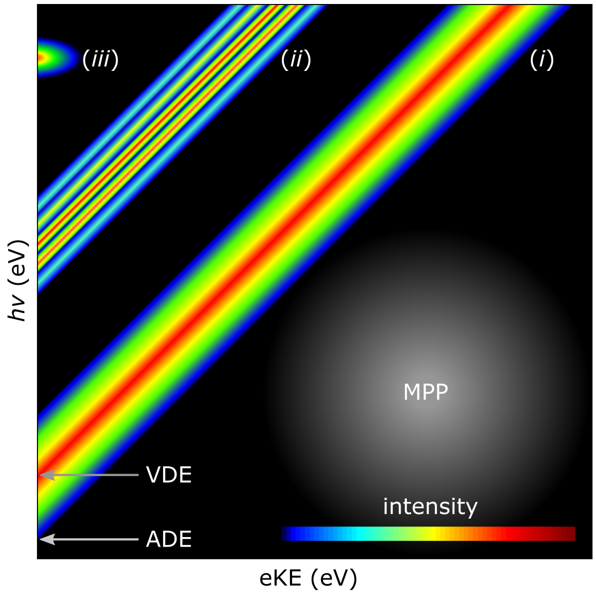

Figure 1.3: A sketched representation of potential features exhibited in frequency-resolved photoelectron spectra, reported in a false colour plot. Feature (*i*) corresponds to direct detachment of the excess electron to the ground electronic state of the neutral. The broadness of the peak indicates, according to the reflection principle, poor Franck-Condon overlaps between the $\nu = 0$ level of the anion and the lower levels of the neutral ground state. The ADE and VDE are derived from the photon energies at which, respectively, the onset and maximum of this peak first appear. Feature (*ii*) corresponds to direct detachment of an electron from a sub-HOMO orbital, leaving a neutral molecule in an excited electronic state. The vibrational structure within the feature indicates favourable Franck-Condon overlaps and therefore geometric similarity between the anion and neutral states. Feature (*iii*) corresponds to some form of autodetachment or thermionic emission where the molecule absorbs the photon energy into nuclear motion before releasing the electron with low eKE. This feature only appears when the photon is resonant with the electronic transition. Features in the region labelled MPP, to the right of the first direct detachment peak may only arise from multi- or multiple-photon processes.

the anion as it evolves. The ultrashort duration of the pulses gives the technique its time-resolution.

In 1999, the Nobel Prize for Chemistry was awarded to Ahmed Zewail for his pioneering work in probing the dynamics of chemical bonds with ultrafast lasers[75,76]. Although femtosecond and ultrashort pulse lasers had been in development for many years already[77], this particular work was the first application of the technology to study molecular dynamics and Zewail was hailed as the father of 'femtochemistry'. Since then, time-resolved femtosecond spectroscopy has been adopted by many research groups around the world, many of whom have used the technique for PES. Time-resolved PES has been the cornerstone of the Verlet group since 2008 and numerous investigations have been made of the molecular dynamics in a variety of systems, notably the green fluorescing protein, quinone, and the isolated deprotonated nucleotides[42,60,61,67,68,70,71,78–90]. All previous experiments in the group were undertaken in an instrument[61] not dissimilar to the one described in Chapter 2 with the exception that the method for generating the gas-phase samples was previously limited to the continuous room-temperature electrospray ionisation technique.

There are a few conditions to consider when performing time-resolved PES. Ideally, neither pulse will have sufficient energy to photodetach the excess electron on its own but if either one does, a one-colour spectrum can be subtracted from each pump-probe spectrum to isolate photoelectron signal that arises only from two-photon processes. Similarly, the probe pulse should not be resonant with any excited states lest its dynamics become convoluted with those of the state accessed by the pump pulse. Finally, the intensity of the two laser pulses, particularly the pump, should be optimised to generate a measurable pump-probe photoelectron signal while being restrained in order to minimise the occurrence of one-colour multi-photon signal.

The time-resolved photoelectron spectra can be reported in a false colour plot, similar to that of the frequency-resolved spectra. An example is shown in Figure 1.4. Here the spectra share a common eKE axis and are aligned along a time-delay abscissa. An eKE peak with a time-dependent intensity corresponds to an electronic state of the molecule with a changing population. The lifetime or rise-time of such states can be derived from the time-dependent integral of the spectra within a spectral window around the peak. Features whose lifetimes or rise-times correlate, such as features (*i*) and (*ii*), may indicate active processes such as internal conversion or autodetachment as the population transfers between states. A peak that has a time-dependent maximum eKE, such as feature (*iii*), is likely to arise from coherent nuclear motion as the changing geometry of the molecule alters the energy separation between the potential energy surfaces of the anion and neutral.

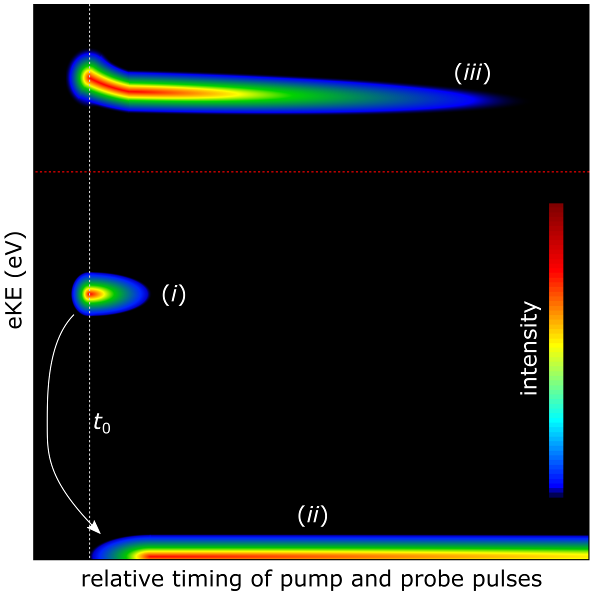

Figure 1.4: A sketched representation of potential features exhibited in time-resolved photoelectron spectra, reported in a false colour plot. Assuming neither photon can directly detach the excess electron, the pump photon excites the anion into an electronic excited state and the probe photon interrogates its evolution. Feature (*i*) indicates that the excited state is short-lived. Feature (*ii*) has a rise time commensurate with the lifetime of feature (*i*) and therefore corresponds to some form of population transfer such as internal conversion or autodetachment. Alternatively, the excited state may be longer lived, as seen in feature (*iii*) above the red dashed line. The maximum eKE associated with this peak moves, indicating a change in the VDE that would be expected from a shift in the relative equilibrium geometries the anion and neutral species.

When deployed in combination, frequency- and time-resolved PES and the information contained in their respective PADs offer a comprehensive picture of the photoactivated dynamics exhibited by molecular anions. Dubbed 'FAT-PI' (frequency-, angle- and time-resolved photoelectron imaging), the power of this approach was first demonstrated in a study of the menadione radical anion[67]. In this investigation it was shown that anion resonances above threshold for photodetachment were able to facilitate the formation of metastable anions that subsequently relaxed into a vibrationally hot ground state. It was argued that this mechanism is important for understanding electron capture mechanisms by related polycyclic and delocalised species. The methodology employed to gather and interpret the data presented in Chapter 3 echoes that of FAT-PI.

1.3 Hexafluorobenzene (C_6F_6)

1.3.1 Previous photoelectron spectroscopy and theory studies

C_6F_6 is a colourless volatile liquid of limited commercial significance. Its practical uses are confined to NMR[91], where it is used as a solvent and standard, and biomedical research, where it is used as a reporter molecule for the presence of O_2 in tissue. An analogue of benzene, C_6F_6 is a closed-shell molecule with D_{6h} symmetry and no permanent dipole or quadrupole moment. It forms a stable anion, $C_6F_6^-$, hosting the excess electron in a VBS with an EA previously calculated to be between 0.454 - 0.76 eV[92–94]. The anion is open-shell and adopts a buckled geometry with C_{2v} symmetry. The fluorine atoms bend out of the plane as a result of Jahn-Teller and pseudo-Jahn-Teller distortion that arises from the mixing of one of the neutral's two degenerate e_{2u} lowest unoccupied molecular orbitals (LUMOs) with the a_{1g} LUMO+1. As a consequence of the geometric disparity, the EA is not thought to be directly measurable by PES, which has previously yielded[95,96] a VDE of 1.56 and 1.55 eV and an ADE of 0.80 and 0.7 eV. The ground electronic states of the planar neutral and buckled anion are referred to as S_0 and D_0 respectively.

However commercially unremarkable, C_6F_6 is chemically interesting because its anion is predicted to be able to host the excess electron in a CBS[97]. Voora and Jordan predicted that, far from the buckled equilibrium geometry of the anion's D_0 state, the molecule ought to adopt the planar geometry of the S_0 state when the excess electron is in the CBS. The orbital that the excess electron occupies in the CBS is large, diffuse and spherical, as shown in Figure 1.5. These calculations, performed using the EOM-MP2 method with the aug-cc-pVDZ+7s7p basis set predict an eBE of 140 meV for the CBS, which is expected to act as a doorway state for low energy electron capture and subsequently to undergo a barrierless transition to form the VBS[97].

Indeed, in 1976 an electron attachment study[98] of dilute gas-phase C_6F_6 in atmospheric pressures of N_2 or Ar discovered two non-dissociative resonances at eKE = 0.03 and 0.73 eV. The 0.03 eV resonance was attributed to the capture of a 'thermal' electron into the ground state of $C_6F_6^-$ but no actual resonant excited electronic state of the molecule was mentioned. The excess electron was presumed to be captured into one of two degenerate LUMOs in the π-system of the molecule, bound with an EA of 1.80 eV. The lifetime of the resulting anion at 298 K was measured to be 12 µs, as determined by time-of-flight mass spectrometry. The lifetime of the other resonance at higher eKE was immeasurably small and was therefore assigned to an unbound excited state of $C_6F_6^-$. It was also noted without explanation that these resonances exhibit surprisingly large attachment cross sections, similar in size to the de Broglie wavelength of the

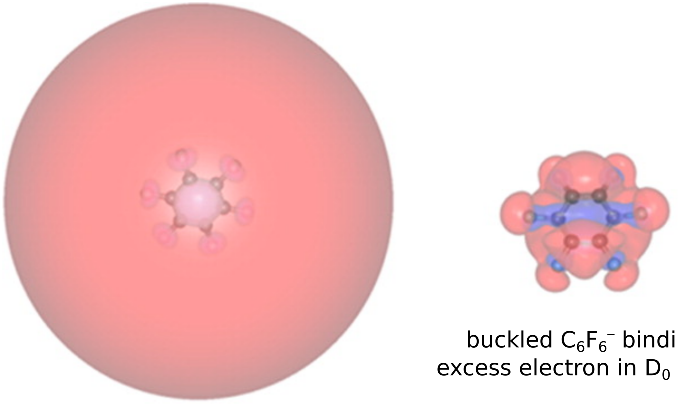

planar $C_6F_6^-$ binding
excess electron in CBS

buckled $C_6F_6^-$ binding
excess electron in D_0 state

Figure 1.5: Visualisations of the orbital associated with the CBS and the HOMO of the D_0 state of $C_6F_6^-$. The excess electron in the CBS is large, highly delocalised and spatially segregated from the valence orbitals. The geometry adopted by the molecule in the CBS is planar, like the neutral molecule, whereas the geometry of the D_0 state of the anion is buckled. Figure reproduced with permission from author and journal[97].

incoming free electron but far larger than the spatial extent of the molecule's π-system. Notably absent from the discussion in this study is the suggestion of an excited state of $C_6F_6^-$ that is actually resonant with the low eKE electrons. A non-valence binding mode of the excess electron to the molecule, such as a CBS, would help to explain this observation as it would be near-resonant with thermal electrons and would exhibit the large cross section and long lifetime measured for the 0.03 eKE feature.

1.3.2 Excess electron mobility in liquid C_6F_6

Although the results of solution-phase studies do not necessarily reflect those of gas-phase studies, one particular experiment in 1980[99] arrived at conclusions that corroborate the predictions made by Voora and Jordan. C_6F_6 was shown to be an exceedingly efficient scavenger of excess electrons in the non-attaching molecular liquid tetramethylsilane, at a rate of 1.2×10^{14} dm^3 mol^{-1} s^{-1}. At the same time, measurements made of electron mobility in pure C_6F_6 revealed that the charge was more than an order of magnitude more mobile than would be expected from the motion of molecular anions through the liquid. The propensity for the molecule readily to form a stable bound anion while simultaneously transmitting the charge through the liquid more rapidly than the transport of individual molecules led to the conclusion that the excess electron passes from a bound state in one molecule to its neighbour and does so without causing a change in the geometry of either molecule from a neutral planar configuration. These conclusions are consistent with the calculations that predict that in the CBS the molecule ought to retain its D_{6h} symmetry and that the orbital associated with the CBS should be large enough to overlap with neighbouring molecules in solution.

1.3.3 Excess electrons in C_6F_6 adsorbed on Cu substrate

An experiment[100] performed by Gahl et al in 2000 gives further credence to the idea that C_6F_6 is able to bind an electron in a delocalised manner. Two-photon photoemission experiments were carried out on C_6F_6 adsorbed on a Cu (111) substrate. Similar to pump-probe photoelectron spectroscopy, two-photon photoemission requires two femtosecond laser pulses, a pump and a probe with a variable time-delay. The pump photon excites an electron from the metallic substrate to an excited state above its surface. The probe photon subsequently removes the excited electron to vacuum where the distribution of eKE and angular incidence are measured, yielding information about the temporal and spatial character of the excited state.

In the absence of any adsorbate, the electron is temporarily bound in an image potential, localised normal to the surface but fully delocalised parallel to it. The lifetime of this state is determined by the extent to which its wavefunction overlaps with the metal substrate. The greater the overlap, the shorter the lifetime. On the addition of a single monolayer of C_6F_6 to the substrate, the excited electrons become highly localised parallel to the surface, suggesting some form of binding between the electron and the C_6F_6 molecules.

When further monolayers of C_6F_6 are added to the first, the lifetime of the excited electron increases while its binding energy and localisation parallel to the surface decrease. The lengthening lifetime and reduced binding energy suggest that the wavefuntion of the excited electron is increasingly removed from the Cu substrate. Furthermore, introduction of an overlayer of Xe does not significantly perturb the character of the excited electron, indicating that it must therefore be contained within the adsorbate layers rather than residing on top of them. The decreased localisation implies that the excited electron is large, mobile and extended over multiple molecules. The trends uncovered in this study provide additional evidence for the way in which the electronic structure of C_6F_6 is able to accommodate and interact with large and delocalised excess electrons.

1.3.4 Cluster studies

Cluster science is the study of aggregates of a quantifiable number of molecules or atoms in the gas-phase. The neutral species within clusters are held together by van der Waals forces and other intermolcular interactions such as hydrogen bonding, while charged constituents are bound in by charge:multipole and charge:induced-dipole interactions. Coulomb repulsion dictates that clusters are unable to have two constituent members with the same charge.

Clusters are a 'mesoscopic' phenomenon useful for exploring how the macroscopic properties of solution- and condensed-phase materials emerge from the properties of their microscopic components[101]. Clusters have been used to study numerous phenomena including micro- and incremental-solvation of various molecules[102,103] as well as the properties of the solvated electron[6,104–114], a solute not occupying the atomic or molecular orbital of a single cluster member but rather inhabiting the intermolecular space.

Clusters have also been used to study electron attachment processes, which can be mimicked by intra-cluster charge-transfer mechanisms. The excess electron located on one cluster member can be transferred to another upon photoexcitation of the cluster. I^- has been demonstrated to be an effective intra-cluster electron donor in many previous studies[1,33,107,115–133]. A number of these studies document the dynamics of the charge-transfer to solvent (CTTS) mechanism whereby the excess electron is photodetached from the I^- ion to become a solvated electron. However, it has also been demonstrated that the excess electron may alternatively enter directly into the valence system of a neighbouring molecule in the cluster via a charge-transfer state (CTS). This CTS can be thought of as an electronic excited state of the cluster and has been shown to take the form of DBS in systems such as I^-·uracil[1]. Given the similar characteristics of the DBS and CBS and the prediction that the CBS of $C_6F_6^-$ ought to act as a doorway for low energy electron capture, it may be reasonable to expect to observe a CBS acting as an intermediate in a charge-transfer process within anionic clusters containing C_6F_6. To that end, experiments were carried out on a new instrument, which is described in Chapter 2, the results of which are detailed in Chapter 3.

Chapter 2

Experimental methods

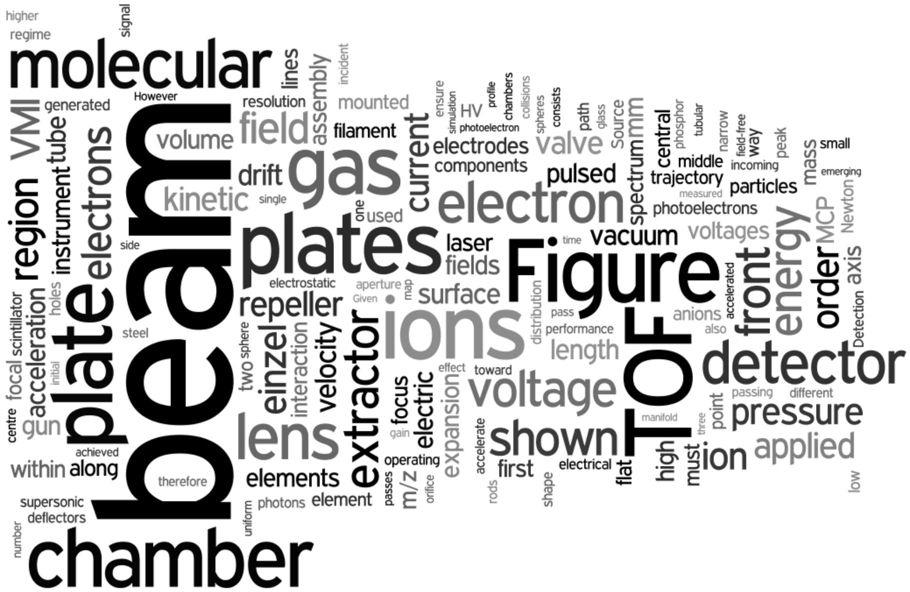

2.1 Molecular beam techniques

A molecular beam is a moving and collimated group of gas particles characterised by a narrow velocity distribution and a low frequency of collisions between the particles within the beam. The first molecular beam experiments were carried out in 1921 by Kallmann and Reiche[134]. Techniques have developed since then and molecular beams are now frequently used to isolate an analyte from its environment, carefully control its interactions with perturbations or study its microscopic properties and behaviours[135].

In order to eliminate unwanted perturbations to a beam in free molecular flow, collisions with other matter, whether background gas or solid surfaces, must be avoided. Collisions with background gas are reduced by containing the beam in a low pressure environment such as a vacuum chamber. The lower the pressure, the longer the mean-free-path and the greater the proportion of the beam preserved along its trajectory.

It is often necessary somehow to manipulate the motion of the molecules as they traverse the vacuum chamber. This is normally achieved with electric fields generated by conductive elements adjacent to the beam path. In this way, the beam can be steered and shaped without coming into contact with solid surfaces. Although neutral atoms and molecules can be manipulated by electric and magnetic fields exploiting the Stark and Zeeman effects[136], the strong interaction of charged species with these fields is greater by far, making them ideally suited to molecular beam studies.

In this project, a molecular beam experiment was developed in order to study the structure and dynamics of various gas-phase anions. The purpose of the following section is to describe the principle techniques deployed in this particular instrument for the benefit of a reader less familiar with this class of experiment. Given the enormous variety and versatility of molecular beam experiments reported in the scientific literature, the following descriptions of these techniques are not a comprehensive account of the methods available to achieve the desired effect. The limited scope of this thesis demands that the focus remain on the solutions that have been implemented in this particular experiment.

2.1.1 Initiating a beam

2.1.1.1 Gas source

Molecular beams are most commonly initiated by allowing gas to expand from a high pressure reservoir, p_0, into a region of lower pressure, p_b, commonly a vacuum chamber, through a narrow aperture or orifice. (Other beam formation techniques, such as laser ablation, electron bombardment or heating of solid materials, will not be discussed here.) The gas will exit the orifice at supersonic speeds when the ratio of p_0/p_b exceeds the threshold[135,137],

$$G = (\frac{\gamma + 1}{2})^{\frac{\gamma}{\gamma - 1}}, \tag{2.1}$$

where γ is the ratio of the specific heat capacities of the gas, $c_\mathrm{p}/c_\mathrm{v}$, at constant pressure and constant volume respectively. This is called a 'supersonic expansion'. Under continuous flow, the centre of the plume of gas that emerges in the region immediately after the orifice is referred to as the 'zone of silence' as the gas in this region accelerates supersonically and independent of the influence of background gas. However, the outer edge of the plume initially over-expands, giving rise to compression shockwaves lateral to the direction of the expansion when the pressure at the boundary drops below that of the background gas. These compression waves radially confine the expanding gas until the increased density produces a reflective shockwave, ending the zone of silence at a boundary called the Mach disk. The result is a highly directional and fast-moving molecular beam formed from the central portion of the supersonic expansion.

Although the gas in the zone of silence does not interact with background gas, there may be collisions within the expansion that serve to reduce the internal temperature of the beam. The number of collisions each gas particle will experience is dependent on the size of the orifice compared to the mean free path of the gas in the high pressure reservoir[138]. The larger the orifice compared to the mean free path, the greater the number of collisions during expansion. The rate of collisions within the beam reduces dramatically with increasing distance from the orifice. It is therefore commonplace to position a narrow aperture skimmer inside the zone of silence in order to transmit the cooled gas into a different vacuum chamber before the reflective shock wave at the Mach disk heats the gas up again.

The collisions in the initial expansion may reduce the internal temperature of the beam enough for the constituent species to form clusters, bound not by chemical bonds but by Van der Waals forces. In order to optimise the conditions for cooling and clustering, the majority of the gas in the reservoir is an inert carrier or buffer gas. The analyte may only be present in trace quantities but this is usually sufficient for detection. The noble gases are ideal buffer gases, not only because of their chemical inertness but also due to their propensity to scatter elastically with internally hot molecules in the expansion, taking away a proportion of their internal energy with each collision. The result is a fast-moving beam of particles with a very narrow velocity distribution and therefore a low translational temperature in its internal reference frame. Furthermore, after many collisions, the population of any molecules in the beam will almost entirely be in the ground vibrational state[138].

A supersonic beam can be achieved simply by placing a pinhole or capillary in the dividing wall between a region containing a high pressure gas sample and a vacuum chamber. However, this solution does not offer direct control over certain parameters, including being able to start and stop the beam easily. Although some experiments do employ continuous molecular beams, only pulsed beams will be discussed here.

A pulsed molecular beam is generated by periodically opening and shutting the narrow orifice between the high 'stagnation' pressure gas reservoir and the vacuum chamber. This is achieved with a pulsed pneumatic valve such as the Hannafin Parker Series 9 General Valve or, as in the case of this experiment, the more specialist Even-Lavie pulsed valve[139,140]. These valves incorporate a fast-action solenoid, a magnetic plunger and a spring to minimise the time for which the valve orifice is open. The result is a train of gas pulses, each with a duration of tens to hundreds of microseconds at a repetition rate of up to 1 kHz.

The Even-Lavie valve is able to generate a very short-duration, highly directional, fast moving molecular beam with a very low internal translational temperature. The excellent performance of this valve is owed to its ability to maintain high stagnation pressures, the rapid actuation of the plunger in opening and closing the orifice and the shape of the nozzle in forming the beam profile. For Ar gas with a stagnation pressure of 100 bar at room temperature[140], the molecular beam velocity is $600 \pm 20\ \mathrm{m\,s^{-1}}$ and the internal temperature of the beam is 2 ± 1 K. This corresponds to Ar atoms with a kinetic energy of 75 meV. Under these conditions the sample molecules are likely to form stable clusters within the supersonic expansion without requiring additional cooling of the gas prior to injection.

2.1.1.2 Ionisation

There are a number of techniques for adding or removing charge from gas-phase atoms and molecules. Many of these involve generating a plasma discharge in the gas expansion. Rather than generating a single analyte, these methods usually produce a soup of different products that can be tuned to an extent by varying the conditions of the supersonic expansion and plasma.

The simplest discharge ion source involves passing the gas expansion through a region containing an electric field stronger than the breakdown voltage of the gas. A field strength of ~ 10^4 V cm^{-1} is usually sufficient and is best achieved by placing two electrodes within 1 - 2 mm of each other immediately at the nozzle of a valve and applying a ~ 1 - 2 kV potential between them. As the gas fills the region, electrons flow from the cathode to the anode, generating an often visibly glowing plume that contains a soup of charged products.

Another way to produce ions is by electron bombardment of the gas expansion. A ring ioniser or electron gun can be used to generate a current or beam of electrons in vacuum. This method has a couple of key advantages over a discharge source. Firstly, the point in the gas expansion at which ionisation occurs can be tuned by moving the electron beam along the molecular beam axis. Secondly, the requirement to position electrodes and other solid surfaces close to or within the molecular beam path is eliminated, minimising perturbation of the gas expansion. Finally, the energy of the incident electrons can be tuned such that their interaction with the gas is much softer and less destructive than the discharge in a strong electric field of ~ 10^4 V cm^{-1}.

An electron gun produces a suitable beam of electrons with a narrow kinetic energy distribution and a focusable beam waist. A simulation of the electron gun in the instrument is shown in Figure 2.1. At the heart of this electron gun is a hot cathode (A), a fine filament wire through which an electric current is passed. This causes it to glow at a temperature of ~ 1000 - 2000 K, releasing electrons into the vacuum. The tip of the filament is contained within an electric field that accelerates and directs the emitted electrons toward its target, the gas expansion (H). The electric field that accelerates and focuses the electron beam is the product of a series of stacked tubular electrodes (B - F) maintained at different voltages. The ultimate kinetic energy of the electrons in the field-free vacuum region is determined by the voltage at which the filament wire is held.

A glow plasma is generated at the point where the electron beam intersects with the supersonic expansion (H), producing a mixture of charged products. At high electron beam energies this is a violent process, generating many cations

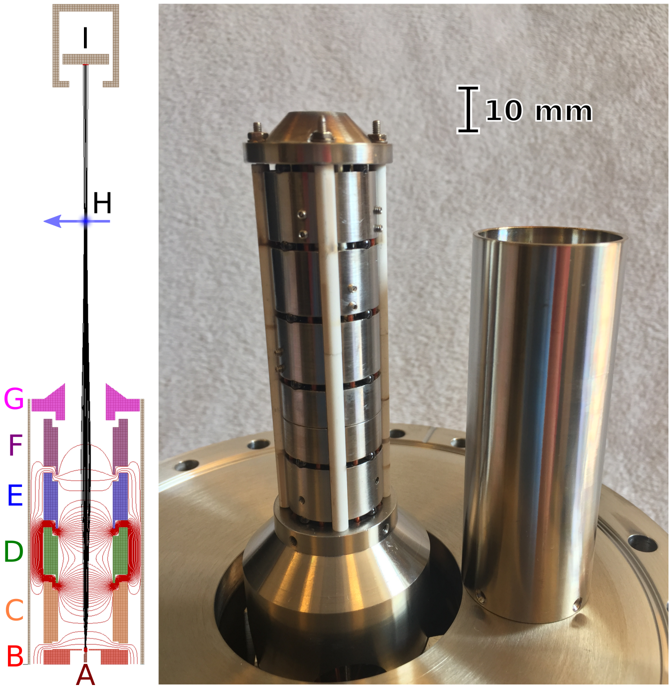

Figure 2.1: The assembled electron gun on the bench and a simulation of the electron beam in the SIMION software package. The stacked electrodes are normally contained within the tubular sheath displayed adjacent to the assembly in the photograph. The projected trajectories of the electrons in the beam are indicated by the black lines. The electric fields between the elements are represented by the red field lines.
A – the heated tungsten filament.
B - F – the stacked tubular electrodes that accelerate and steer the electron beam.
G – the nozzle and earthing sheath enclosing the HV electrodes.
H – the electron beam intercepting the expanding molecular beam.
I – the electron beam dump.

and unwanted molecular fragments. However, a carrier gas such as Ar not only provides a good clustering medium but also a source of slow electrons under electron bombardment. A single electron impact at 300 eV ionises Ar, producing 2 - 3 secondary low kinetic energy electrons slow enough to be captured by atoms, molecules or clusters in the supersonic expansion[141,142]. The resulting anions are present in sufficient quantity for measurement.

2.1.2 Electrostatic optics

Electrostatic optics provide the easiest and most reliable way to manoeuvre particles around a vacuum chamber. They are so called because they act on a molecular beam in an analogous way to glass optics on a laser beam. While electrostatic optics are able to manipulate the motion of neutral species by means of the Stark effect[136], only the motion of charged particles, specifically anions, will be considered here.

When a voltage differential is applied to adjacent conductive surfaces, the field generated in the space between them produces an accelerative force that acts upon charged particles within the field. The magnitude, direction and shape of the field is a function of the shape of these electrodes, the voltages applied to them and the distance between them. The Simion 8.0 software package was used to model the inhomogeneous fields around the various components in the instrument in order to simulate the behaviour of ions traversing the beam path. The following elements are common components in molecular beam experiments and their function will be described in some detail.

2.1.2.1 The einzel lens

The einzel lens is used either to collimate a divergent ion beam or focus a collimated one, similar to a biconvex or plano-convex lens in the path of a laser. It consists of an assembly of three consecutive concentric tubular electrodes, as shown in Figure 2.2. The ions pass along the central axis of the three tubes. The first and last elements are typically held at 0 V and the middle element has a voltage in the region of the kinetic energy of the ion beam applied to it. The shape of the field lines in the space between the middle electrode and its neighbours resembles that of a biconvex optical lens. Analogously, the trajectory of the particles before and after this region reflects that of light rays passing through a bi-convex lens.

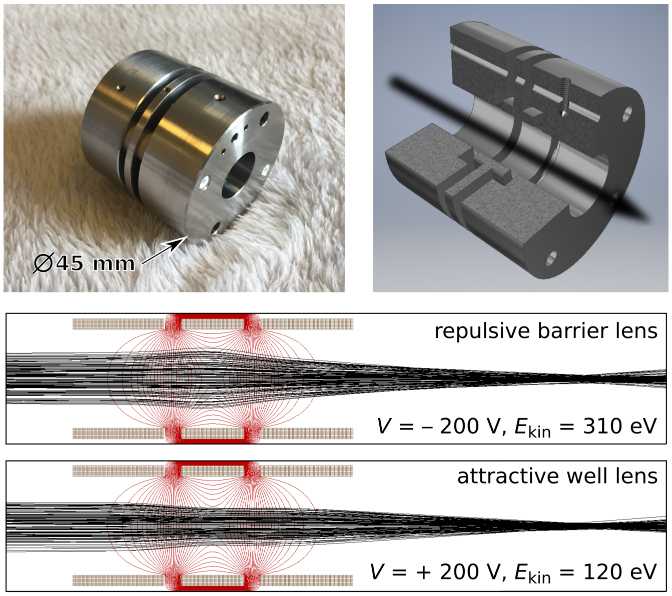

Figure 2.2: The design of the einzel lens assembly included in the instrument incorporates an overlapping section between the central and outer elements to ensure stray electric fields and background gas are excluded from the molecular beam path. The simulations show a cross section of the two types of einzel lens operating at $V = \pm 200$ V. The projected trajectory of the anions is indicated by the black lines. The electric field generated in the space between the elements is represented by the red lines. Note that although the focal lengths of the two lenses are the same, the kinetic energy of the molecular beam, E_{kin}, must be greater than the potential barrier generated in the repulsive barrier lens.

The focal length of the lens can be thought of as the extent to which the lens alters the momentum of the ions within the beam perpendicular to the direction of travel. The focal length depends on the energy of the incoming ions, the diameter of the lens aperture, the separation between the consecutive elements and, most crucially, the voltage applied to the middle element. The higher the energy of the incoming ions, the lesser the effect of the lens on their trajectories and the longer the focal length. The larger the lens aperture, the flatter the field lines in the region through which the ions fly and hence the smaller the effect on the radial momentum of the ions and the longer the focal length. Similarly, the larger the separation between consecutive elements, the flatter the field lines and hence the longer the focal length. Finally, the higher the voltage applied to the middle element, the stronger the field, the greater the effect on the radial momentum of the ions in the beam and therefore the shorter the focal length.

The quality of the focus produced by the einzel lens is a function of the kinetic energy distribution of the incoming ions and the size of the lens aperture relative to the beam profile. Given that the focal length of the einzel lens is dependent on the kinetic energy of the incoming ions, a beam containing ions with a large distribution of energies will not have a well-defined focal point. This is analogous to chromatic aberration observed in optical lenses. Similarly, the ambient pressure in the chamber can affect on the quality of the beam focus if the ions are likely to lose kinetic energy in collisions with background gas. Finally, in the same way that spherical aberration is more pronounced for incident light rays far from the normal line of a spherical lens, ions passing through the extremities of the einzel lens aperture will be focussed differently to ions in the central portion of the beam.

Given that the voltage applied to the middle element is the only parameter of the einzel lens that can reasonably be altered during operation, all the dimensional aspects of the lens must be simulated to ensure a suitable design before it is implemented. However, regardless of the charge on the particles in the ion beam, a negative or positive voltage may be applied to the middle element in order to have a similar effect on the outgoing beam shape. As long as the approach and exit of the einzel lens are field-free and referenced to the same potential, the kinetic energy of the outgoing beam is the same as that of the incoming beam. One side of the einzel lens accelerates the ions and the other side decelerates them to the same degree; the polarity of the ions with respect to the voltage applied to the middle plate determines the order in which the beam is accelerated and decelerated.

An einzel lens that decelerates the ions first (the 'repulsive barrier' lens shown Figure 2.2) can be operated up to a voltage corresponding to the kinetic energy of the incoming beam. Above this point, the ions will turn around and go back the way they came because they don't have sufficient kinetic energy to overcome the barrier. An einzel lens that accelerates the ions first (the 'attractive well' lens shown Figure 2.2) can operate at much higher voltages. However, it must be noted that when recording the time-of-flight (TOF) of a molecular beam, any einzel lens will alter this measurement. A repulsive barrier lens will lengthen the overall TOF and an attractive well lens will shorten it.

2.1.2.2 Deflectors

Deflectors change the path of a molecular beam in a similar manner to mirrors or reflective prisms diverting the path of a laser. The simplest form comprises a pair of flat plates, positioned parallel to one another either side of the molecular beam, as shown in Figure 2.3. A voltage difference applied between the two plates causes the ions passing through the gap to experience acceleration orthogonal to their direction of travel, altering their ultimate trajectory. With a second pair of plates positioned orthogonally, both the lateral and vertical velocity components of the ion beam can be adjusted but usually only by small degrees. For larger changes in trajectory, curved plates that follow the changing beam path must be used. In this instrument, rather than using flat plates, the two instances of deflectors are shaped out of a tubular electrode, cut into four quadrants and arranged symmetrically around the beam axis. This design works well for the same small angular deflections achieved with flat plates but was preferable to flat electrodes primarily for ease of construction with respect to the elements around them.

2.1.2.3 Time-of-flight mass spectrometry

Mass spectrometry (MS) refers to a collection of techniques for measuring the masses of atoms, molecules and clusters in a molecular beam. TOF MS relies on the particles carrying a charge in order to measure their mass. An accelerative electric field is applied to a collection of particles, imparting a uniform quantity of kinetic energy, E_{kin}, to each particle per unit charge it carries. Assuming each particle carries the same charge, z, every particle receives the same quantity of kinetic energy directed along a molecular beam path of fixed length, l, toward a detector. Assuming all the particles begin their journey simultaneously, particles of the same mass:charge ratio (m/z) travel together in a 'mass-packet' at the same velocity, v. Particles with lower m/z will accelerate to higher v and arrive at the detector before those with higher m/z. The constituent masses of particles

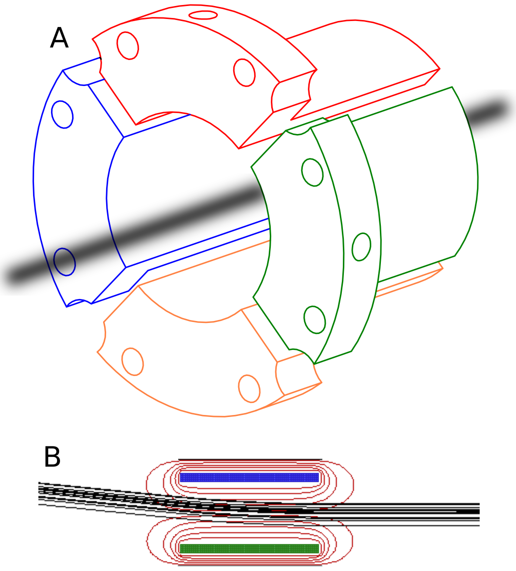

Figure 2.3: Deflectors are ideal for making alterations in the beam trajectory or compensating for small misalignments of the beam.
A – a pair of vertical (red & yellow) and horizontal (blue & green) deflectors.
B – a SIMION simulation of the blue & green horizonal deflectors operating at ±100 V. The field lines are shown in red. The ions have a kinetic energy of 2.7 keV and their trajectories are shown by the black lines.

in the beam is therefore determined by the duration, t, of their respective flights between their simultaneous acceleration and their arrival at the detector, given by

$$t = l\sqrt{\frac{\frac{1}{2}m/z}{E_{\text{kin}}}}. \tag{2.2}$$

At high masses, the difference in flight time, Δt between m/z and $m/z + 1$ is small due to the relationship $t \propto \sqrt{m}$. The resolution of a TOF mass spectrometer is the smallest mass at which $\gamma \geqslant \Delta t$, where γ is the temporal linewidth of the m/z peak. The linewidth of a peak corresponds directly to the spread of the corresponding mass packet along the molecular beam axis at the point of detection. The better the temporal focus of the beam, the narrower the spread of the mass packets and the better the TOF resolution. The temporal focus is determined by the kinetic energy distribution imparted by the initial acceleration of the beam and the initial spatial distribution of the particles during acceleration.

In 1955 Wiley and McLaren[143] devised a simple three-plate electrostatic assembly that delivered improved resolution for TOF mass spectrometers as it was less sensitive than existing techniques to the initial spatial and velocity distributions of the ions. Three thin and flat plates are stacked parallel to one another as shown in Figure 2.4. The ‘repeller’ plate sits at the back of the assembly, followed by the ‘extractor’ in the middle. A different voltage is applied to each plate to produce two electric fields that accelerate the ions at different rates. There is a long drift region between the plates and the detector, allowing the ion packets of uniform m/z to separate out along the beam axis.

The ions begin their journey in the extraction volume, the central space between the repeller and extractor plates. The field in this first region accelerates the ions toward the extractor plate. The central portion of the extractor and front plates are removed and replaced with a conductive mesh. These meshes allow the ions to pass through the plates with minimal losses while maintaining the flat electric field lines necessary for uniform acceleration of the ions in each acceleration region. The ratio of the diameter of the plates relative to the separation between them must be > 4 in order to prevent fringe fields from the edge of the plates perturbing the acceleration region. After initial extraction, the ions then pass through the mesh and into the next acceleration region.

In between the extractor and front plates, the field strength is much greater and the acceleration of the ions is increased. Every ion receives the full kinetic energy imparted by the field in this second region. The front plate is typically held at 0 volt so that the long drift region between it and the detector is field-free. This ensures that the trajectory of the beam is relatively unperturbed and the ions separate out into mass packets of uniform m/z for detection.

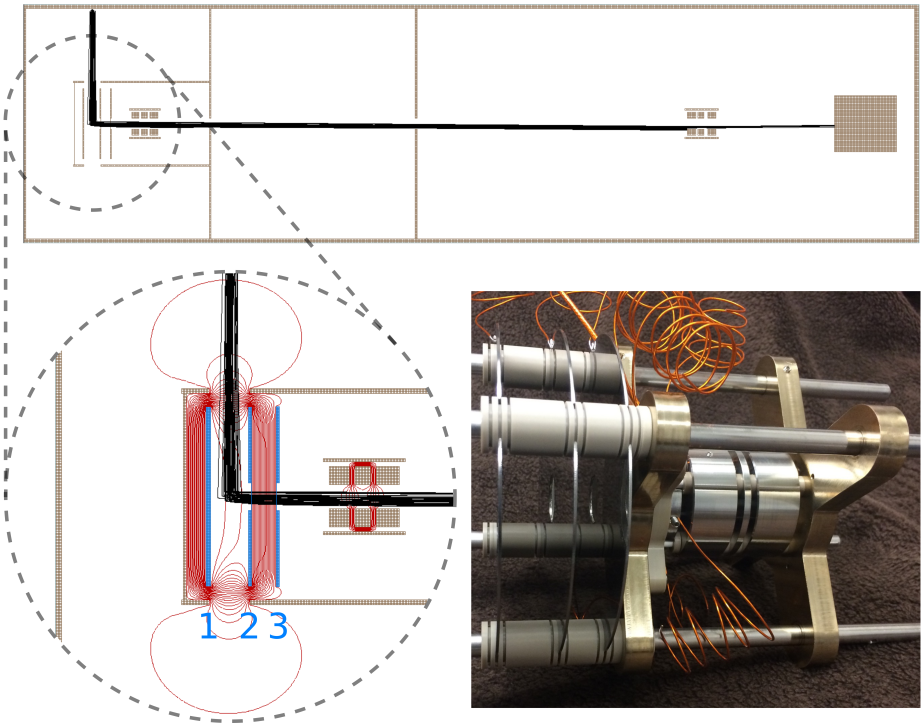

Figure 2.4: Images of the TOF components and a top-view SIMION simulation of the TOF regime. The black lines correspond to the trajectory of the ions and the red lines represent the electric field contours. The ions simulated have m/z = 186 and an initial velocity of 550 $\mathrm{m\,s^{-1}}$. The ions are accelerated orthogonally with respect their original direction of travel, down the length of the instrument and toward the TOF detector, passing through two einzel lenses along the way. The inset shows a more detailed view of the Wiley-McLaren TOF plates and the fields they generate. The repeller (1), extractor (2) and front (3) plates accelerate the ions simultaneously using pulsed HV switches. Deflectors, which lie between the front plate and the first einzel lens, and which compensate for the residual momentum from the supersonic expansion, have been omitted from this simulation due to symmetry constraints.

Assuming a trivial initial velocity and a uniform acceleration field, the distance, d, from the extractor plate an ion originates is related to the length of time, δt, it takes to reach the first mesh by $d \propto \delta t^2$. There is also a linear relationship between d and the total kinetic energy the ion achieves before entering the second acceleration region. Therefore ions that originate closer to the rear repeller plate will initially lag behind those that started closer to the extractor plate but due to their higher final velocity will eventually catch up with ions at the front of the mass packet.

The temporal focus is the point at which the distribution of each mass packet along the beam axis is at its shortest. This point can be tuned in order to coincide with the front surface of the ion detector by adjusting the ratio of voltages applied to the TOF plates or by adjusting the separation between them. The temporal focus can be brought closer to the TOF plates by turning down the voltage applied to the extractor plate relative to the repeller plate.

The width of the peak in the TOF spectrum corresponds to the length of the mass packet at the temporal focus. This is largely determined by the velocity distribution of the gas in the first acceleration region between the repeller and extractor plates – more specifically, the distribution of their velocity components along the beam axis. The flatness of the fields between the plates, the response function of the detector, and any perturbing fields along the drift region can also affect the TOF peak width.

Given the requirement for all the particles to be accelerated simultaneously, the voltage applied to each plate must be switched on very fast if the ions are not generated in-situ. In order to ensure uniform acceleration of all the ions, the target voltage of each plate must be achieved before the ions have passed through the first mesh into the stronger acceleration region. In this instrument, this is achieved with a pair of fast high voltage (HV) Behlke switches with a rise time of < 10 ns.

2.1.2.4 Electron velocity-map imaging

VMI is a technique used to measure the velocity distribution of ions or electrons following a perturbing event acting on a molecular beam – such as photoionisation or photodissociation – as it passes through an interaction volume. Developed by Eppink and Parker[51] in 1997, VMI employs an electrostatic lens to map the velocity components of the ion products onto a two dimensional detector surface.

The event that occurs in the interaction volume produces an expanding Newton sphere of each ion product from every point within the volume. The electrostatic lens accelerates these Newton spheres towards a detector. As they fly, the spheres expand at a rate proportional to the velocity of the ions emerging from the interaction volume. Each Newton sphere is flattened on the detector surface producing a series of images, which are captured by a camera and compiled into a heat map. Although the Newton spheres expand in three dimensions, the detector surface measures only in two. Therefore, only velocity components parallel to the detection surface are mapped.

The central slice of each Newton sphere corresponds to those ions whose velocity components are entirely in the detector plane. The polar onion-peeling algorithm v8.5 (POP 8.5) reconstructs the original 3D Newton sphere from the heat map and extracts the central slice. The velocity information from this slice can then be translated into kinetic energy, yielding useful insight into the interaction event. The shape of the electrostatic lens produced by the plates ensures that regardless of their origin within the interaction volume, Newton spheres corresponding to the same ion products coincide on the detector surface. The maximum ion kinetic energy measurable by the regime corresponds to the maximum sphere size the detector can image, which in turn is determined by the length of the drift region, the size of the detector surface and the acceleration applied by the electrostatic lens.

The simplest arrangement of electrostatic elements required to perform VMI is very similar to that of Wiley McLaren TOF plates, as shown in Figure 2.5. Three thin and wide plates are stacked parallel to one another with a drift region and a detector located beyond the front plate. A different voltage is applied to each plate, generating two acceleration regions in the space between them. Similar to TOF MS, the ions begin their journey in the interaction volume directly between the repeller and extractor plates and are accelerated through the holes in the extractor and front plates.

The VMI setup differs from the Wiley McLaren regime in that there is no conductive mesh in the centre section of the extractor and front plates. The absence of the conductive mesh produces curved field lines around the holes in the plates, generating the necessary lensing effect to focus the ions onto the surface of the detector. Unlike TOF MS, the useful information is encoded in the location of the ion strikes on the surface of the VMI detector and so it must therefore be capable of imaging. Resolution in the time domain can provide additional information if multiple species are being imaged[144], or better velocity resolution if the central slice of the Newton sphere can be isolated[145]. However, temporal resolution is not essential when imaging electrons or other ion products of uniform mass.

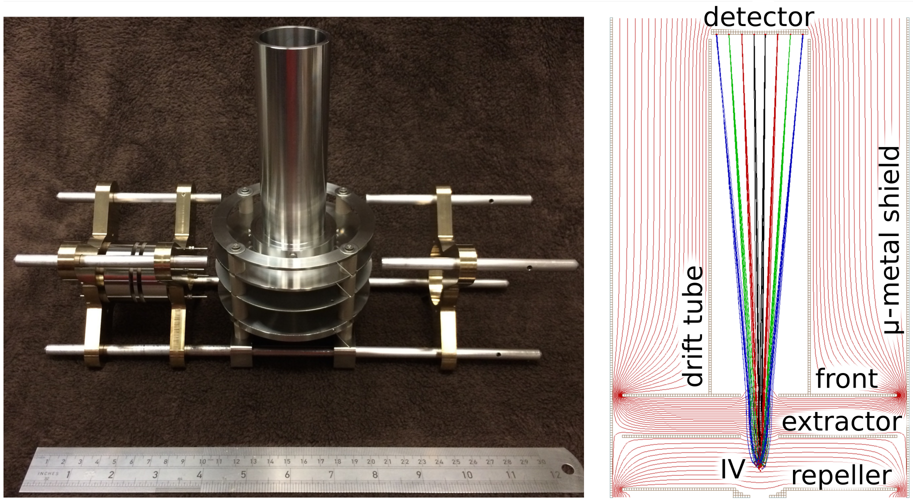

Figure 2.5: The assembly that includes the VMI electrostatic optics and a SIMION simulation of electron VMI. Each set of coloured lines corresponds to photoelectrons with uniform eKE. The eKEs of the black, red, green and blue lines are 0.1, 1.0, 3.0 and 6.0 eV respectively. For the sake of clarity, only those photoelectrons whose velocity vectors lie along the molecular beam axis are shown. The interaction volume (IV) in between the repeller and extractor plates is where the photoelectrons being imaged are generated. Regardless of where they originate within this volume, all electrons with the same velocity vector are focussed to the same point on the position-sensitive detector. The front plate, drift tube and front face of the detector are all at the same voltage, generating a field-free region in which the Newton spheres of electrons expand. A μ-metal shield encloses the entire assembly and protects it from stray electric and magnetic fields.

The focal length of the lens is defined by the point in space through which all the ions with the same velocity vector eventually pass, albeit at different times due to discrepancies in spatial origin. The focal length can be controlled by the ratio of the voltages applied to the plates. If three completely flat plates are used to accelerate the ions, the focal length is highly dependent on the initial ion kinetic energy, similar to chromatic aberration in optical lenses arising from different photon energies. The consequence is that the Newton spheres of some products coincide and are in focus and others are not, resulting in a variable velocity resolution on the flat detection surface.

In order to compensate for this achromatic aberration and ensure the same focal length for all ion kinetic energies, additional electrostatic elements can be added to introduce stabilising fields in the drift region between the front plate and the detector[146]. Alternatively, the field lines throughout the entire interaction volume can be flattened to ensure uniform acceleration before the ions pass through the curved lensing fields. This can be achieved by changing the shape of the repeller and extractor plates. In this experiment the shape of the repeller plate has been modified to include a 'sphere of exclusion' centred on the interaction volume, as shown in Figure 2.5. The diameter of this sphere is larger than the separation between the plates and therefore requires an indentation in the centre of the repeller plate corresponding to the segment of the sphere that overlaps with the plate.

In this experiment the subject of VMI is the photoelectrons released by a laser pulse incident on anions in the molecular beam. Given the sensitivity of the imaging process to small changes in ion trajectory, the entire assembly is protected from stray electric and magnetic fields by a field-free drift tube and a µ-magnetic shield.

2.1.3 Detection methods

A molecular beam of ions is essentially an electrical current of gas charge-carriers. This current is therefore the best means by which to detect the ions. The time-dependency of the ion beam can be characterised by depositing the current into an electrical circuit and measuring the corresponding change in voltage across a resistor. The larger the value of the resistor, the greater the measured voltage but due to the intrinsic capacitance of an oscilloscope, a larger resistor also corresponds to a poorer time resolution. The number of ions in a typical molecular beam is far too few to constitute a voltage detectable by an oscilloscope with a reasonable time resolution. Therefore, in order to generate a detectable current, the charge of each ion must be amplified by ~ $10^6\times$.

2.1.3.1 The microchannel plate

The microchannel plate (MCP) is a device for amplifying individual incident ions or photons into large numbers of electrons. It consists of an array of tiny holes in a thin plate of resistive glass. A HV potential difference is applied between the two flat faces of the plate. The polarity of the potential is oriented such that the rear face of the plate is more positive than the front. The holes in the plate are spaced and angled with respect to the flat faces such that incident ions and photons with trajectories near normal to the plate are likely to strike the inside surface of one of the holes rather than passing straight through or striking the front of the plate.

When an ion or photon strikes the inside of a hole it stimulates secondary emission, ejecting a shower of electrons from the surface of the glass that is accelerated by the electric field toward the rear side of the plate. These electrons in turn strike the glass surface again, each releasing further electron cascades and so on, triggering an avalanche that eventually emerges from the back side of the plate. The signal amplification or gain is a function of the potential applied between the flat faces of the plate; the higher the voltage difference, the higher the gain. However, the gain of a single MCP eventually saturates when the electrons in the surface of the glass cannot be replenished any quicker and the avalanche cannot grow further. Ultimately at the breakdown voltage of the glass, current flows through the plate spontaneously without incident ions or photons. This must be avoided as it can irreversibly damage the MCP.

However, the signal gain can be increased beyond the saturation of a single MCP by stacking multiple plates on top of each other with increasingly positive voltages applied to each successive face. The output electron avalanche emerging from the rear of the first plate becomes the input signal for the next plate. The gain from the first plate may be $\sim 10^5$ but due to the high level of incoming signal on the second plate, its gain is likely to be saturated at $\sim 10^2$, yielding a total gain of $\sim 10^7$. Maximum transmission from one plate to the next is achieved by ensuring the arrays of holes in both plates are aligned with one another and the orientation of their angles in successive plates is inverted. Because of the complimentary orientation of the angle of the holes, a two-plate arrangement is referred to as a ‘chevron’ and three-plates, a ‘z-stack’.

2.1.3.2 The scintillator

A scintillator is a simple device that converts incident radiation, such as x-rays or high-energy electrons, into visible photons. It consists of a glass substrate coated with a fluorescent material, such as a phosphor complex. In the context of molecular beam detectors, it is usually used in conjunction with an MCP. A positive HV is applied to the glass surface such that the electrons emerging from the rear of the MCP assembly are accelerated toward it. The electrons excite the phosphor at the point of impact and cause it to fluoresce visible photons. The wavelength of the photons and the persistence of the fluorescence are dependent on the phosphor compound selected. A fast phosphor for a TOF detector may have a persistence of < 1 ns. The photons are typically emitted over a broad energy band with a peak between 400 - 550 nm.

Given that the voltage applied to the rear of a MCP assembly is often hundreds of volts with respect to ground, measuring the small amplified current emerging from the device can be tricky. The scintillator, therefore, is a means of extracting the signal optically without directly coupling to the HV at the rear of the MCP. The glass substrate of the scintillator allows the fluorescence to be observed from behind. Used in conjunction with a camera to capture the fluorescence, the scintillator also provides a means by which to map the location of individual ion strikes on an MCP.

2.1.3.3 The photomultiplier tube

A photomultiplier tube (PMT) is device that converts a low intensity light signal into a measurable electrical current. It consists of a series of electrodes, called dynodes, maintained at progressively more positive voltages in order to accelerate electrons between them. This device relies on the photoelectric effect; incident photons remove electrons from the surface of the first dynode and are then accelerated toward the next in the stack. Similar to the avalanche effect in the MCP, the electrons striking the next dynode cause secondary emission, releasing a cascade that is amplified with each successive dynode. The voltages applied to the dynodes determine the overall gain of electrical current between the first and last dynodes. This may be in excess of $\sim 10^5$ with a suitable HV acceleration field. The advantage of detecting photons rather than anions is that the front dynode can be maintained at a negative HV because the incident photons have no negative charge that would repel them. By extension, the last dynode can be held at 0 V, which makes measuring the current passing through it much more straightforward than when it is floating at a positive HV.

Many ion and photon detectors incorporate a combination of MCP, scintillator and PMT components. A diagram of the TOF detector used in the instrument is shown in Figure 2.6. The MCP amplifies the incoming ion signal, the scintillator converts the current to photons and the PMT translates and amplifies the photon signal back into a current that can be measured by an oscilliscope as a voltage drop across a resistor. The imaging detector used for

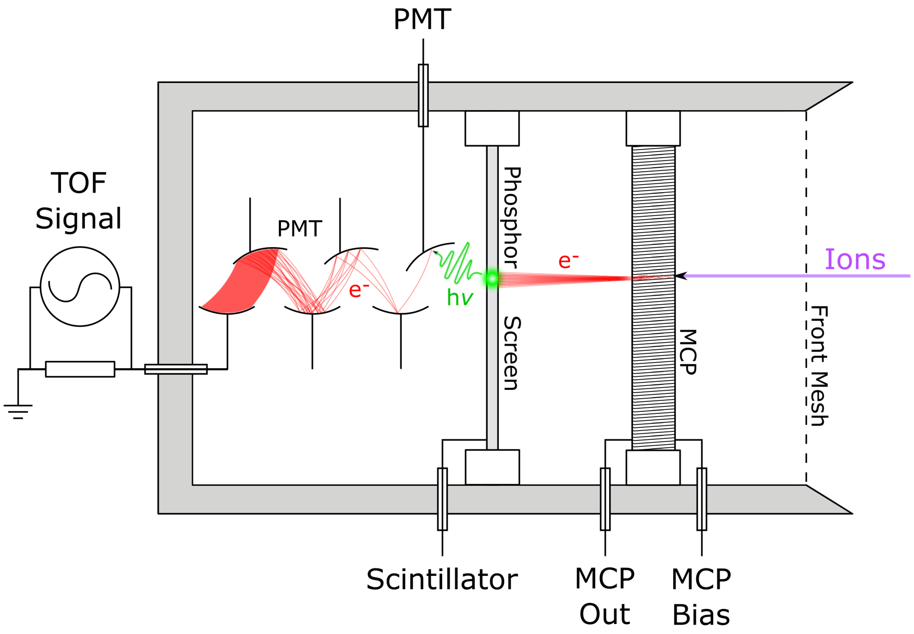

Figure 2.6: Components of the TOF detector in the instrument. The incident ions are accelerated by the field between the front mesh and the front of the MCP. The signal is amplified through the MCP and the electrons emerging from the rear are accelerated again towards the scintillator. The phosphor on the scintillator fluoresces, converting the electron current into photon energy. The PMT then translates the photon energy back into electrical current measured by the oscilloscope. The overall gain is determined by the voltage applied to each element.

VMI has the same basic elements except that a camera records the location of the flashes on the phosphor screen rather than a PMT capturing the timing of the flashes. It is worth noting that an oscilloscope has an intrinsic capacitance that lengthens the appearance of the trailing edge of a narrow voltage spike. Therefore, in order to discharge the capacitance of the oscilloscope quickly and preserve the narrow peak widths observed in TOF MS, a low value resistor, typically 50 Ω, must be used.

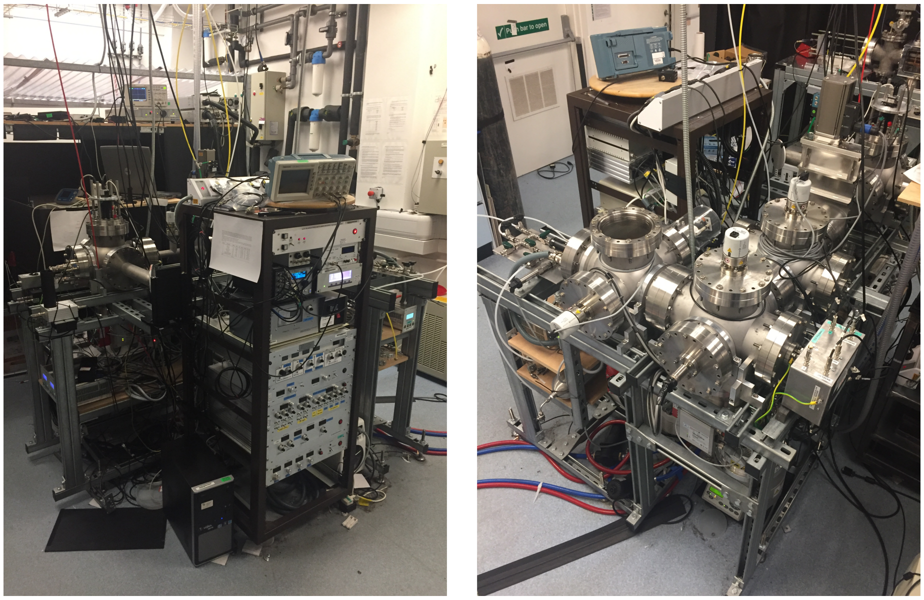

Figure 2.7: Two pespectives of the photoelectron spectrometer consisting of the stainless steel vacuum chambers and the instrument control rack, which contains all of the associated electronics.

2.2 Instrumentation

The photoelectron spectrometer is a gas-phase molecular beam experiment contained in a vacuum system, shown in Figure 2.7. An overview of the instrument is shown in Figure 2.8. The primary vacuum chambers are six-way crosses made of stainless steel with 160 mm ⊘ conflat (CF) flanges. Each of the four chambers is evacuated by a Pfeiffer HiPace® 700 turbomolecular pump (turbo). The turbo in the Source chamber, which experiences the highest gas load, is backed by a Pfeiffer ACP40 Roots pump. The other three turbos are backed by an Edwards EPX180NE hybrid turbo-drag pump. The pressure in each vacuum chamber is monitored with a Pfeiffer Compact Cold Cathode Gauge IKR 270. The Detection chamber can be isolated from the other three chambers by a VAT Series 108 UHV gate valve, which preserves a high vacuum in this chamber while the other chambers are vented.

The 6-way chambers are mounted on a framework of deep channel 41 mm steel c-section from Unitrunk. Inside the chambers, all components are fixed to aluminium bronze crosses similar to the one shown in Figure 2.9, in turn mounted on an arrangement of four 8 mm ⊘ stainless steel alignment rods with 110 mm pitch circle diameter. In this way, all components are self-aligned along the

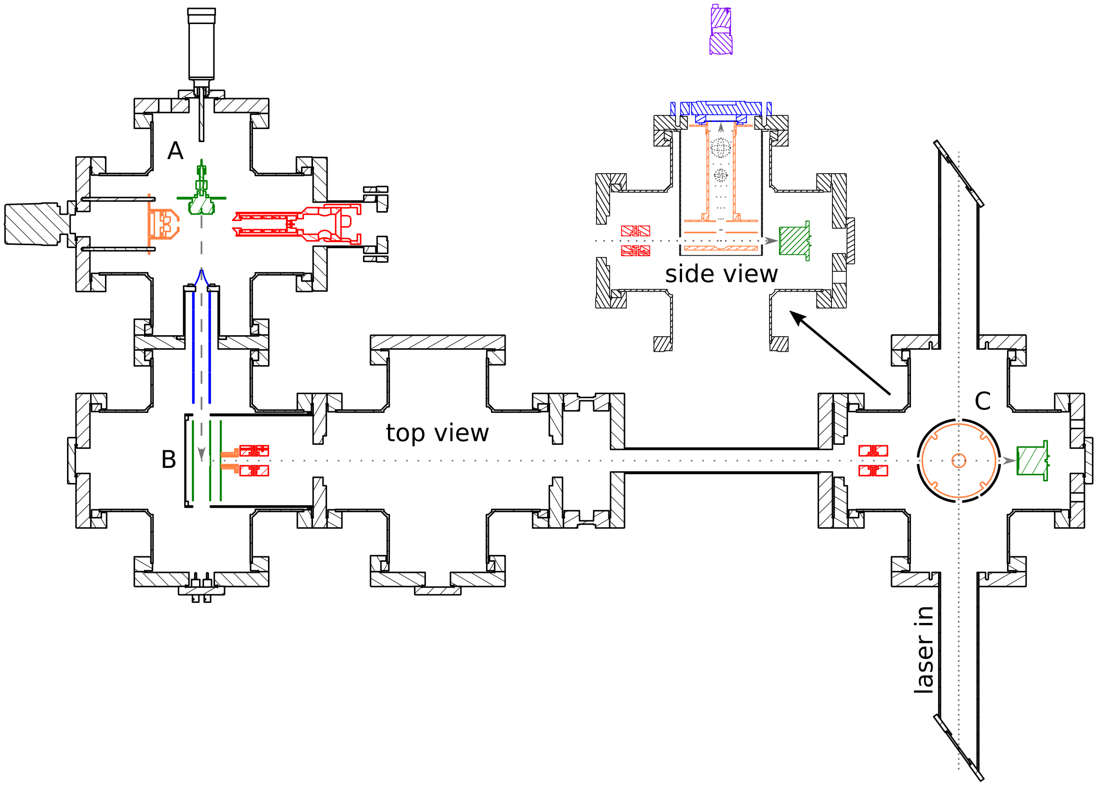

Figure 2.8: An overview of the photoelectron spectrometer. The molecular beam is initiated in the Source chamber (A) by a pulsed valve and ionised by an electron gun. The species are mass separated by a Wiley-McLaren TOF regime in the second chamber (B) and addressed in the Detection chamber (C) either by a nanosecond tuneable OPO laser system for frequency-resolved studies or a femtosecond pump-probe laser system for time-resolved studies. The photoelectrons are extracted by VMI and their impact on a phosphor screen is monitored by a monochrome Basler CCD camera external to the vacuum chamber. The 'inlet' laser window is shown mounted at Brewster's angle but can be replaced with a thin flat window normal to the laser axis in order to minimise the dispersive medium through which the femtosecond laser pulses pass.

Figure 2.9: An example of the aluminium bronze crosses on which the components inside the instrument are mounted. The alignment rods pass through the sleeves at the end of the arms and are mounted on the flanges at the end of each vacuum chamber. In this way every component is self-aligning.

beam axis. Aluminium bronze was chosen over stainless steel for its lower density and over aluminium for its anti-galling properties. Detailed design drawings and Autodesk™ Inventor® files are included in the digital appendix.

2.2.1 Vacuum chamber components

2.2.1.1 Source chamber

The Source chamber is where the molecular beam is initiated and anion species generated. A diagram of the Source chamber is shown in Figure 2.10. The ultimate pressure in the Source chamber is 3×10^{-9} mbar. When the Even-Lavie valve is operating at 200 Hz with a stagnation pressure of 3.5 bar and a pulse duration of 32 µs, the pressure in this chamber is typically ~ 5×10^{-5} mbar.

A gas sample is introduced to the instrument through a manifold system outside the Source chamber. The manifold, shown in Figure 2.11 is made from 6 mm compression fittings and includes 6 openings: 2 for introducing gas samples; 2 for attaching a bubbler for liquid samples; 1 for evacuating the system and; 1 that leads to the pulsed valve inside the chamber. The flow of gas within the manifold is managed by 5 ball valves and 3 needle valves. A Pfeiffer piezo APR

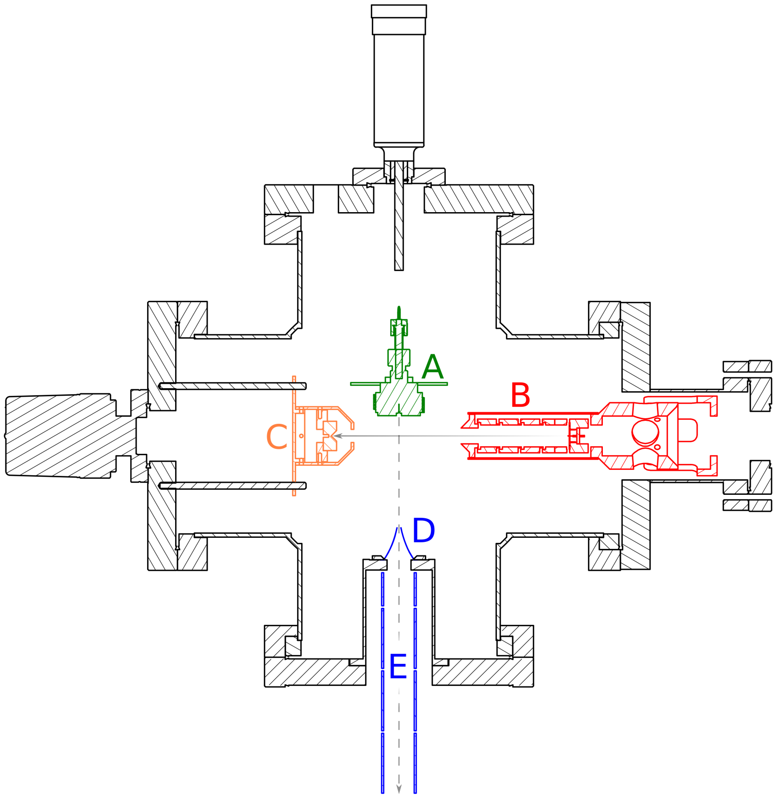

Figure 2.10: The Source chamber in which the molecular beam is initiated, ionised and skimmed, seen from above. All electrical connections (except for the electron gun) and gas feedthroughs are on the same flange as the translator, to the north of the diagram. A pressure gauge is mounted on the western flange and the flange on top of the chamber contains a window.
A – the Even-Lavie high temperature pulsed valve is mounted on the translator rod behind it. The valve can therefore be moved back and forth relative to the ionisation region.
B – the electron gun passes a beam of electrons through the gas expansion in front of the pulsed valve. All of the electrical connections for this assembly are fed through the flange on which it is mounted.
C – the Faraday cup is the electron beam dump. It consists of a conical indentation in a copper block, with a surface coat of graphite spray, enclosed in a protective case.
D – a Beam Dynamics Inc nickel skimmer with a 3 mm aperture selects the central portion of the beam as it passes into the neighbouring TOF chamber. This small aperture also ensures that the Source and TOF chambers are differentially pumped.
E – a series of four tubular electrodes make up a low voltage einzel lens that confines the expanding beam and focusses it into the middle of the TOF chamber to ensure a high ion density for mass selection.

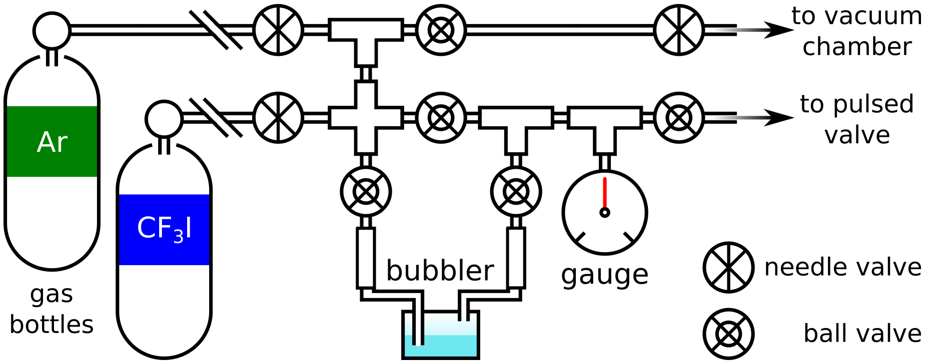

Figure 2.11: The manifold system that regulates the delivery of high pressure gas to the Even-Lavie pulsed valve. A combination of needle and ball valves make for a versatile system in which different sections can be isolated from each other and gas flow controlled. Rather than using the bubbler, particularly volatile liquid samples can be introduced to the manifold by placing a single drop in a compression fitting plug connected to one of the arms of the bubbler.

266 pressure gauge attached to the manifold monitors the stagnation pressure behind the valve. The manifold can be evacuated in two ways. A nylon tube connected to the Pfeiffer ACP40 roots pump, which backs the Source chamber turbo, can be attached to any of the inlets in the manifold to provide a rough backing line with a high throughput. Alternatively, when a more thorough evacuation is required, opening the ball and needle valves that feed directly into the Source chamber provides a much lower base pressure. However, care must be taken when opening these valves as the turbo is highly susceptible to damage from high gas loads.

An Even-Lavie high temperature pulsed valve[139] (Figure 2.10 A) offers short-duration gas pulses with high directionality and efficient adiabatic cooling. An electron gun (Figure 2.10 B) passes a beam of electrons along the central axis of the chamber perpendicular to the molecular beam axis, intercepting the gas expansion emerging from the pulse valve. The design of the electron gun is discussed in Section 2.2.1.1.1 and its performance is evaluated in Section 2.2.2.1. The pulse valve is mounted on a translator that can move it forward and backwards relative to the electron beam, as shown in Figure 2.12. In this way, the point at which the gas is ionised can be varied. The gas line between the flange and the valve is coiled, which allows it to stretch and compress during translation. In these studies, argon was used as a backing gas, typically at 2.0 - 4.0 bar, depending on the analyte. Electron bombardment at 300 eV electron kinetic energy ionises the Ar gas, releasing several low kinetic energy electrons that are captured by the analyte in the molecular beam expansion[141,142].

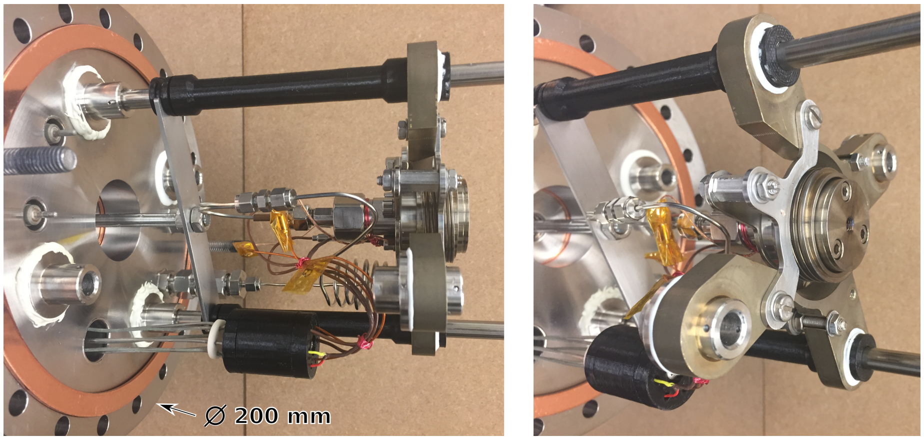

Figure 2.12: Two perspectives of the Even-Lavie valve (Figure 2.10 A) mounted on its aluminium bronze cross on the alignment rods. The translator rod can be seen behind the valve, protruding through the flange. The black components are bespoke 3D printed PLA parts. The six electrical contacts are contained in a PLA casing that preserves the alignment of the pins relative to their respective connectors.

Given the need for the Even-Lavie valve to translate smoothly backward and forward on the alignment rods, sleeves were inserted into the mounting holes on the aluminium bronze cross on which the valve is mounted. These sleeves reduce the friction of sliding and ensure that the cross does not snag or catch on the stainless steel alignment rods. Although aluminium bronze has anti-galling properties, the cross did not slide smoothly enough on the rods on its own. Stainless steel sleeves were inserted but these also eventually snagged on the rods. However, 3D printed polylactic acid (PLA) proved to be the ideal material. It is soft enough to slide on the rods, even under considerable lateral force, and has a low rate of outgassing, to the extent that it has no noticeable effect on the ultimate pressure measured in the vacuum chamber. Residual gas analysis (RGA) has not yet been performed in the chamber to identify any potential contaminants but none have been observed in the TOF spectra.

2.2.1.1.1 Electron gun The electron gun (Figure 2.10 B) is comprised of a 150 µm ⊘ W filament cathode and a series of consecutive concentric tubular electrodes, bespoke manufactured by Durham Precision Engineering Ltd and shown in Figure 2.13. Under normal operating conditions, a current of up to 3.2 A is passed through the filament, releasing electrons into the vacuum. The fields between the electrodes, which operate at the voltages listed in Table 2.1, accelerate and focus the electrons into a beam, as shown by the simulation in Figure 2.1.

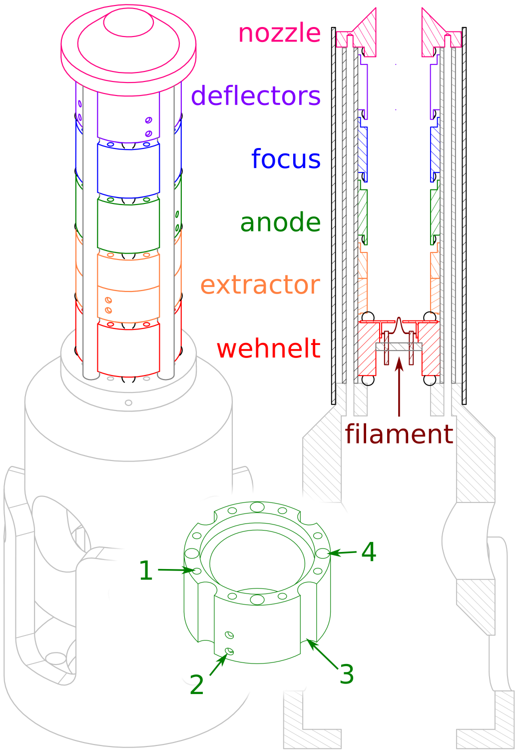

Figure 2.13: A sectional view of the tubular electrodes stacked in the electron gun (Figure 2.10 B). The electron beam is initiated at the filament and is accelerated, collimated and focussed by the electrodes that follow. The inset view of a single element shows how the electrodes receive their respective voltages (1 & 2) and are stacked and aligned (3 & 4).

The inset view of the single anode element in Figure 2.13 demonstrates how the voltages are delivered to each element and how the assembly is held together. There are eight holes (1) arranged around the rim of each tube that pass through its entire length, carrying the insulated wires that deliver the voltages to each element. One of these holes on each element is intercepted by two tapped holes (2) entering from the side wall of the tube. These tapped holes hold grub screws that secure one wire to each element thereby making electrical contact. Four cylindrical grooves (3) run along the outer face of each tube, in which ceramic rods sit to keep the elements aligned. Similarly, there are four hemispherical divots (4) on the top and bottom faces of each tube in which 1/8" ⊘ SiN balls rest in order to stack consecutive elements in alignment and maintain electrical isolation. A stainless steel sheath surrounds the entire assembly to contain the strong electric fields.

Table 2.1: The voltages applied to the various electron gun elements shown in Figure 2.13.

Element	Voltage wrt ground (V)	Figure 2.13 element
filament	− 300	A
Wehnelt	− 340	B
extractor	0	C
anode	+ 2400	D
focus	+ 300	E
deflectors	± 5	F

Each element in the electron gun shown in Figure 2.13 has a different effect on the beam shape and current: the filament floating voltage determines the total kinetic energy of the electrons in the beam; the voltage difference between the Wehnelt and filament determines the kinetic energy distribution of the electrons and hence the quality of the beam's focus; the extractor voltage determines the magnitude of the current drawn off the filament; the ratio of the anode and focus voltages determine the focal length of the beam and tightness of focus; and the deflectors at the nozzle of the gun steer the beam vertically and laterally to ensure optimal overlap with the expanding molecular beam. The performance of the electron gun is discussed in Section 2.2.2.1.

2.2.1.2 Time-of-flight chamber

The TOF chamber is where the anions in the molecular beam are extracted and separated into mass-packets with TOF MS. A diagram of the TOF chamber is shown in Figure 2.14. The ultimate pressure of the TOF chamber is 1×10^{-9} mbar and its operating pressure is $\sim 5 \times 10^{-7}$ mbar.

Once ionised, the molecular beam then passes through a Beam Dynamics Inc nickel trumpet skimmer with a 3 mm aperture (Figure 2.10 D). The skimmer is mounted directly onto a 'top-hat' extension tube connected to the flange of the neighbouring TOF chamber. This effectively extends the TOF chamber into the middle of the Source chamber; the narrow skimmer aperture ensures that the two chambers are differentially pumped. This prevents the higher background gas pressure in the Source chamber from interfering with the skimmed beam.

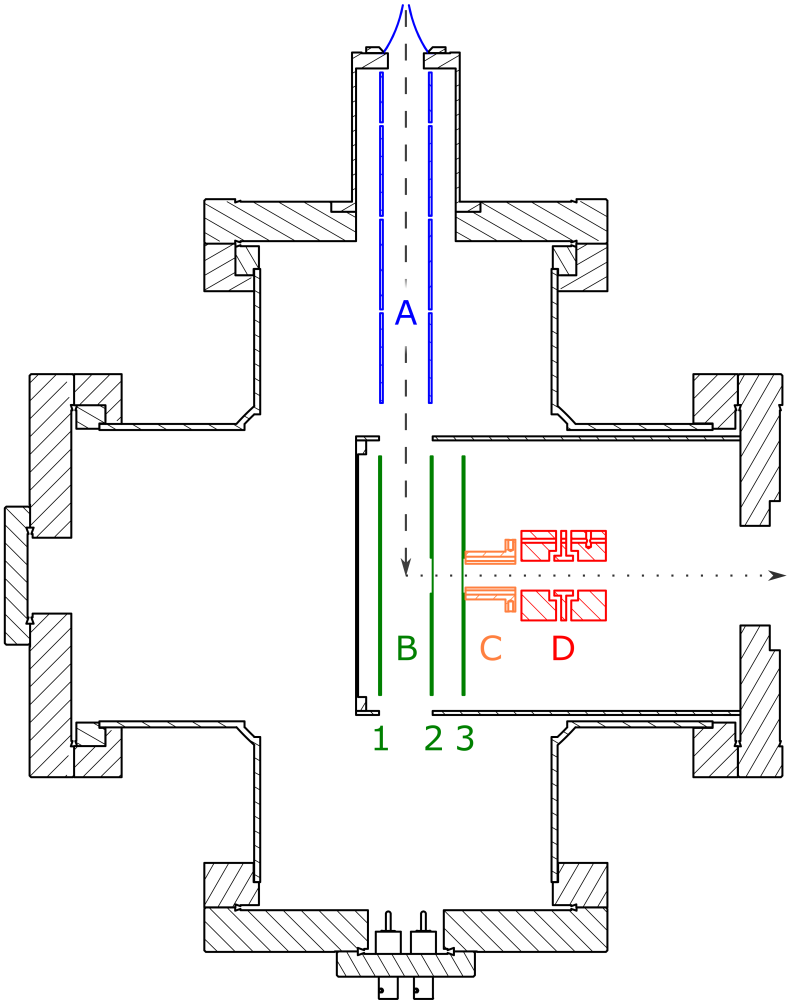

Figure 2.14: The vacuum chamber containing the TOF electrostatic elements seen from above. Electrical feedthroughs are located on the flanges to the south and west of the diagram and a pressure gauge is mounted on top of the chamber.
A – the low voltage einzel lens that confines the expanding molecular beam and focuses it into the centre of the TOF plates.
B – the three flat plates that comprise the Wiley-McLaren TOF regime. The repeller plate (1) and the extractor plate (2) are pulsed to a negative HV when the ions are in the space between them. This accelerates them orthogonally through a hole in the extractor plate that is covered with a fine gauze. The ions continue to accelerate toward the front plate (3), which is held at 0 V.
C – the deflectors (as shown in Figure 2.3) make small adjustments to the trajectory of the beam in order to maximise the transmission of ions down the length of the instrument.
D – an einzel lens (as shown in Figure 2.2), collimates the beam to minimise ion losses due to residual radial momentum in the beam.

Four consecutive concentric ring electrodes are mounted inside the top-hat and protrude into the TOF chamber (Figure 2.10 E & 2.14 A). These electrostatic elements act as a very low voltage einzel lens (< 1 V), confining the anions and guiding them toward the TOF assembly at the centre of the chamber.

The TOF assembly is mounted on four stainless steel alignment rods and is composed of a three-plate Wiley-McLaren TOF regime[143] followed by a set of vertical and lateral electrostatic deflectors and an einzel lens. These elements are surrounded by a stainless steel tube that protects the slow incoming molecular beam from stray field perturbations. The incoming molecular beam enters the TOF assembly between the rearmost 'repeller' and middle 'extractor' TOF plates (Figure 2.15). The direction the anions are extracted is perpendicular to the original direction of travel, ensuring that excess neutral gas in the beam does not enter the Detection chamber.

The repeller and extractor TOF plates are pulsed on to – 3.00 kV and – 2.68 kV respectively, while the front plate (Figure 2.15) remains at 0 V. The TOF plates are 1 mm thick and 120 mm ⊘. The first two plates are separated by 25 mm and the middle and front plates by 15 mm.

The central apertures in the middle and front plates through which the anions pass are 20 mm ⊘ and a fine gauze with 88% open area is fixed over each with conductive adhesive. The gauze ensures the fields between the plates are as flat as possible, avoiding lensing effects that would deflect the trajectory of the anions. Given the field strength is greater in the space between the extractor and front plates than between the repeller and extractor plates, the anions are accelerated most in this region. Therefore the gauze is attached to the sides of the plates that face this region in order to ensure minimal deviation in their trajectories.

The vertical and lateral deflectors (also shown in Figure 2.3) are quadrants of a tubular electrode arranged in a circle and mounted immediately after the front grounded TOF plate. The primary role of these elements is to compensate for minor misalignment of the TOF plates and for any residual momentum in the beam from its original trajectory before extraction. Therefore, the voltages applied to each deflector pair must be optimised for the m/z of the analyte.

An einzel lens (also shown in Figure 2.2) is positioned after the deflectors in order to collimate the molecular beam for its trajectory down the length of the instrument. This einzel lens typically operates at – 1 kV and the total drift length is 1.2 m. The composition of the molecular beam is revealed in the TOF spectrum produced when the anions strike a MCP detector in the Detection chamber. The performance of the TOF regime is evaluated in Section 2.2.2.2.

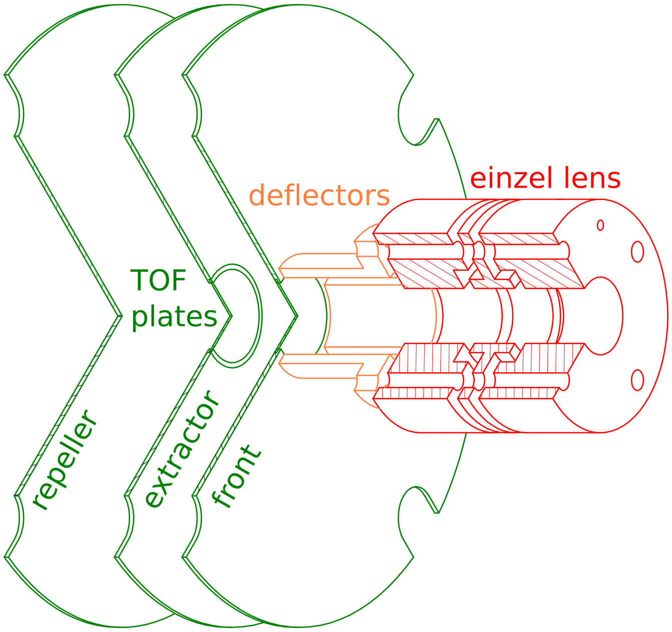

Figure 2.15: The Wiley-McLaren TOF plates, deflectors and einzel lens in the TOF chamber (Figure 2.14 B, C & D). The repeller and extractor plates are pulsed to a negative HV when the ions are directly in between them in order to accelerate them through the apertures in the extractor and front plates. These apertures are covered in a fine gauze, which maintains a flat acceleration field between the plates. The lateral and vertical deflectors compensate for both residual momentum in the beam following the supersonic expansion and any misalignment of the TOF plates. The einzel lens collimates the emerging molecular beam in order to maximise the transmission of ions into the Detection chamber.

2.2.1.3 Detection chamber

The Detection chamber is both where the composition of the molecular beam is analysed and where measurements using PES are made. A schematic of the Detection chamber is shown in Figure 2.16. The ultimate pressure of the Detection chamber is 1×10^{-9} mbar and its operating pressure is up to ~ 5×10^{-7} mbar.

Upon exiting the TOF chamber, the molecular beam passes through an empty 6-way chamber, a gate valve and through a drift tube. Along the beam axis within the Detection chamber is an einzel lens, the VMI electrostatic elements and the TOF detector. At lower voltages (~ +1 kV), the einzel lens focuses the collimated beam onto the surface of the detector for maximum TOF signal. At higher voltages (~ +2 kV), the einzel lens focuses the molecular beam onto the laser axis, which passes perpendicular to the ions through the centre of the chamber. The laser systems and optical bench are discussed in detail in Appendix A.2.

The TOF detector is a Photonis Inc Advanced Performance Bi-Polar Time-of-Flight detector. It consists of a single MCP coupled to a phosphor scintillator and a PMT. The recommended operating parameters are given in Appendix A.1.7. An example TOF spectrum is shown in Figure 2.20.

The VMI assembly consists of a three-plate stack and a drift tube, as shown in Figures 2.5 and 2.17. The interaction volume where laser addresses the molecular beam lies half way in between the repeller and extractor plates. The VMI plates are aligned such that the molecular beam enters from the side and the photoelectrons produced in the interaction volume are projected vertically, perpendicular to both the ion beam and the laser axis. The plates themselves are 110 mm ⊘, the hole in the extractor plate is 15 mm ⊘ and the hole in the front plate is 16 mm ⊘. The separation between the repeller and extractor plates is 20 mm and between the extractor and front plates is 16 mm.

The surface of the repeller plate is not an single flat plane; at the centre of the plate there is an indentation in the shape of a spherical segment, the centre of which coincides with the interaction volume. This indentation ensures that the electric field lines in the interaction volume are flatter than they would be in the absence of the indentation and therefore distinct from the lensing field around the hole in the extractor plate. This in turn reduces the sensitivity of the VMI to the spatial origin of the photoelectrons and improves the energy resolution of the photoelectron spectra.

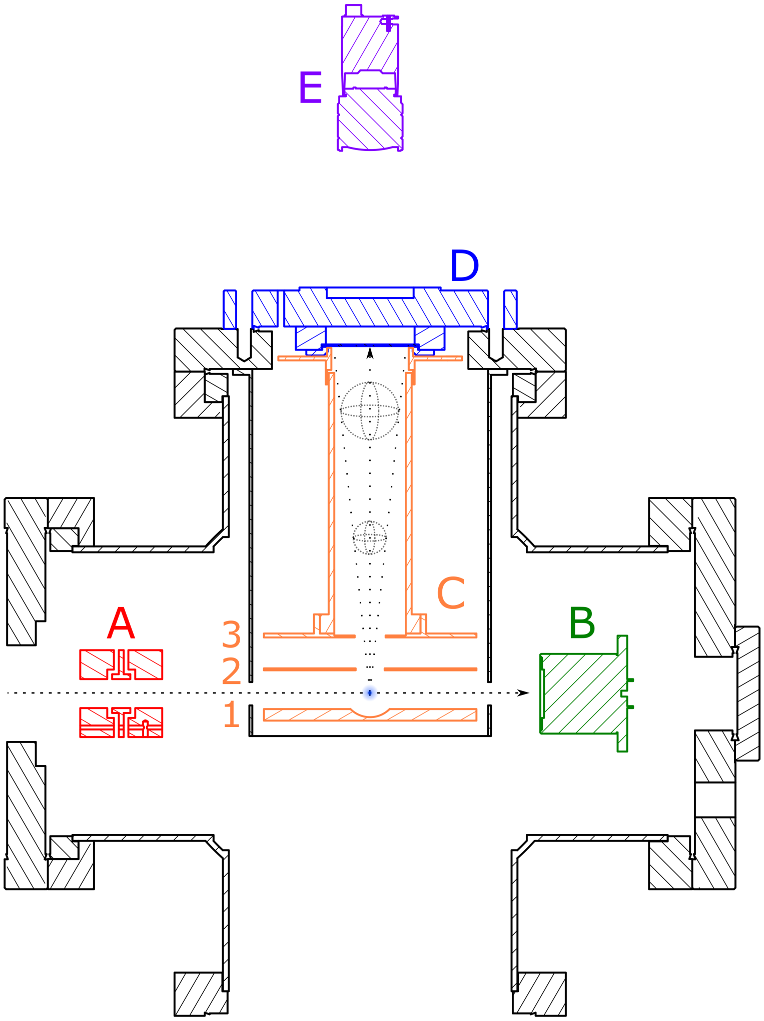

Figure 2.16: A side view of the contents of the Detection chamber, seen from the 'entry' laser window. All electrical feedthroughs (except for the VMI detector) are on the terminal flange behind the TOF detector. The pressure gauge is mounted half way along the narrow drift tube, not shown on this schematic.
A – the second einzel lens along the TOF drift path focusses the molecular beam into the interaction volume at the centre of the chamber.
B – the TOF detector that measures the TOF spectrum shown in Figure 2.20.
C – the VMI plates generate an electric field that projects the photoelectrons produced in the interaction volume upwards. A SIMION simulation of electron VMI can be seen in Figure 2.5. The bottom repeller plate (1) has a hemispherical indentation in the centre of it to improve the focussing capability of the regime. This plate is switched on rapidly as the laser pulse addresses the mass packet in the interaction volume. The extractor plate (2) is kept static at a small negative voltage while the front plate (3) is kept at the same HV as the drift tube and the front MCP surface of the VMI detector.
D – the position-sensitive VMI detector amplifies individual photoelectron strikes such that they can be seen on the phosphor scintillator from outside the chamber.
E – the monochrome Basler CCD camera records the flashes produced by the scintillator and sends them to the analysis software on the computer.

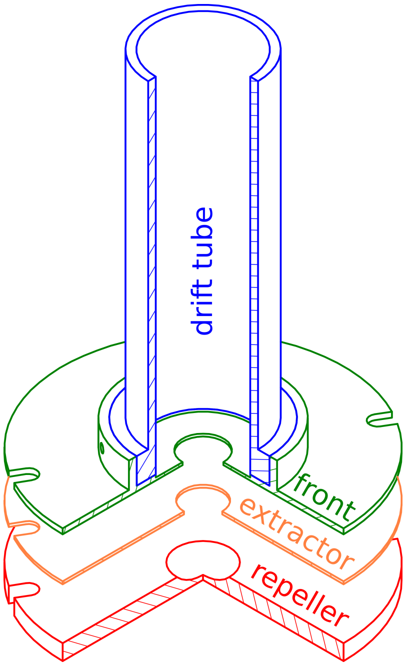

Figure 2.17: A cutaway view of the VMI plates and drift tube (Figure 2.16 C), at the top of which is the position-sensitive detector. The repeller plate is pulsed on when the photoelectrons are generated in the interaction volume between it and the extractor plate. The extractor plate remains at small negative voltage in order to prevent ions from passing up the drift tube and introducing noise on the detector. The front plate, drift tube and front face of the detector are held at a static positive HV, providing the field-free region in which the Newton spheres of photoelectrons expand as they travel toward the detector.

A Photek Ltd VID 240 imaging detector lies at the end of the field-free VMI drift tube. This consists of a chevron stack of MCPs followed by a scintillator coated with P43 phosphor. The recommended operating parameters are given in Appendix A.1.8. A modified front plate has been attached to the detector in order to protect insulating components from oncoming photoelectrons and so prevent perturbations in the field-free drift region arising from charged surfaces. A μ-metal shield encases the entire assembly to eliminate any stray magnetic fields that would perturb the trajectory of the photoelectrons within the drift tube.

Unlike the Wiley McLaren TOF regime, which applies pulsed voltages to both the repeller and extractor plates in order to accelerate the ions, this VMI assembly applies a pulsed voltage to only one plate. A Directed Energy Inc (DEI) PVM-1001-N pulsed voltage module delivers a 480 V pulse of duration 113 ns to the repeller plate. The extractor plate is maintained static at − 35 V in order to reduce the number of ions passing through the plates and causing noise on the detector. The ion beam experiences a small deflection from its original trajectory as it passes between the repeller and extractor plates but it is insufficient to cause it to miss the TOF detector surface. The front plate is maintained static at +650 V and in order to maintain a field-free drift region after the front plate, the same HV is also applied to both the drift tube and the front face of the first MCP. The performance of the VMI regime is evaluated in Section 2.2.2.3.

2.2.2 Characterisation of the instrument

The parameters under which the instrument operates best are detailed in Appendix A.1. The character and performance of the instrument are evaluated below in order to demonstrate its capabilities and report necessary calibration constants.

2.2.2.1 Electron gun performance

The focal point of the electron beam is monitored visually as it causes the gas pulse emerging from the Even-Lavie valve to fluoresce. The cross-section of the beam, obtained from a long-exposure image of the fluorescing gas, is shown in Figure 2.18. The shape fits well to a Gaussian profile with a full-width half-maximum (FWHM) of 0.6 mm but displays an elongated trailing edge as a result of the gas continuing to fluoresce as it expands.

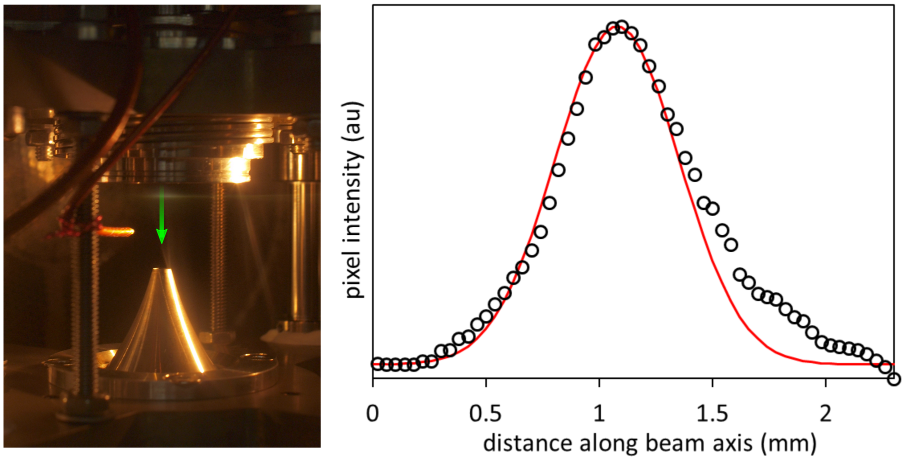

Figure 2.18: The electron beam generates a visible glow discharge as it passes through the supersonic expansion in front of the pulsed valve. The beam waist at the focal point was measured as a cross section of the pixel intensities along the molecular beam axis, indicated by the green arrow. A Gaussian fit, indicated by the solid red line, was applied to the rising edge of the profile. The FWHM of this peak is 0.6 mm. The trailing edge was excluded from the fitting because the gas continues to fluoresce as it expands into the vacuum, giving rise to the elongated decay profile.

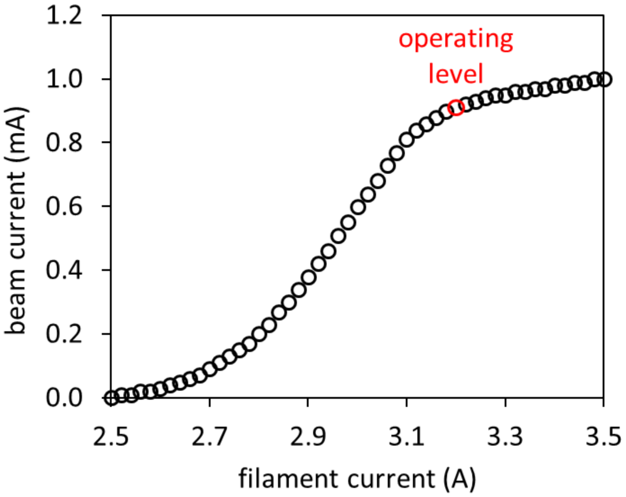

Figure 2.19: The beam current produced by the electron gun as a function of the current passed through the W filament as it is turned on.

The electron beam is dumped into a copper block (Figure 2.10 C) with a conical indentation, covered in a thin graphite coating to improve collection efficiency. The current passing through the block is measured by the voltage drop it produces across a resistor. Under normal operating conditions, the beam current is 0.83 mA and is best controlled by varying the current passed through the filament, as shown in Figure 2.19. These values were measured when the electron gun was first turned on. The beam current tends to settle during operation and gradually reduces by as much as ~ 10 % over the course of the first hour of operation. The recommended operating level is 3.2 A. This will ensure a sufficiently high beam current for most experiments and a filament lifetime in the order of months/years rather than weeks/days/hours. If the signal levels are too high and risk damaging the detectors, the quickest way to reduce the number of ions is to turn down the filament current.

2.2.2.2 Time-of-flight performance

The performance of the Wiley-McLaren TOF regime in the instrument is shown in Figure 2.20. The spectrum consists of several cluster series of $n \times C_6F_6$ molecules bound to O_2^-, H_2O^- and O_4^-. The peaks have a finite width, as demonstrated by the inset plot. The FWHM of this peak is 23 ns. To a first approximation, the peak width is independent of m/z. The convergence of the TOF of m/z and m/z+1 yields a mass resolution of $\frac{m/z}{\Delta m/z} = 1600$.

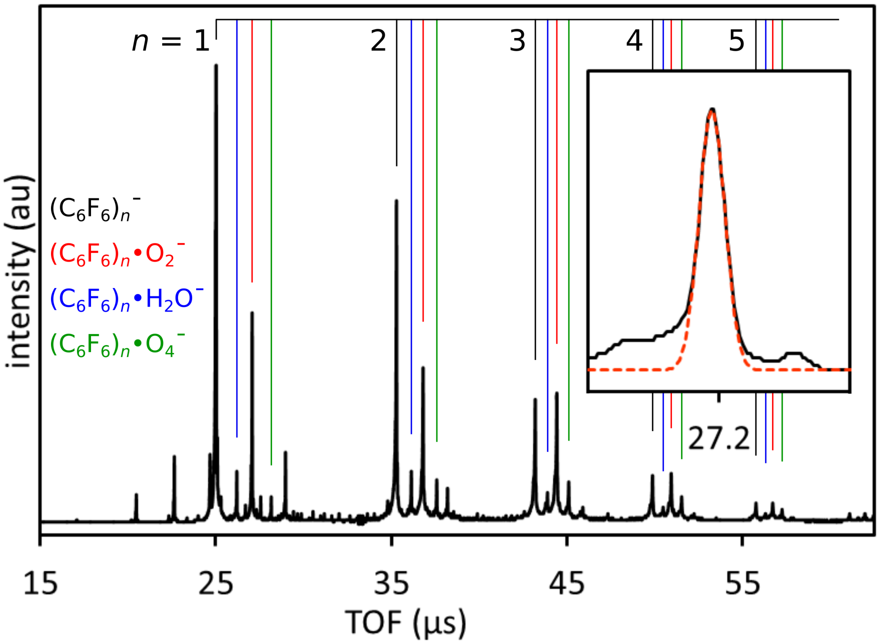

Figure 2.20: An example TOF spectrum consisting of clusters containing $(C_6F_6)_n^-$, O_2^-, H_2O^- and O_4^-. The inset plot shows a Gaussian profile (red dashed line) fitted to a sample peak in the spectrum. The FWHM of this peak is 23 ns, corresponding to a TOF mass resolution of $\frac{m/z}{\Delta m/z} = 1600$.

Table 2.2: The calibration constants for translating the time axis in the TOF spectrum to units of m/z in accordance with Equation 2.3.

Coefficient	**Value**
c_1	0.293
c_2	0.139
c_3	− 2.86

The calibration of the TOF spectrum is based on the quadratic equation,

$$m/z = c_1 t^2 + c_2 t + c_3, \tag{2.3}$$

where t is the TOF in units of µs. The coefficients in Table 2.2 are only valid when the Wiley-McLaren repeller plate operates at − 3.00 kV and the einzel lenses are not operating. These coefficients produce an optimum fit for $m/z > 100$ because the initial acceleration of the anions introduces a deviation from the model in Equation 2.3.

2.2.2.3 Velocity-map imaging performance

The photoelectrons generated when the laser pulse addresses the anions are projected onto the Photek Ltd detector by the electric fields in the VMI regime. Over the course of hundreds or thousands of laser shots, a heat map of electron strikes is generated from the cumulative image of the flattened Newton spheres as they strike the detector surface. The central slice of each Newton sphere is extracted by the POP 8.5 algorithm. The intensity profile of the cross section of this central slice contains the information necessary to generate a photoelectron spectrum. The abscissa with units of pixel number must be translated into units of eV. The energy axis scales as $E = kR^2$, where E is the energy, R is the pixel number and k is a scaling calibration constant, which must be derived from a known spectrum. The intensity profile of the photoelectron spectrum, I_{PE}, is derived from the intensity profile of the cross section of the central slice, I_{XS}, by the relationship $I_{\mathrm{PE}} = \frac{I_{\mathrm{XS}}}{R}$.

Figure 2.21 shows the VMI heat map and corresponding photoelectron spectrum of O_2^- at $h\nu = 2.95$ eV. This spectrum was used for calibration because of the 16 resolvable and assignable peaks. These peaks correspond to the vibrational levels within the X $^3\Sigma_g^-$ (*i*), a$^1\Delta_g$ (*ii*), and b$^1\Sigma_g^+$ (*iii*) electronic states of neutral O_2. The anisotropy of the PAD in the heat map yields $\beta_2 = -1$, indicating that the electron was removed from a p- or π-like orbital, as would be expected for the π* HOMO of O_2^-. The measured spectrum is shown in the

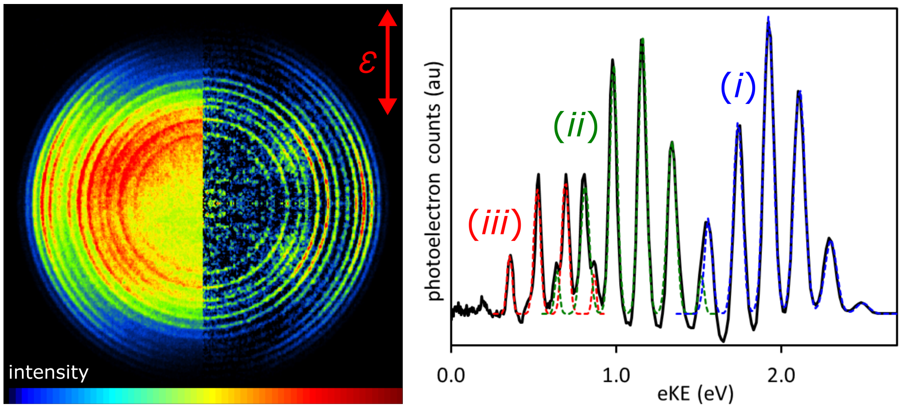

Figure 2.21: The VMI heat map and corresponding photelectron spectrum of O_2^- at $h\nu = 2.95$ eV used to calibrate the VMI measurements. On the left of the heat map is the raw image and on the right is central slice of the Newton spheres reconstructed by the POP 8.5 algorithm. There are three series of narrow peaks in the spectrum that correspond to the vibrational levels within the X $^3\Sigma_g^-$ (i), $a^1\Delta_g$ (ii), and $b^1\Sigma_g^+$ (iii) electronic states of neutral O_2.

solid black line and the coloured Gaussian profiles have been fitted according to the Constants of Diatomic Molecules in the NIST Webbook[147]. When the repeller plate is pulsed to – 480 V and the VMI focus is optimised, the calibration constant is found to be $k = 2.816 \times 10^{-5}$. The energy resolution of the VMI derived from the peak widths in this spectrum is $\Delta E/E = 2.6\%$.

Chapter 3

Photoelectron spectroscopy of anionic clusters containing C_6F_6

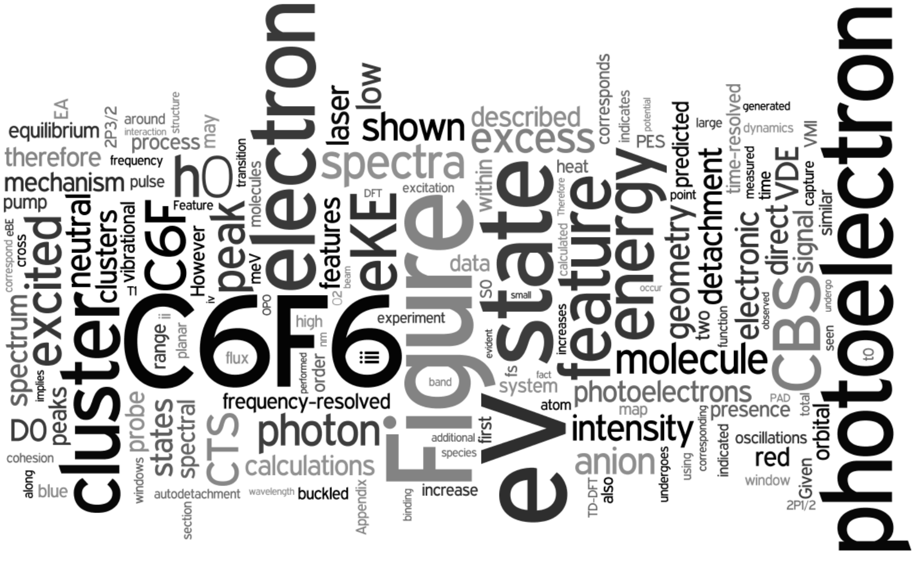

3.1 Frequency-resolved photoelectron spectroscopy of $(C_6F_6)_n^-$ clusters

3.1.1 Motivation

The dipole-bound states (DBSs) observed in systems such as uracil[1], acetonitrile[148], nitromethane[33] and the dimer anion of *para*-benzoquinone[71] have been shown to act as doorway states in the formation of their respective VBS anions. The DBS therefore plays an important role in the fundamental chemical reaction of electron capture by a polar molecule, $M + e^- \rightarrow M^-$. However, there is an absolute theoretical limit of 1.625 D below which the permanent dipole of the molecule is too small to generate a sufficiently large binding interaction with the excess electron[13,15]. Therefore this phenomenon cannot form part of the mechanism by which non-polar molecules capture electrons.

According to calculations performed by Voora and Jordan[97], the non-polar molecule C_6F_6 is predicted to host a correlation-bound state (CBS) of the anion. Similar to the DBS, the excess electron in a CBS occupies a large and diffuse spherical orbital and is weakly-bound, stabilised principally by charge:induced-dipole interactions with the valence system of the neutral core molecule. The CBS of $C_6F_6^-$ is calculated to have a binding energy of 140 meV and is posited to serve as the doorway state in the electron capture mechanism, $C_6F_6 + e^- \rightarrow C_6F_6^-$. A CBS has only ever been spectroscopically observed once before, in the trimer anion of *para*-toluquinone[42]. The following results constitute the first of my attempts to generate and spectroscopically characterise a CBS of $C_6F_6^-$.

3.1.2 Methodology

A gas sample containing C_6F_6 is prepared by passing 3.0 bar of Ar buffer gas over a reservoir of liquid C_6F_6 within the manifold system described in Section 2.2.1.1. The vapour pressure[149] of C_6F_6 is 87 mbar at 293 K. A single drop placed in a terminating compression fitting in the manifold system is therefore sufficient to produce a vapour composition of ~ 3 %, enough for the signal to persist in the mass spectrum for the duration of weeks. A molecular beam is initiated by injecting the gas mixture into the vacuum through the Even-Lavie pulsed valve. $(C_6F_6)_n^-$ clusters are generated in the supersonic expansion by intersecting it with 300 eV electrons in a beam produced by the electron gun described in Section 2.2.1.1.1.

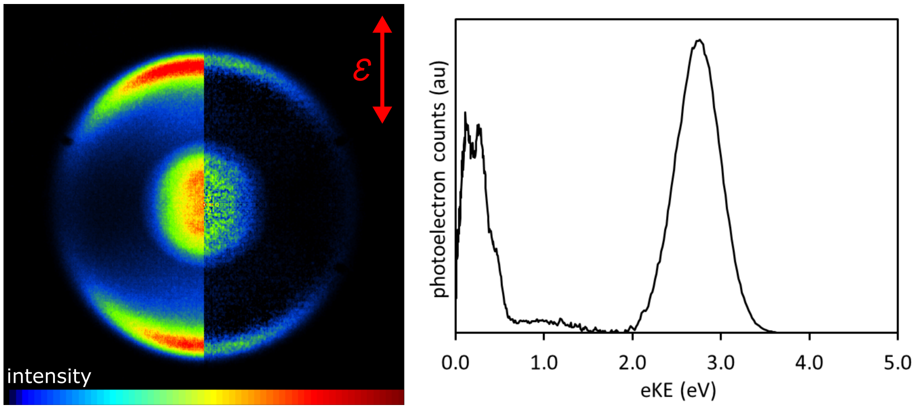

Figure 3.1: The VMI heat map and corresponding photoelectron spectrum of $C_6F_6^-$ addressed by a single photon at $h\nu = 4.3$ eV (288.34 nm). The left side of the heat map displays the raw data captured by the camera. The right side is the central slice of the Newton spheres reconstructed by the POP 8.5 algorithm. The red arrow indicates the polarisation of the laser.

The $(C_6F_6)_n^-$ clusters are isolated in the beam by orthogonal extraction in a Wiley-McLaren TOF mass spectrometer, as described in Section 2.2.1.2. The mass packet corresponding to $(C_6F_6)_n^-$, $m/z = n \times 186$, is addressed by a tuneable nanosecond OPO laser system, described in Appendix A.2.1. The photoelectrons emerging from the interaction volume are velocity-mapped in a VMI spectrometer, described in Section 2.2.1.3. The location of each electron strike on the detector, described in Section 2.1.3, is recorded by a charge-coupled device (CCD) camera, compiled into a heat map and analysed in the software described in Appendix A.3.1.

In these experiments, $h\nu$ was varied using the nanosecond OPO laser system described in Appendix A.2.1. Photon energies in the range $3.1 \leq h\nu \leq 5.8$ eV ($399.9 \geq \lambda \geq 213.8$ nm) were used at increments of 0.1 or 0.5 eV. The integration time for recording images was varied in order to obtain a VMI heat map and corresponding photoelectron spectrum that was smooth and relatively free of noise. An example VMI heat map and photoelectron spectrum are shown in Figure 3.1. The set of spectra for each species, n, is gathered into a false colour plot with a common eKE axis and $h\nu$ abscissa. Each spectrum is normalised by the integrated area under its line, which corresponds to the total photoelectron yield within the integration time. This method of normalisation means that the wavelength-dependence of the laser intensity, the integration time at each wavelength and the cross section of the analyte are all immaterial.

Density functional theory (DFT) and time-dependent density functional theory (TD-DFT) calculations were performed by Cate Anstöter. Unless specified otherwise, these calculations were all executed in the QChem 4.4 package[150] with the CAM-B3LYP functional[151] and the Dunning aug-cc-pVDZ basis set[152].

The frequency-resolved spectra of $C_6F_6^-$ are shown in Figure 3.2. Feature (*i*) corresponds to the direct detachment process, whereby the excess electron is removed from the singly-occupied highest occupied molecular orbital (SO-HOMO) of the anion's D_0 state, leaving behind a neutral molecule in the S_0 state. The VDE is derived by extrapolating the peak back to the photon energy, $h\nu$, where the maximum of this feature first emerges. Similarly, the ADE is derived from the photon energy where the onset of the peak first appears. From these data, the VDE is calculated to be 1.60 ± 0.07 eV and the ADE, 1.0 ± 0.1 eV. The VDE compares favourably to previous studies, where it has been measured[95,96] to be around 1.55 eV. The ADE is a little higher than previously measured, where it was found to be 0.7 - 0.8 eV.

Cate's calculations, the results of which are depicted in Figure 3.3, reaffirm that the equilibrium geometry of the S_0 state is planar with D_{6h} symmetry whereas the D_0 state is buckled with C_{2v} symmetry, as shown in Figure 3.4. The EA is predicted to be 0.55 eV and the VDE, 1.70 eV. These values compare favourably with previous calculations of VDE = 1.78 eV[96] and EA = 0.53 eV[92]. When the photoelectron is ejected in a direct detachment process, the neutral molecule is left not in its own equilibrium geometry but rather in the original geometry of the anion. The discrepancy between the calculated VDE and EA is reflective of the significant energy required to bend the neutral molecule into the equilibrium geometry of the anion.

Feature (*i*) in Figure 3.2 has a broad Gaussian profile without any distinctive internal structure. The shape and eKE of this peak can be explained by considering the reflection principle, depicted in Figure 3.5. The projection of the initial wavefunction in the D_0 state onto the final state, indicated by the blue column, determines the possible transitions according to the degree of Franck-Condon overlap between the initial and final wavefunctions. The broad peak shape of feature (*i*) implies a favourable Franck-Condon overlap not with the $v' = 0$ vibrational level of the S_0 state but instead with a collection of closely-spaced high-energy vibrational levels far from equilibrium and which cannot be spectrally resolved. This interpretation explains not only the discrepancy between the calculated EA and the measured and predicted VDE but also the lack of vibrational structure of the S_0 state. Indeed, given that the ADE is also substantially larger than the predicted EA, it can be concluded that the $v' = 0 \leftarrow v = 0$ transition is impossible and therefore an experimentally derived EA cannot be obtained from the spectra.

The PAD of feature (*i*) is strongly anisotropic with $\beta_2 = +2.0$ when $h\nu < 3.0$ eV. The reason for this is unclear as the DFT calculations, presented in Figure

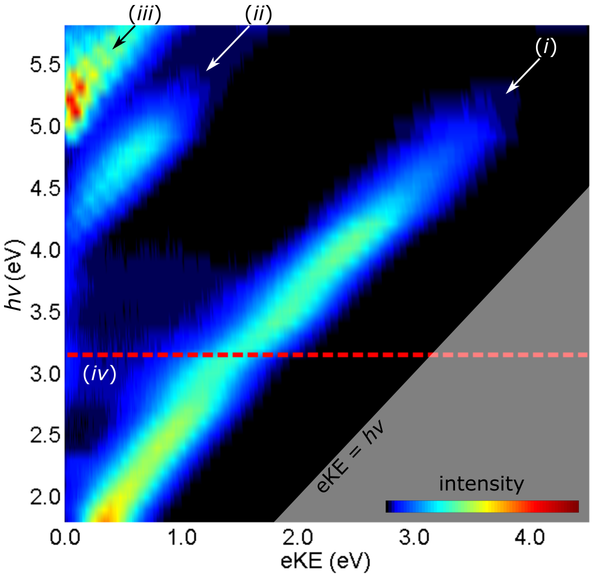

Figure 3.2: The frequency-resolved photoelectron spectra of $C_6F_6^-$ in the range $1.8 \leq h\nu \leq 5.8$ eV ($688.8 \geq \lambda \geq 213.8$ nm) at increments of 0.1 eV. The red dashed line indicates where the OPO switched from the visible to UV output ports. Feature (*i*) corresponds to the direct detachment process. Features (*ii*) and (*iii*) correspond to detachment of an electron that leaves the molecule in the neutral's triplet excited states T_1 and T_2 respectively. The low eKE electrons that comprise feature (*iv*) suggest that there are anion excited states accessible in this photon range that allow the molecule to capture some of the injected photon energy into nuclear motion before autodetaching the excess electron. The structure of this feature makes it hard to assign. There is no evidence for the existence of a CBS in these data.

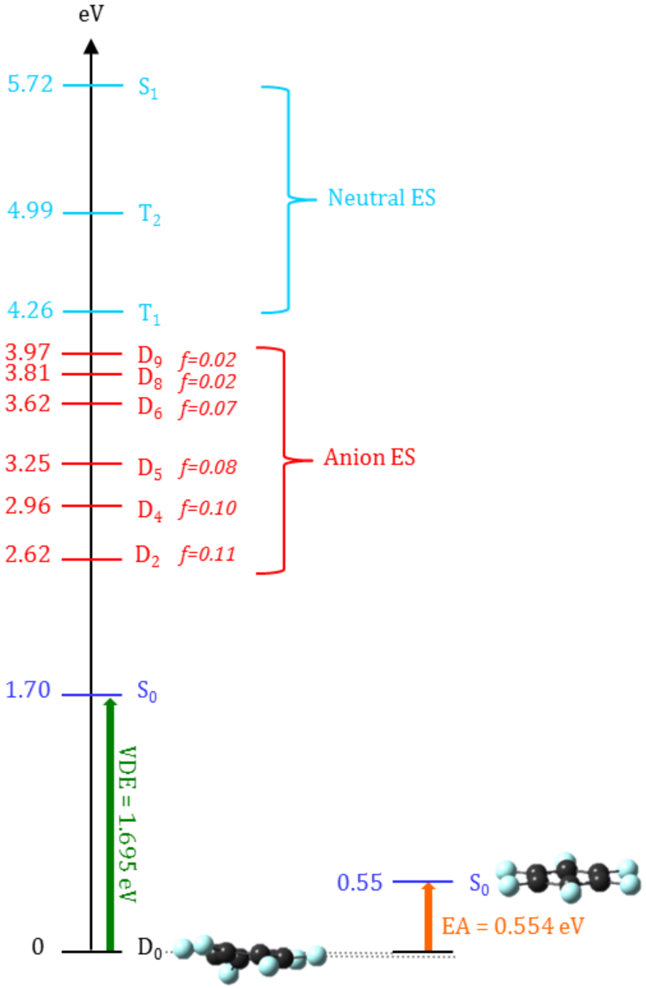

Figure 3.3: The electronic structure of C_6F_6 and its anion in the equilibrium geometry of the D_0 state. The S_0 state in its equilibrium geometry is shown on the right along with the calculated EA. The red D states are electronic excited states of the anion. Their respective oscillator strengths are shown alongside. The blue T states are the electronic excited state of the neutral, directly observed in Figure 3.2.

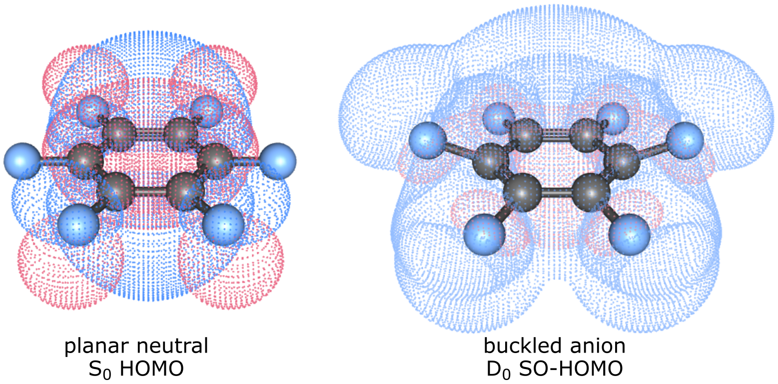

Figure 3.4: DFT calculations of the HOMO of the singlet S_0 ground electronic state of the planar neutral species and the SO-HOMO of the doublet D_0 ground electronic state of the buckled anion species.

3.4, show that the SO-HOMO is not significantly spherical or s-like, as would be expected from such a strongly anisotropic PAD. However, Dyson orbital calculations, which reveal the spatial character of the outgoing photoelectron waves, verified that the PAD should be strongly anisotropic with a correspondingly positive value for β_2.

There is a slight kink in the middle of feature (i) that has most likely arisen from improper management of high photoelectron signal levels. Rather than reducing the laser intensity or ion number density, the detector was turned down instead. It therefore follows that the density of photoelectrons produced in the interaction volume was high enough to perturb the VMI process. An alternative explanation is that the stepper motors controlling the crystals and prisms within the OPO required recalibration.

Features (ii) and (iii) correspond to detachment of an electron from an orbital below the anion's SO-HOMO, leaving a neutral molecule in a triplet excited state, as shown in Figure 3.5. TD-DFT calculations reveal that the first two triplet excited states of the neutral, T_1 and T_2, ought to appear at $h\nu$ = 4.26 and 4.99 eV respectively, in good agreement with the spectra in Figure 3.2. In contrast to feature (i), there is some vibrational structure evident in these peaks, as seen in Figure 3.1. This implies that the Franck-Condon overlap – and hence the geometric similarity – between the D_0 state and the T_1 and T_2 states includes the $v'' \sim 0 \leftarrow v = 0$ transition, unlike the direct detachment process seen in feature (i). This conclusion is corroborated by the TD-DFT calculation shown in Figure 3.6, which confirms that the geometry of the T_1 state is also buckled along a similar coordinate to the D_0 state.

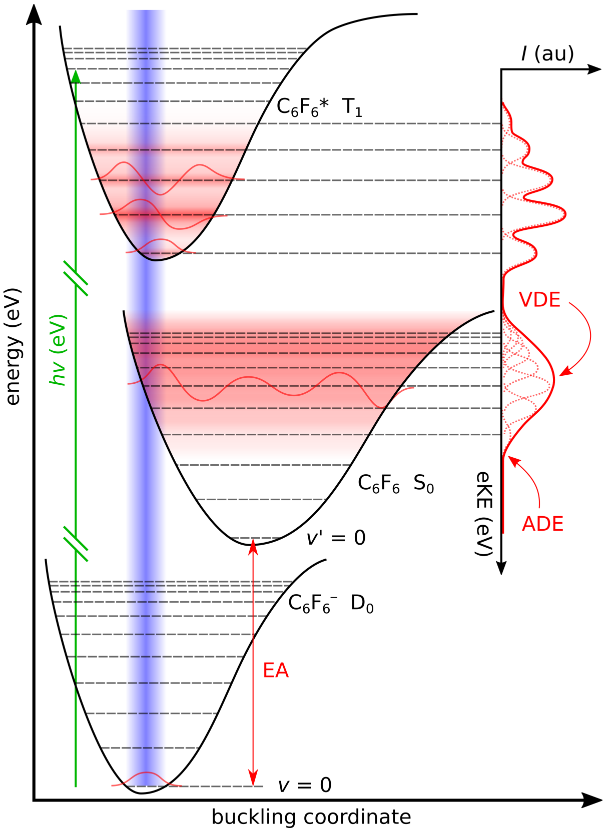

Figure 3.5: The shape of the features in Figure 3.2 can be explained by constructing a schematic similar to that in Figure 1.1. The reason the EA is not evident in Figure 3.2 is due to the lack of Franck-Condon overlap between the $v = 0$ vibrational level of the D$_0$ state and the $v' = 0$ level of the S$_0$ state. The projection of the $v = 0$ wavefunction (blue column) onto the S$_0$ state overlaps most favourably with closely-spaced vibrational levels far from its equilibrium geometry. The peaks that arise from these transitions are not resolvable and lead to a broad and Gaussian-shaped peak from which the VDE and ADE are derived. The lower vibrational levels of the T$_1$ state have a more favourable Franck-Condon overlap with the $v = 0$ level and therefore the corresponding feature contains some vibrational structure.

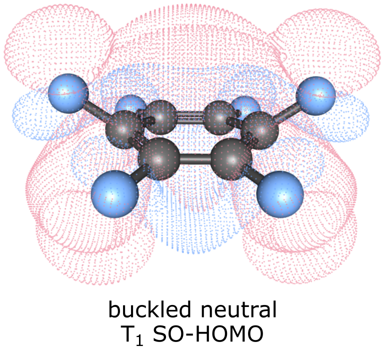

Figure 3.6: TD-DFT calculation of the SO-HOMO of the triplet excited electronic state of the neutral, T_1. The geometry adopted in this state is buckled in a similar manner to the D_0 state of the anion.

Finally, feature (*iv*) is characterised by the release of low eKE photoelectrons. In the case of features (*i*), (*ii*) and (*iii*), eKE increases at a rate commensurate with $h\nu$. The presence of these low eKE photoelectrons implies a mechanism by which photon energy is absorbed by the molecule before the electron departs. This in turn suggests the presence of electronic excited states of the anion that, when accessed, undergo a degree of nuclear rearrangement before autodetaching the excess electron. TD-DFT calculations reveal the presence of a series of anion excited states in the range $2.6 < h\nu < 4.0$ eV but the experimental data are not clear enough to make any confident assignments. However, one photon energy range containing a particularly pronounced increase of low eKE photoelectrons was explored in more detail.

Figure 3.7 shows the proportion of photoelectrons released with low eKE as a function of $h\nu$. The laser wavelength was scanned and the total pixel intensity of the central portion of the VMI heat map was measured as a proportion of the rest of the image. This peak is the clearest indication of the presence of some electronic excited state of $C_6F_6^-$ that undergoes autodetachment. However, the excitation energy does not convincingly match any of the electronic excited states identified in the DFT calculations. Furthermore, it was qualitatively observed during data acquisition that the prominence of this feature was not linearly dependent on the laser intensity. This non-linearity suggests that a multi- or multiple-photon process is responsible for the production of these low eKE photoelectrons. If this is the case, this feature may not be the result of autodetachment but rather it may correspond to a two-photon equivalent of feature (*ii*) that fortuitously appears when a $h\nu$ is resonant with an intermediate excited state. However, the exact mechanism remains unclear.

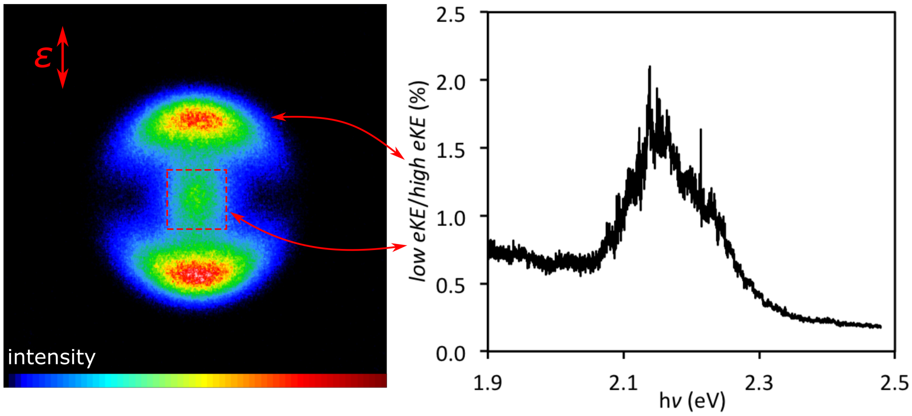

Figure 3.7: The proportion of photoelectrons released with low eKE as a function of incident photon energy. On the left is an example VMI heat map of $C_6F_6^-$ at $h\nu = 2.20$ eV. The laser polarisation is indicated by the arrow labelled ϵ. The total intensity of the central portion of the heat map, indicated by the red dashed box, constitutes the window in which photoelectrons were deemed *low eKE*. The rest of the photoelectron strikes on the heat map were counted as *high eKE*. The peak in the plot on the right confirms the probable presence of some resonant excited state of the anion that undergoes autodetachment or as an intermediate in a multiple-photon detachment process.

3.1.3 Conclusion

There is a distinct lack of any features in the frequency-resolved spectra in Figure 3.2 that would constitute a direct observation of a CBS. Given its predicted binding energy of 140 meV, photoelectrons detached from a CBS would have eKE = $h\nu$ – 140 meV. No such peaks are evident. This is likely due to the fact that the CBS is predicted to undergo a barrierless transition into the D_0 state. Therefore the entire anion population in the mass packet would be in the D_0 state after its long transit through the instrument.

Moreover, the C_6F_6 molecule is predicted to adopt the planar geometry when binding the excess electron in the CBS rather than the buckled geometry that characterises the D_0 state. This large geometry difference means that direct excitation from the D_0 state to the CBS is highly unlikely and would occur at a photon energy below the range probed in this experiment. Although the laser pulse duration, 5 ns, is more than sufficient for sequential multiple-photon processes to occur, indirect excitation to a CBS via one of the anion excited states implied by feature (*iv*) is not evident in the spectra.

Therefore, in order to observe a CBS, it must be generated in-situ by means of the low energy electron capture mechanism in which it is predicted to play a role. Previous studies have mimicked the electron impact process by deploying an in-cluster electron donor, using a charge-transfer mechanism that causes the excess electron to migrate from one species in a cluster to another within a specific energy range. In the first instance, clusters of $(C_6F_6)_n^-$ were employed as they were readily formed alongside $C_6F_6^-$ in the molecular beam.

3.1.4 Frequency-resolved PES of $(C_6F_6)_n^-$

The frequency-resolved photoelectron spectra of $(C_6F_6)_n^-$ clusters (n = 2 - 5) are shown in Figure 3.8. The primary features in each are similar to those in the $C_6F_6^-$ spectra. Each exhibit a direct detachment peak, similar to feature (*i*) in Figure 3.2. Similarly, each contain some photoelectron signal in the region where the T_1 and T_2 triplet excited states of the $n = 1$ cluster occur. There is also significant low eKE photoelectron signal in the region between these two prominent features.

However, there are a few key differences between these spectra and those in Figure 3.2. The VDE derived from the peak of the direct detachment feature increases incrementally by ~ 200 meV with the introduction of each additional

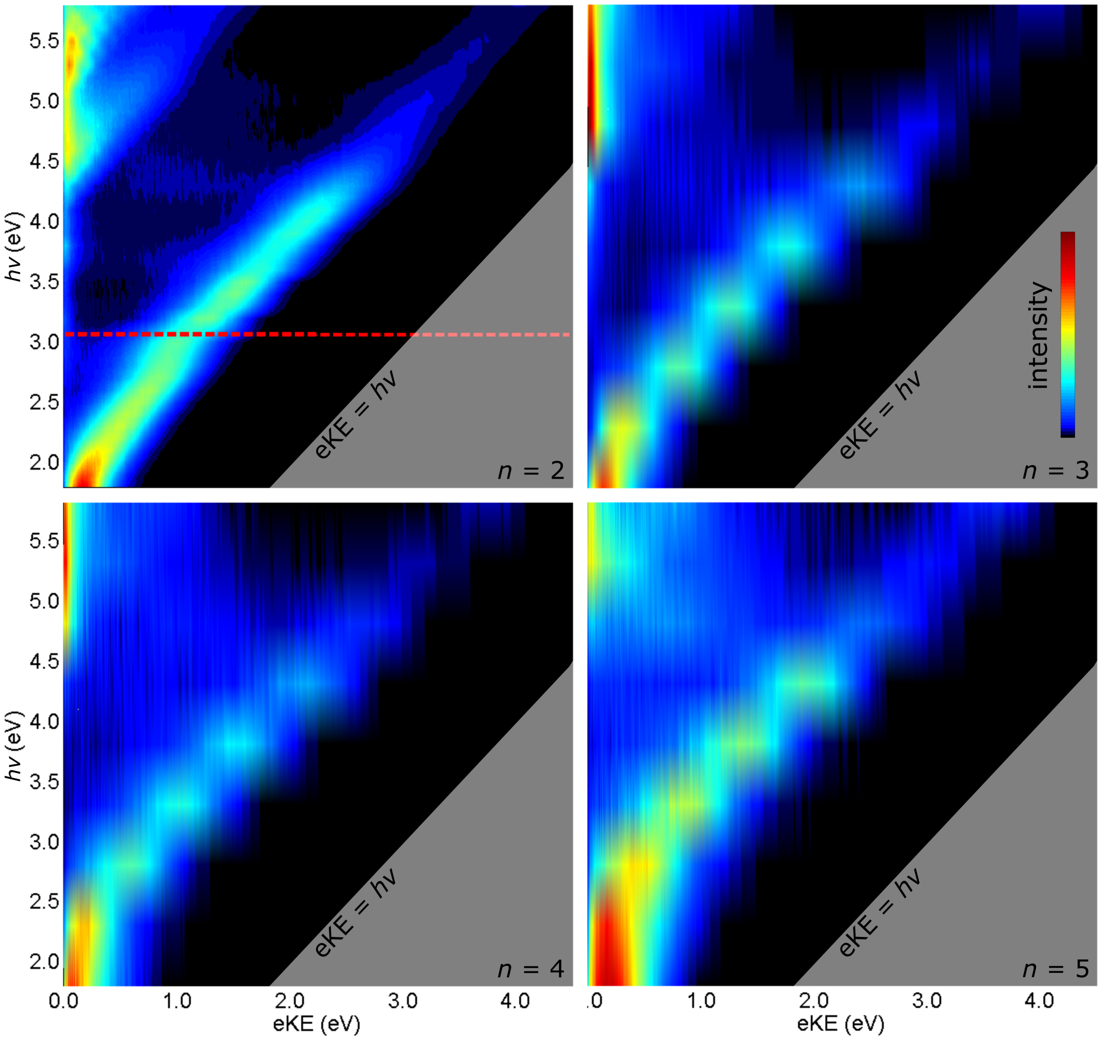

Figure 3.8: Frequency-resolved photoelectron spectra of $(C_6F_6)_n^-$ clusters for n = 2 - 5 in the range 1.8 ≤ $h\nu$ ≤ 5.8 eV (688.8 ≥ λ ≥ 213.8 nm). For the cluster n = 2, spectra were acquired at energy increments of 0.1 eV and for n = 3 - 5, increments of 0.5 eV. As in Figure 3.2, each photoelectron spectrum is normalised by its total photoelectron yield. The red dashed line indicates where the OPO switches from the visible to the UV output ports.

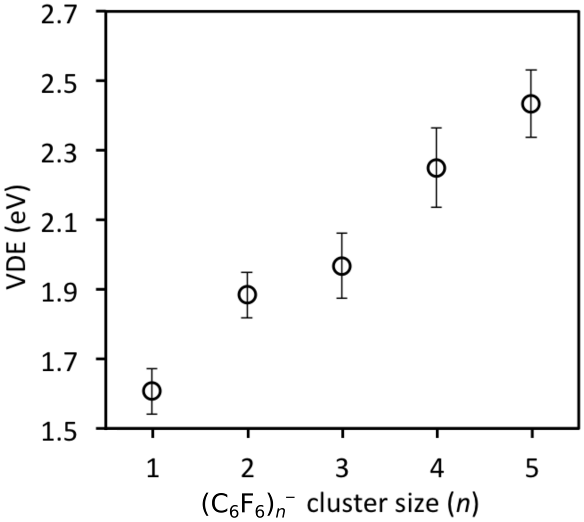

Figure 3.9: The VDE of the $(C_6F_6)_n^-$ clusters. The VDE increases in a linear fashion at a rate of ~ 200 meV per additional n.

cluster unit, as shown in Figure 3.9. This is explained by the cluster cohesion energy, described in Figure 3.10. When n is small, the attractive potential between a $(C_6F_6)_n^-$ anionic cluster and an additional C_6F_6 molecule is deeper by ~ 200 meV than the equivalent of a neutral $(C_6F_6)_n$ cluster. Additionally, the adjacent molecules in the cluster may form a solvation shell around the anion, hindering the departure of the photoelectron, which would increase the measured VDE. However, this hindrance effect must be a small as the expected broadening of the direct detachment peak is not evident.

The other key change in the spectra to note is that the vibrational structure that was apparent in the features assigned to the T_1 and T_2 triplet excited states in Figure 3.2 is no longer resolvable. This is attributed to the presence of adjacent molecules in the cluster hindering free vibrational movement and hence blurring out previously well-defined spectral features.

3.1.5 Conclusion

It was thought that by clustering a shell of neutral planar C_6F_6 molecules around a slow electron donor, in this case $C_6F_6^-$, a CBS could be generated within the VMI interaction volume and immediately probed. However, these spectra do not contain any peaks with eKE ~ $h\nu$ that would indicate that a CBS had been formed and probed. Nor do they contain any clearly resolvable electronic excited

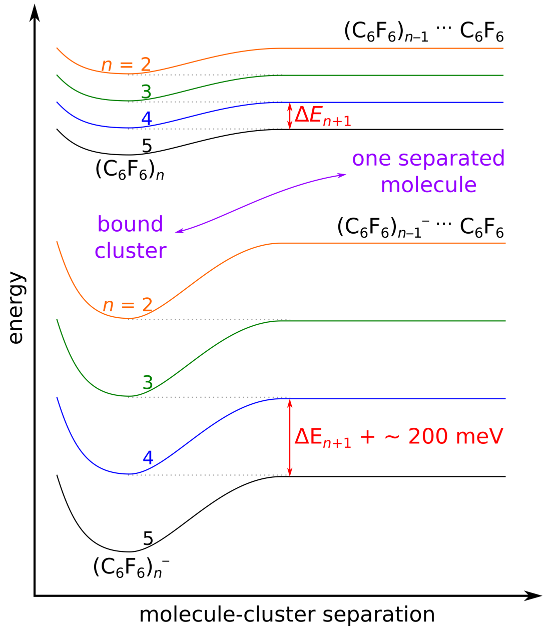

Figure 3.10: The increase in VDE with each additional cluster unit can be explained by considering the cluster cohesion energy. The attractive potential between a C_6F_6 molecule and a $(C_6F_6)_n$ neutral cluster has some depth, ΔE_{n+1}. This interaction is governed by van der Waals forces. The attractive potential between a C_6F_6 molecule and a $(C_6F_6)_n^-$ anionic cluster is deeper by ~ 200 meV when n is small. The attraction is stronger than in the case of the neutral cluster because of the influence of charge:induced-dipole interactions. Therefore, the VDE measured in the photoelectron spectra increase by ~ 200 meV per additional cluster unit.

states of the anion that might evolve into to a CBS. Therefore, an alternative approach is required in order to ensure a successful transfer of the charge from the donor species to the C_6F_6 molecule.

3.2 Frequency and time-resolved PES of $C_6F_6 \cdot I^-$ clusters

The following is based on a paper accepted for publication in the journal Nature Chemistry.

3.2.1 Motivation

Although a CBS could not be generated in $(C_6F_6)_n^-$ clusters, I^- has been demonstrated to be an effective intra-cluster electron donor[1,33,107,115–133]. In these studies, the electron proceeds via a CTS, which has in some cases been shown to be a non-valence binding mode of the excess electron. Given that the CBS of $C_6F_6^-$ is predicted to be a doorway state for low energy electron capture, a CTS of the $C_6F_6 \cdot I^-$ cluster is a good candidate for observing a CBS. Cate's initial calculations on the $C_6F_6 \cdot I^-$ cluster indicates that the I^- sits above the C_6F_6 molecule's ring structure and that geometry of the C_6F_6 molecule is negligibly affected by the presence of the I^- ion. This result gives credence to the idea that this particular intra-cluster charge-transfer process may suitably mimic the capture of a free electron by a neutral planar C_6F_6 molecule to form $C_6F_6^-$.

In order to first demonstrate the possible existence of such a CTS, frequency-resolved photoelectron spectra of $C_6F_6 \cdot I^-$ clusters were measured. Given that there are no bound electronic excited states of atomic I^-, any occurrence of an electronic excited state in the $C_6F_6 \cdot I^-$ cluster indicates the likely presence of a CTS. Once identified and located, time-resolved PES was deployed to probe its dynamics.

3.2.2 Methodology

In the frequency-resolved experiment, $h\nu$ was varied using the nanosecond OPO laser system described in Appendix A.2.1. Photon energies in the range $3.1 \leq h\nu \leq 5.8$ eV ($399.9 \geq \lambda \geq 213.8$ nm) were used at increments of 0.1 eV. It is important to reiterate that the pulse duration of ~ 5 ns is very long compared to the timescale of electronic and nuclear dynamics within the $C_6F_6 \cdot I^-$ clusters and therefore gives adequate opportunity for sequential multiple-photon processes to occur. The data were acquired and analysed using the LabVIEW software described in Appendix A.3.1.

In the photoelectron flux experiment, $h\nu$ was scanned continuously using the nanosecond OPO laser system described in Appendix A.2.1. Using the software described in Appendix A.3.3, the total pixel intensity of each frame was recorded as an approximate measure of the number of photoelectrons produced. Normalisation to account for variations in laser intensity was achieved by dividing the spectrum by the wavelength-dependent photoelectron flux of I^-. This normalisation is only as valid as the assumption that the cross section of I^- is independent of photon energy within the range of the scan[153].

In the time-resolved experiment, two femtosecond laser pulses with a variable time delay addressed the clusters, as described in Appendix A.2.2. The 3.10 eV (400 nm) pump pulse first excites the species into an electronic excited state, in this case the CTS of $C_6F_6 \cdot I^-$ identified in the frequency-resolved spectrum. The $h\nu = 1.55$ eV (800 nm) probe pulse then interrogates the evolution of the electron within the system. The two pulses have a temporal cross-correlation of 70 fs and a series of scans, both forward and backward in t, were performed using the LabVIEW software described in Appendix A.3.2.

3.2.3 Frequency-resolved PES of $C_6F_6 \cdot I^-$

The frequency-resolved photoelectron spectra of $C_6F_6 \cdot I^-$ are shown in Figure 3.11. Features (*i*) and (*ii*) consist of peaks with eKE that increases linearly with $h\nu$. These peaks are very narrow, which implies that the equilibrium cluster geometry is not significantly affected by the photodetachment of the excess electron. Photoelectron spectra[154] of atomic I^- consist of two peaks with eBE = 3.059 eV and 4.002 eV, split by 0.943 eV. Features (*i*) and (*ii*) are separated by 0.93 ± 0.01 eV and feature (*i*) has VDE = 3.49 eV. Given that the energy splitting is the same, albeit with a marginally higher direct detachment energy than atomic I^-, features (*i*) and (*ii*) can confidently be assigned to direct detachment of the excess electron from $C_6F_6 \cdot I^-$, leaving neutral clusters of $C_6F_6 \cdot I\ [^2P_{3/2}]$ and $C_6F_6 \cdot I\ [^2P_{1/2}]$ respectively.

The above assignment is confirmed by the PAD of these features, which has negative anisotropy in both cases ($\beta_2 = -\ 0.75$). The negative β_2 values imply that the orbital from which the electron was removed is p- or π-like. Indeed, Cate's DFT calculations show that the π ring system of the C_6F_6 molecule mixes a good deal with the p-orbitals on the clustered I atom. These features therefore confirm that the excess electron is localised to the I 5p orbital within the cluster in its equilibrium state, as would be expected from the relatively high EA of I (3.059 eV) compared to C_6F_6 (0.55 eV). The difference between the VDE of $C_6F_6 \cdot I^-$ and the EA of I is 0.43 eV, which corresponds to the increase in cluster cohesion energy of $C_6F_6 \cdot I^-$ relative to $C_6F_6 \cdot I$, depicted in Figure 3.12.

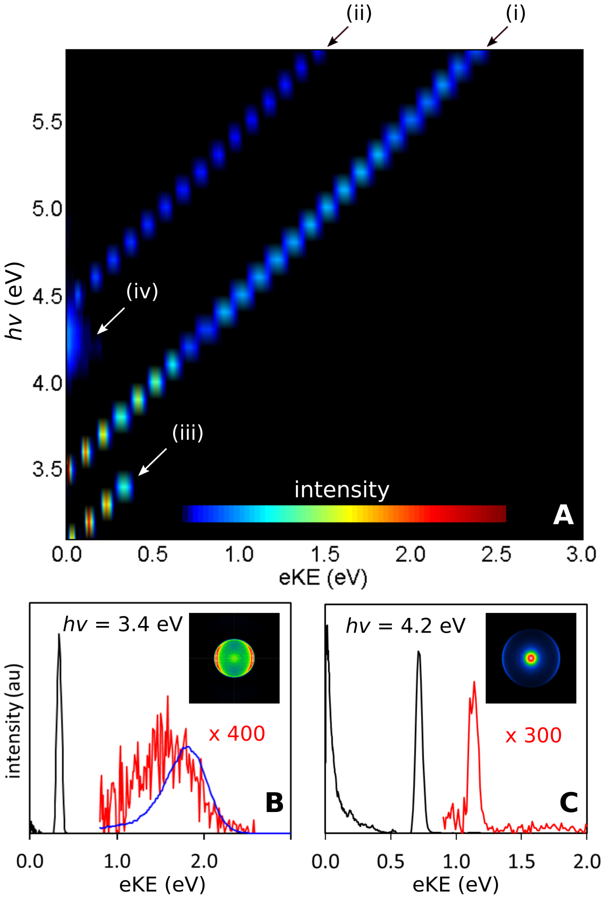

Figure 3.11: A – the frequency-resolved photoelectron spectra of $C_6F_6 \cdot I^-$ in the range $3.1 \leq h\nu \leq 5.8$ eV ($399.9 \geq \lambda \geq 213.8$ nm). The intensities are normalised by the total photoelectron yield in each spectrum. Features (*i*) and (*ii*) correspond to direct detachment of the excess electron from the I^- ion, leaving neutral I in its $^2P_{3/2}$ and $^2P_{1/2}$ states respectively. Feature (*iii*) is consistent with photodetachment of the electron from atomic I^-, independent of the cluster environment. Feature (*iv*) corresponds to delayed autodetachment from an excited state at around 4.2 eV.
B & C – the photoelectron spectrum at $h\nu = 3.4$ and 4.2 eV along with their respective VMI heat maps inset. In order to aid comparison, the photoelectron signal above eKE = 1.0 eV (red) is scaled and the photoelectron spectrum of $C_6F_6^-$ (blue) is overlaid in B.

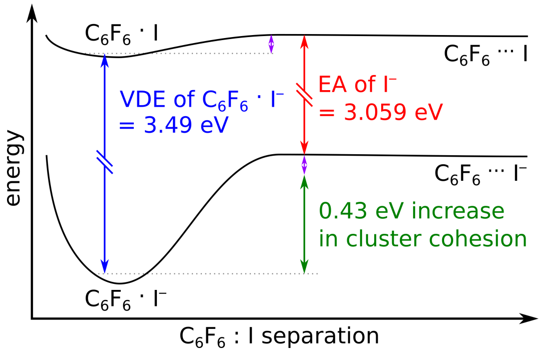

Figure 3.12: The cluster cohesion energy of $C_6F_6 \cdot I^-$ is greater than that of $C_6F_6 \cdot I$ by 0.43 eV. This is evident in the fact that the VDE of $C_6F_6 \cdot I^-$ is greater than the EA of I by 0.43 eV. The absolute cluster cohesion of both the neutral and anionic clusters are unknown.

This increase in cluster cohesion energy arises from the charge:induced-dipole interactions between the I^- and C_6F_6 molecule that are absent in the case of the neutral cluster, which is bound only by weaker van der Waals forces.

Feature (*iii*) consists of a peak that matches the aforementioned spectra of atomic I^-. Given that this peak appears below the threshold for single-photon direct detachment (indicated by feature (*i*)), and that the laser pulse is of sufficient duration to induce multiple-photon processes, the presence of feature (*iii*) implies the existence of some mechanism that leads to cluster dissociation and the generation of I^- as a photofragmentation product.

The magnified peak shown in red in Figure 3.11 B is compared to the photoelectron peak for $C_6F_6^-$ at the same photon energy, overlaid in blue. While the profile is similar, the eKE is shifted to slightly lower energy, suggesting that this peak corresponds to direct detachment of the excess electron from a $C_6F_6^- \cdot I$ cluster where the charge is localised to the C_6F_6 molecule and is stabilised somewhat by the presence of the 'solvent' I atom.

In studies of the uracil·I^- cluster[1], photoexcitation at $h\nu = 4.0$ eV resulted in the production of both I^- and [uracil·H]$^-$ photofragments. The emergence of the I^- fragment had a rise-time of 86 ± 7 ps, much faster than the 5 ns duration of the laser pulse in this frequency-resolved experiment. It was concluded that the mechanism by which this took place involved the initial excitation of the excess electron from the I^- to a DBS of the uracil anion. This then, through a process of internal conversion, decayed back into a vibrationally excited uracil·I^-

cluster that subsequently dissociated. This interpretation can be translated to the $C_6F_6 \cdot I^-$ cluster and is summarised by,

$$C_6F_6 \cdot I^- \xrightarrow{h\nu} [C_6F_6 \cdot I[^2P_{3/2}]]^{*-} \xrightarrow[\text{charge-transfer}]{\text{dissociation } \textit{or}} I^- + C_6F_6 \textit{ or } C_6F_6^- \cdot I[^2P_{3/2}], \quad (3.1)$$

where $[C_6F_6 \cdot I[^2P_{3/2}]]^{*-}$ is some electronic excited state of the cluster in which the I atom is in its $[^2P_{3/2}]$ state. This mechanism explains the generation of the two products that are indicated by the presence of feature (*iii*) and the magnified peak in Figure 3.11 B. Given that this excited state leads to the production of $C_6F_6^- \cdot I$ as well as I^-, it follows that it functions as a CTS.

Feature (*iv*) in Figure 3.11 is characterised by low eKE photoelectrons at around $h\nu = 4.2$ eV. As can be seen in the magnified peak in Figure 3.11 C, I^- persists as a product of photofragmentation, suggesting it is in competition with the mechanism that produces feature (*iv*) and that therefore their respective lifetimes are comparable.

The position of feature (*iv*) relative to feature (*ii*) is comparable to the position of feature (*iii*) relative to feature (*i*). The most likely explanation for this feature is the presence of another excited state of the cluster in which the I atom is in its $[^2P_{1/2}]$ state. This second excited state either decays back into $C_6F_6 \cdot I^-$ and then dissociates, as seen in feature (*iii*), or undergoes delayed autodetachent of the excess electron. Unlike the excited state assigned to feature (*iii*), autodetachment is a pathway open at this photon energy because it is above the threshold for direct detachment. However, in order to do so, the I atom must undergo spin-orbit relaxation into its $[^2P_{3/2}]$ state, which may explain why the rate of cluster dissociation is comparable. This mechanism can be summarised by,

$$C_6F_6 \cdot I^- \xrightarrow{h\nu} [C_6F_6 \cdot I[^2P_{1/2}]]^{\dagger -} \xrightarrow[\text{autodetachment}]{\text{dissociation } \textit{or}} I^- + C_6F_6 \textit{ or } C_6F_6 \cdot I[^2P_{3/2}] + e^-, \quad (3.2)$$

where $[C_6F_6 \cdot I[^2P_{1/2}]]^{\dagger -}$ is this second excited state of the cluster that proceeds via the $[^2P_{1/2}]$ state of I and can then undergo spin-orbit relaxation and delayed autodetachment of the excess electron to form $C_6F_6 \cdot I[^2P_{3/2}]$.

3.2.4 Photoelectron flux spectroscopy of $C_6F_6 \cdot I^-$

Figure 3.13 shows the photoelectron flux of $C_6F_6 \cdot I^-$ as a function of photon energy. The features are labelled in accordance with their counterparts in Figure 3.11. The VDE of the $C_6F_6 \cdot I^-$ cluster can be seen clearly in feature (*i*) where the total photoelectron flux suddenly increases.

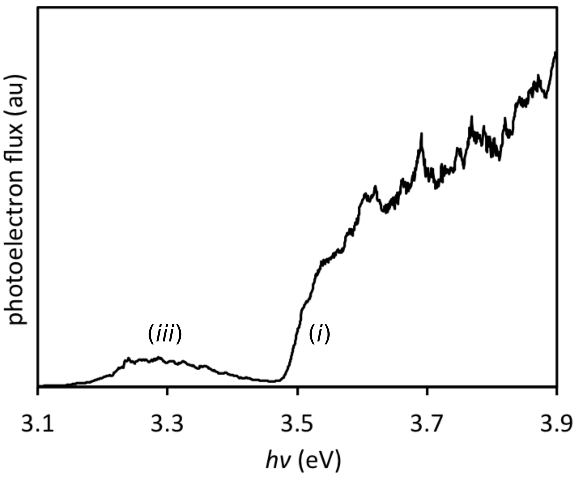

Figure 3.13: The photoelectron flux of $C_6F_6 \cdot I^-$ as a function of incident photon energy. There is a small band of measurable photoelectron yield (*iii*) below the threshold of direct detachment from the I^- ion within the cluster (*i*). This band corresponds to feature (*iii*) in Figure 3.11, which implies the presence of an electronic excited state that leads to cluster dissociation and the subsequent detection of the I^- photofragment.

Feature (*iii*) corresponds to direct detachment from the I^- photofragment described in Equation 3.1. The photoelectron flux for this feature is low compared to feature (*i*) due to the fact that it requires two sequential photons to release the photoelectron; one to induce the photofragmentation of the $C_6F_6 \cdot I^-$ cluster and one to photodetach the excess electron from the I^- product. The PAD of this feature is negative ($\beta_2 = -0.75$), in concordance with photoelectron spectrum of I^-. The band in feature (*iii*) therefore indicates where excitation into the CTS of the cluster can be accessed and therefore where the pump photon of the time-resolved regime ought to be tuned.

However, the photoelectron flux is particularly small at the low $h\nu$ side of feature (*iii*). At this point, the photon energy is just above threshold for photodetachment from I^- and so the assumption of its uniform cross section, which underlies the normalisation process, breaks down. Furthermore, the OPO laser intensity is particularly low in this region and given that the photoelectron flux of multiple-photon process does not scale linearly with laser intensity, the photoelectron flux measured will be lower than the single-photon driven population transfer into the CTS. Indeed, the charge-transfer band may extend to lower photon energies. However, the question remains whether this CTS possesses the characteristics of a CBS.

Table 3.1: The spectral windows in which the principle features of the time-resolved photoelectron spectra occur. These windows are indicated by the correspondingly coloured square brackets in Figure 3.14. The spectra are integrated within these windows in order to determine their respective time-dependencies. This is shown in Figure 3.15.

Data	**Spectral window**	
colour	**eKE min** (eV)	**eKE max** (eV)
grey	0.0	0.1
red	0.25	0.60
blue	1.0	1.2

3.2.5 Time-resolved PES of $C_6F_6 \cdot I^-$

Having located the CTS accessible in the band $3.1 \leq h\nu \leq 3.5$ eV, time-resolved femtosecond pump-probe PES was deployed to measure its dynamics and determine whether it exhibits the characteristics of a CBS.

The time-resolved photoelectron spectra of $C_6F_6 \cdot I^-$ are shown in Figure 3.15. A pump pulse of 3.10 eV was selected. Although this corresponds to the tail end of the charge-transfer band revealed in Figure 3.13, it should still be resonant with the CTS for two reasons. Firstly, as discussed above, the intensity of the low $h\nu$ side of the band was likely underestimated; and secondly, the laser system is able to produce a reasonably high intensity 3.10 eV pulse. Therefore, because of its finite spectral width, the 3.10 eV pump pulse should generate as much population in the CTS as a lower intensity pump pulse tuned to the band's apparent peak at 3.30 eV.

For both the 3.10 eV pump and 1.55 eV probe photons, $h\nu <$ VDE. This experiment therefore has the benefit that any and all photoelectron signal observed arises from multi- or multiple- photon processes.

Subplot A in Figure 3.14 contains three primary features that occur within the spectral windows detailed in Table 3.1: two intense and short-lived peaks centred around eKE $=$ 0.2 and 1.1 eV (blue); bands of photoelectron signal in the range $0.25 <$ eKE < 0.60 eV that oscillate with time (red); and a feature at eKE < 0.1 eV that increases in prominence with increasing time-delay (grey).

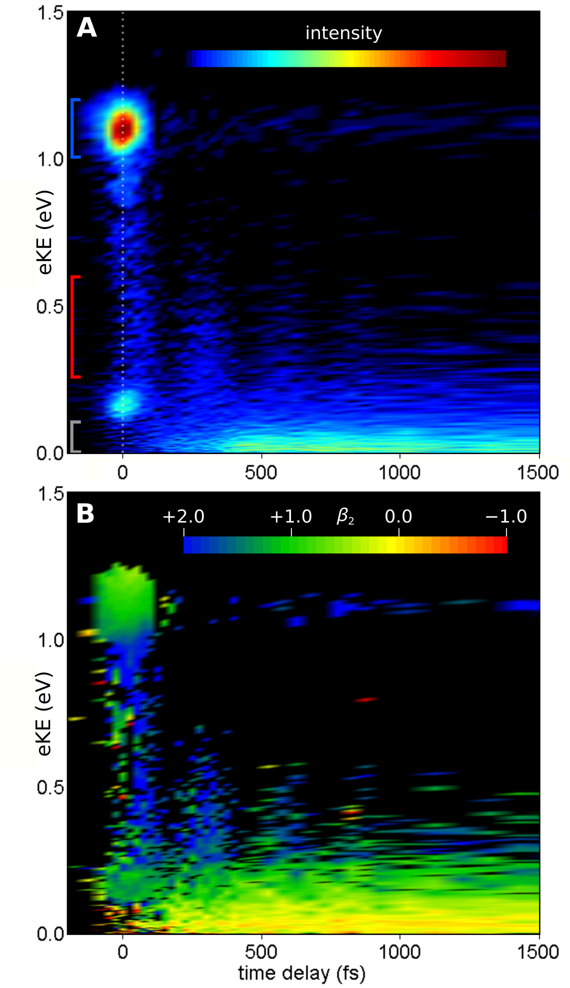

Figure 3.14: The time-resolved photoelectron spectra of $C_6F_6 \cdot I^-$ and corresponding PAD false-colour plots. Each vertical slice in subplot A is an individual photoelectron spectrum, normalised by integrating its intensity profile and then multiplying it by the photoelectron flux at the corresponding time delay. The features in the spectral windows indicated by the coloured brackets have been integrated and plotted as a function of time in Figure 3.15. Details of the spectral windows are outlined in Table 3.1. The PAD is shown in subplot B. Data are only presented where signal levels were above 5% of the maximum intensity in subplot A. A moving average of ±4 data points was applied uniformly to each spectrum in order to gently smooth particularly noisy regions.

The high-intensity, short-lived features in the spectral windows $0.1 \leq$ eKE ≤ 0.2 eV and $1.0 \leq$ eKE ≤ 1.2 eV are centred around $t = 0$ (t_0), where the pump and probe pulses overlap temporally. The energy separation between these two prominent peaks is 0.93 ± 0.02 eV. As in the frequency-resolved spectra in Figure 3.11, this corresponds to the spin-orbit splitting in atomic I that gives rise to the energy separation between the $^2P_{3/2}$ and $^2P_{1/2}$ states. Indeed the sum of the pump and probe photon energies is 4.65 eV and the corresponding frequency-resolved one-colour photoelectron spectrum in Figure 3.11 contains peaks at the same eKE. This feature can therefore confidently be assigned to 3.10 eV pump-photon excitation of the excess electron from the 5p orbital of the I atom to the CTS identified in the frequency-resolved measurements of the cluster, from where it is photodetached by the 1.55 eV probe photon.

Although these peaks at t_0 may have the same eKE profile as the frequency-resolved spectrum at 4.65 eV, there is a difference in the PAD between these peaks and the corresponding peaks in features (*i*) and (*ii*) of Figure 3.11. In the one-colour frequency-resolved spectra, $\beta_2 = -0.7$ for these peaks, whereas in the two-photon time-resolved pump-probe spectra, $\beta_2 = +1.0$, as shown in subplot B of Figure 3.14. This suggests that the orbital from which the excess electron was removed at t_0 is s-like. Indeed TD-DFT calculations performed using the CAM-B3LYP functional and aug-cc-pVDZ Dunning basis set indicate the existence of a probable CTS at an appropriate excitation energy characterised by a large, predominantly spherical orbital that surrounds the C_6F_6 molecule in its planar geometry. This is the first piece of evidence indicating that the orbital characterising the CTS expresses characteristics similar to the CBS predicted by Voora and Jordan[97].

The time-dependence of the peaks in this feature is shown in blue in Figure 3.15. To derive each point, the photoelectron spectrum at each time-step was integrated within the spectral window specified in Table 3.1. Given that the lineshape of the temporal profile is very Gaussian, all that can be understood from this is that the lifetime of this CTS is less than the time-resolution of the experiment, < 40 fs, as determined by the cross correlation of the two laser pulses. The mechanism that gives rise to this feature is therefore summarised by,

$$C_6F_6 \cdot I^- \xrightarrow[pump]{h\nu=3.10\text{ eV}} [C_6F_6 \cdot I]^{*-} \xrightarrow[probe]{h\nu=1.55\text{ eV}} C_6F_6 \cdot I[^2P_{3/2}] \textit{ or } [^2P_{1/2}] + e^-, \quad (3.3)$$

where the two photons arrive simultaneously and $[C_6F_6 \cdot I]^{*-}$ is the CTS of the cluster identified in feature (*iii*) of Figures 3.11 and 3.13. The peak at eKE = 1.1 eV corresponds to photoelectrons leaving a neutral cluster in which the I atom is in its $[^2P_{3/2}]$ state whereas the peak at 0.2 eV indicates that the I atom may also be left in its $[^2P_{1/2}]$ state. The relative intensity of the low eKE peak compared to the high eKE peak is much smaller than is observed[153] in

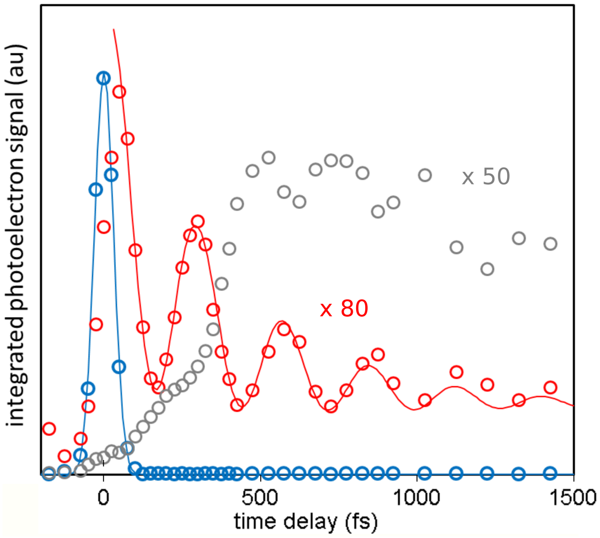

Figure 3.15: The time-dependence of the features indicated by the coloured brackets in Figure 3.14. Each data point is the integral of the photoelectron spectrum within the spectral windows specified in Table 3.1 at its respective time delay, t. The blue data (circles) have been fitted to a Gaussian function (line) and the red data have been fitted (after $t = 0$) to a function expressed in Equation 3.4. The red data have been multiplied by 80 × and the grey data by 50 × in order to ease comparison with the more intense blue data.

one-colour PES of I^-. This is because in the two-photon pump-probe regime, the CTS serves as a resonant intermediate in producing the high eKE peak whereas no such resonant intermediate is accessible to enhance the production of photoelectrons for the low eKE peak.

In addition to the short-lived high intensity peak at eKE $= 1.1$ eV, there is a strip of photoelectron signal that endures within the blue spectral window. This is background noise that arises from tripling the 1.55 eV probe photon to produce $h\nu = 4.65$ eV at all time-delays. This background noise was not subtracted although its intensity was minimised by reducing the power of the probe pulses in the VMI interaction volume.

The intensity of the peak centred around eKE $= 1.1$ eV is high compared to the rest of the spectrum, which indicates a comparatively large photodetachment cross section for that particular mechanism. It has been shown that the cross section for photodetachment of an electron is expected to be large when the de Broglie wavelength of the outgoing photoelectron is similar to the spatial extent of the orbital from which it comes[128,155,156]. At 1.1 eV, the de Broglie wavelength, $\lambda = \frac{h}{p}$, of the photoelectron is ~ 12 Å. According to the calculations by Voora and Jordan, the radius at which the proportion of the total integrated intensity of the wavefunction describing the CBS of $C_6F_6^-$ reaches 90 % is ~ 11 Å. Given the high intensity of this peak and the conformity between the de Broglie wavelength of the photoelectron and the size of the predicted CBS, further similarities are revealed between the predicted CBS and the CTS accessed by the pump photon and probed at t_0.

The oscillating feature in the spectral window $0.25 < \mathrm{eKE} < 0.60$ eV (red in Figure 3.15) has been fitted to a damped oscillator with a decaying offset described by,

$$I(t) = A\mathrm{e}^{-\frac{t}{\tau_1}} \cos(\omega t + \phi) + B\mathrm{e}^{-\frac{t}{\tau_2}} + C, \tag{3.4}$$

where A, B and C are arbitrary; τ_1 is the dampening lifetime; τ_2 is the lifetime of the decaying offset; ϕ is the phase shift from t_0; and ω is the frequency of the oscillations. The fitting yielded values of $\omega = 121 \pm 2$ cm^{-1} and $\phi = -0.6$ rad. These correspond to an oscillation period of 275 ± 5 fs and phase offset of 26 fs.

A fast Fourier transform (FFT) of the data, shown in Figure 3.16, contains a peak at 121 cm^{-1} with a Lorentzian-like lineshape, confirming both the principle frequency and decaying character of the oscillations. These oscillations in photoelectron signal are reminiscent of wavepacket dynamics observed in the time-resolved spectra of molecules undergoing coherent vibrational motion[157].

It should be noted that the first band of intense photoelectron signal after t_0 in the range $0.25 \leq \mathrm{eKE} \leq 1.0$ eV has a subtle time-dependency. The eKE decreases rapidly with increasing time-delay, t, and the photoelectron signal intensity simultaneously reduces significantly. This indicates that the electron undergoes a rapid increase in eBE and suggests that the cross section of its orbital rapidly decreases at the same time. This rapid reduction in the photodetachment cross section and simultaneous increase in eBE may explain how the $C_6F_6^- \cdot I$ clusters seen in Figure 3.11 are generated. In order to produce the $C_6F_6^- \cdot I$ cluster with the anion in its D_0 state, the electron must transfer from the diffuse and short-lived CTS into the smaller and more tightly-bound VBS.

Indeed, Voora and Jordan's calculations predict that the CBS with eBE = 0.14 eV undergoes a barrierless transition into the VBS with VDE = 1.60 eV. In so doing, the orbital's 90 % isosurface moves from a radius of ~ 11 Å to a radius of < 4 Å. The photoelectrons produced by the probe photon before and after this transition have a de Broglie wavelength of ~ 12 Å and ~ 40 Å respectively. This change in orbital size would result in the sudden drop in photodetachment cross section, which is in fact what is seen in this feature in the spectral window $0.25 \leq \mathrm{eKE} \leq 1.0$ eV.

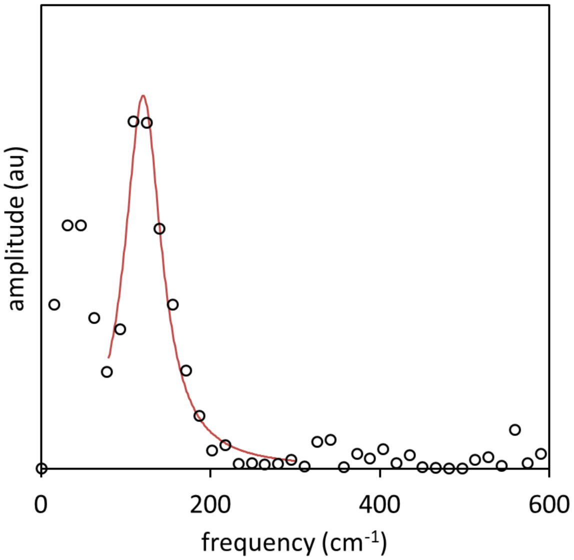

Figure 3.16: The FFT of the oscillating feature shown in Figure 3.15. The red line is a Lorentzian fit to the data and is centred at 121 ± 2 cm^{-1}, in accord with the model in Equation 3.4.

Furthermore, when the PAD of this feature is examined in subplot B of Figure 3.14, there is a clear difference between it and the primary intense peak in the spectral window 1.0 ≤ eKE ≤ 1.2 eV. The β_2 coefficient increases from $+$ 1.0 to $+$ 2.0, indicating a rapid change in the electronic character of the orbital from which the excess electron is removed. Whereas the β_2 = +1.0 anisotropy of the primary peak is consistent with detachment of the excess electron from a spherical s-like orbital, the β_2 = +2.0 anisotropy of the proceeding feature (and that of the continuing oscillations) is consistent with the PAD measured for $C_6F_6^-$, in which the excess electron leaves the valence-bound D_0 state of the molecule in a distinct p-wave. This change in PAD strongly suggests that the CTS observed in the primary peak is electronically distinct from the state that follows and therefore lends further credence to its assignment as a CBS.

As the excess electron enters the valence system of the C_6F_6, the molecule's geometry is expected to change from planar to buckled because the equilibrium geometry of the D_0 state of the anion is different to that of the S_0 state of the neutral, as confirmed by the DFT calculations presented in Figure 3.3. Further TD-DFT calculations were performed in order to assign the oscillations measured in the photoelectron signal shown in Figure 3.15; the frequency of the first 6 of 19 calculated vibrational modes of $C_6F_6^-$ are presented in Table 3.2. Mode number 3, 122 cm^{-1}, appears to be the best match for the measured frequency of 121 ± 2 cm^{-1}. The vectors of this vibrational mode are overlaid on the buckled $C_6F_6^-$ molecule depicted in Figure 3.17, and show that the motion of the nuclei is

Table 3.2: The frequencies of the first 6 vibrational modes of $C_6F_6^-$, calculated by TD-DFT. Mode number 3 is closest to 121 ± 2 cm^{-1}, the frequency of the oscillations in photoelectron signal measured in Figure 3.15. The vectors indicating the nuclear motion in this vibrational mode are shown in Figure 3.17.

Mode number	**Frequency** / cm^{-1}
1	69.55
2	104.22
3	122.23
4	187.60
5	255.75
6	259.34

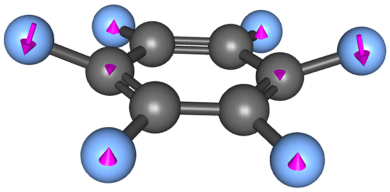

Figure 3.17: The bending mode of $C_6F_6^-$ that lies along the nuclear coordinate between the buckled geometry of the D_0 state and the planar geometry adopted in the CBS. The pink arrows indicate the direction and magnitude of the motion of the nuclei. The calculated frequency of this mode is 122 cm^{-1}, which is in strong agreement with the frequency of 121 ± 2 cm^{-1} measured in the oscillations in photoelectron signal seen in Figure 3.15.

directed along the coordinate between the buckled and planar geometries of the molecule. None of the other vibrational modes of the molecule that were calculated exhibit nuclear motion along this coordinate. These vectors, along with the close agreement between the measured and calculated frequencies, support the conclusion that the oscillations observed in Figure 3.15 do indeed correspond to the change in geometry expected as the molecule buckles from its planar S_0 geometry into its D_0 equilibrium geometry.

The oscillations in photoelectron signal arise from the fact that as the $C_6F_6^-$ buckles, eBE increases until it is more than the energy that the probe photon can provide. This steep rise in eBE is the result of the sudden divergence of the D_0 potential energy surface with respect to that of the S_0 as the ion buckles into its new equilibrium geometry.

Due to the rapid change in geometry, the molecule actually over-buckles beyond the equilibrium geometry of the anion and the photoelectron signal disappears altogether. The minima in the oscillations in Figure 3.15 correspond to this outer turning point. The molecule then returns along the bending coordinate towards its original planar configuration, at which point the photoelectron signal returns because the potential energy surface of the neutral becomes accessible again. The maxima in the oscillations in Figure 3.15 correspond to this inner turning point. The dampening of the oscillations and slight dephasing at $t > 750$ fs is likely the result of the oscillations coupling to other bending modes of the molecule along different coordinates at divergent frequencies, known as intramolecular vibrational energy redistribution[158].

The first oscillation in Figure 3.15 indicates that the equilibrium geometry of the $C_6F_6^-$ ion is first reached at $t \sim 100$ fs. Given that a full oscillation period is 275 fs, working backwards by 1/4 period yields a starting point of ~ 30 fs. This reveals further information about the lifetime of the CTS and lends physical meaning to the phase shift of $-$ 0.6 rad (26 fs) revealed by the fitting function in Figure 3.15. This ultrafast process is in good agreement with barrierless transition that the CBS of $C_6F_6^-$ is expected to undergo into the VBS.

The final feature, in the grey spectral window of Figure 3.14, consists of low eKE photoelectrons that increase in intensity with increasing t. This feature does not arise from autodetachment of the excess electron from the newly-formed $C_6F_6^- \cdot I$ because it only appears after t_0 and therefore requires the sequential incidence of the pump and probe photons. These photoelectrons also don't correspond to direct detachment by the probe photon from the $C_6F_6^-$ because those have already been assigned to the red spectral window as the molecule vibrates.

In fact, as can be seen in Figure 3.15, this feature in the grey spectral window increases in a stepwise fashion, almost directly out-of-phase with the oscillations in red. Although the exact mechanism remains unclear, the most plausible explanation is that during the vibrations, the probe photon moves in and out of resonance near the outer turning point with an electronic excited state of $C_6F_6^-$. Following this electronic excitation, probably to a vibrationally hot state, the excess electron autodetaches. This mechanism explains why the photoelectrons in the grey spectral window have low eKE and a similar periodicity to the oscillations in red. Further clarity may be sought by performing PES on $C_6F_6^-$ in the region around $h\nu = 1.55$ eV in order to ascertain whether there is indeed an electronic excited state of the anion there that undergoes autodetachment.

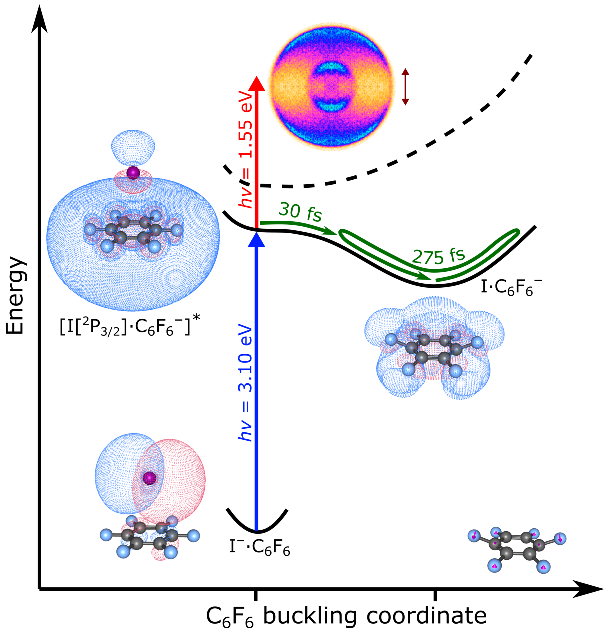

Figure 3.18: An energy schematic of the time-resolved photoelectron spectra of $C_6F_6 \cdot I^-$. The photons are indicated by the coloured arrows. The solid black lines denote the potential energy surfaces of the charged cluster and the dashed line of the neutral cluster. Each electronic state is accompanied by a visualisation of the calculated orbital in which the excess electron resides. The colour-inverted VMI heat map of the t_0 spectrum, which displays the positive β_2 PAD, is shown at the top of the diagram.

3.2.6 Conclusion

Putting all this evidence together, the picture shown in Figure 3.18 presents a coherent mechanism for the time-resolved experiment. The 3.10 eV pump photon excites the excess electron into a short-lived CTS. The lifetime of this state is ~ 30 ± 10 fs as it undergoes a barrierless transition, injecting the electron into the D_0 ground state of the $C_6F_6^-$ anion. This causes the molecule to undergo vibrations along its buckling coordinate at a frequency of 121 ± 2 cm^{-1}. A visualisation of each of the orbitals, as calculated using DFT and TD-DFT is shown adjacent to each electronic state.

Given the existence of an accessible CTS in the $C_6F_6 \cdot I^-$ cluster; its ultrafast lifetime; the coherent transition it undergoes into the buckled D_0 state of $C_6F_6^-$; the intensity of the photoelectron signal yielded by the CTS; the similarity in the predicted shapes of the $C_6F_6^-$ CBS and $C_6F_6 \cdot I^-$ CTS orbitals; and the difference between the PADs of direct detachment of the excess electron from the

I^- p-orbital compared to the cluster CTS, I therefore argue that the short-lived CTS observed at t_0 is indeed a CBS. The exceeding efficiency and coherence with which the electron is injected into the valence system of the C_6F_6 molecule demonstrates the importance that the CBS is likely to play in the electron capture channel of other similar molecules lacking a permanent multipole moment.

Compared to eBE = 140 meV calculated by Voora for the CBS of C_6F_6, this CBS has a relatively large eBE of 450 meV. This artefact is attributed to the presence of the highly polarisable I atom providing additional stability to the excess electron in the CBS. If Voora's calculations are correct, this implies that $C_6F_6^- \cdot I$ enjoys a cluster cohesion energy ~ 0.3 eV greater than $C_6F_6 \cdot I$. This is similar in magnitude to the increase in cluster cohesion energy of 0.43 eV measured for $C_6F_6 \cdot I^-$ in Figure 3.2 and illustrated in Figure 3.12. The increased eBE is also reflected in the shifted position of the $C_6F_6^- \cdot I$ cluster peak relative to that of $C_6F_6^-$ presented in subplot B of Figure 3.11. Unfortunately, attempts to calculate the energy and geometry of the $C_6F_6^- \cdot I$ cluster were inconclusive.

The high eBE of the excess electron in the $C_6F_6^- \cdot I$ cluster caused some of the referees of this paper to ask how the assignment of the CTS to a CBS was a more convincing explanation than a direct injection of the excess electron into the valence system of the C_6F_6 molecule. This author is convinced that the CBS assignment is more valid than the direct injection mechanism in particular due to the change in electronic character evident in the PAD false colour plot presented in Figure 3.14.

3.3 Outlook

In order to further validate this observation of the CBS of $C_6F_6^-$, an identical study should be performed on analogous molecules such as C_6Cl_6, which may also be able to host a CBS and may provide additional information regarding the effect of polarisability on the dynamics of the CBS. It would also be interesting to probe the $(C_6F_6)_2 \cdot I^-$ cluster because Voora also predicted a CBS for $(C_6F_6)_2^-$. On the other hand, C_6H_6 has a negative EA and therefore does not readily form an anion[159]. If the interpretation of the above data proves to be correct, time-resolved photoelectron studies of $C_6H_6 \cdot I^-$ clusters will reveal no CBS.

There remain a number of fields in which it would be of interest to explore the role of the CBS in electron capture by molecules without a permanent multipole moment.

- Polycyclic aromatic hydrocarbons observed in the interstellar medium undergo chemistry that requires the formation of anions[160] but some of these molecules have no permanent multipole moment that could give rise to a DBS or QBS. It would be interesting to establish to what extent CBSs plays a role in these mechanisms.
- Although individual nucleobases have a permanent dipole and have been shown to host DBSs that acts as a doorway to electron capture[1], nucleobase pairs arranged in their stacked configuration have a trivial net dipole moment. Given that deoxyribonucleic acid (DNA) damage by low energy electron impact remains a contentious issue[161–163], it would be interesting to see whether the dynamics of electron capture by paired nucleobases are significantly different from that of individual nucleobases.
- Species such as C_{60}[9] and clusters of Xe[40] and Kr are also supposedly able to host CBSs with significantly longer lifetimes than the CBS of $C_6F_6^-$ and it would be interesting to probe their dynamics.

The task for which this experiment was originally designed was to study water cluster anions ($(H_2O)_n^-$) and the hydrated electron (e_{aq}^-). The conditions under which the molecular beam is presently generated proved unsuitable for making $(H_2O)_n^-$. However, with the use of an alternative ionisation method that introduces an effusive gas discharge perpendicular to the supersonic expansion[164], electrons can be entrained more gently into the beam where $(H_2O)_n^-$ are generated. Furthermore, with the addition of a Paul Trap attached to a cryohead, the temperature of these $(H_2O)_n^-$ could be precisely and accurately controlled. In this way a study could be performed to ascertain the cluster size-and temperature-dependence of the binding character of e^-_{aq}. Subsequently, biomolecules could be introduced to determine the effect of hydration shells on their electron capture dynamics.

The versatility of this instrument to generate and observe a variety of different species is substantial, owing in large part to its modular construction. I hope it will be fruitful and productive for many years to come and I look forward to reading in the literature about the results it produces.

Bibliography

[1] W.-L. Li, A. Kunin, E. Matthews, N. Yoshikawa, C. E. H. Dessent and D. M. Neumark, *The Journal of Chemical Physics*, 2016, **145**, 044319.

[2] B. Boudaiffa, *Science*, 2000, **287**, 1658–1660.

[3] P. J. Sarre, *Monthly Notices of the Royal Astronomical Society*, 2000, **313**, L14–L16.

[4] T. J. Millar, C. Walsh and T. A. Field, *Chemical Reviews*, 2017, **117**, 1765–1795.

[5] A. Chutjian, A. Garscadden and J. Wadehra, *Physics Reports*, 1996, **264**, 393–470.

[6] T. Sommerfeld and K. D. Jordan, *Journal of the American Chemical Society*, 2006, **128**, 5828–5833.

[7] V. P. Vysotskiy, L. S. Cederbaum, T. Sommerfeld, V. K. Voora and K. D. Jordan, *Journal of Chemical Theory and Computation*, 2012, **8**, 893–900.

[8] J. Simons, *The Journal of Physical Chemistry A*, 2008, **112**, 6401–6511.

[9] V. K. Voora, L. S. Cederbaum and K. D. Jordan, *The Journal of Physical Chemistry Letters*, 2013, **4**, 849–853.

[10] H. Fielding, *Annual Review of Physical Chemistry*, 2005, **56**, 91–117.

[11] J. Simons, *Journal of the American Chemical Society*, 1981, **103**, 3971–3976.

[12] K. D. Jordan and F. Wang, *Annual Review of Physical Chemistry*, 2003, **54**, 367–396.

[13] E. Fermi and E. Teller, *Physical Review*, 1947, **72**, 399–408.

[14] A. S. Wightman, *Physical Review*, 1950, **77**, 521–528.

[15] M. Gutowski, K. D. Jordan and P. Skurski, *The Journal of Physical Chemistry A*, 1998, **102**, 2624–2633.

[16] O. H. Crawford, *Proceedings of the Physical Society*, 1967, **91**, 279–284.

[17] O. H. Crawford and A. Dalgarno, *Chemical Physics Letters*, 1967, **1**, 23.

[18] O. H. Crawford and W. R. Garrett, *The Journal of Chemical Physics*, 1977, **66**, 4968–4970.

[19] M. Gutowski and P. Skurski, *The Journal of Physical Chemistry B*, 1997, **101**, 9143–9146.

[20] F. Wang and K. D. Jordan, *The Journal of Chemical Physics*, 2001, **114**, 10717–10724.

[21] R. F. Wallis, R. Herman and H. W. Milnes, *Journal of Molecular Spectroscopy*, 1960, **4**, 51–74.

[22] M. Mittleman and V. Myerscough, *Physics Letters*, 1966, **23**, 545–546.

[23] C. A. Coulson and M. Walmsley, *Proceedings of the Physical Society*, 1967, **91**, 31–32.

[24] W. B. Brown and R. E. Roberts, *The Journal of Chemical Physics*, 1967, **46**, 2006–2007.

[25] J.-M. Lévy-Leblond, *Physical Review*, 1967, **153**, 1–4.

[26] J. E. Turner, V. E. Anderson and K. Fox, *Physical Review*, 1968, **174**, 81–89.

[27] S. F. Wong and G. J. Schulz, *Physical Review Letters*, 1974, **33**, 134–136.

[28] K. Rohr and F. Linder, *Journal of Physics B: Atomic and Molecular Physics*, 1976, **9**, 2521–2537.

[29] A. H. Zimmerman and J. I. Brauman, *The Journal of Chemical Physics*, 1977, **66**, 5823–5825.

[30] R. L. Jackson, A. H. Zimmerman and J. I. Brauman, *The Journal of Chemical Physics*, 1979, **71**, 2088.

[31] R. L. Jackson, P. C. Hiberty and J. I. Brauman, *The Journal of Chemical Physics*, 1981, **74**, 3705–3712.

[32] K. R. Lykke, R. D. Mead and W. C. Lineberger, *Physical Review Letters*, 1984, **52**, 2221–2224.

[33] M. A. Yandell, S. B. King and D. M. Neumark, *The Journal of Chemical Physics*, 2014, **140**, 184317.

[34] K. D. Jordan and J. F. Liebman, *Chemical Physics Letters*, 1979, **62**, 143–147.

[35] M. Gutowski and P. Skurski, *Chemical Physics Letters*, 1999, **303**, 65–75.

[36] G.-Z. Zhu, Y. Liu and L.-S. Wang, *Physical Review Letters*, 2017, **119**, 023002.

[37] M. Gutowski, P. Skurski, A. I. Boldyrev, J. Simons and K. D. Jordan, *Physical Review A*, 1996, **54**, 1906–1909.

[38] V. K. Voora and K. D. Jordan, *Nano Letters*, 2014, **14**, 4602–4606.

[39] T. Sommerfeld, B. Bhattarai, V. P. Vysotskiy and L. S. Cederbaum, *The Journal of Chemical Physics*, 2010, **133**, 114301.

[40] V. G. Bezchastnov, V. P. Vysotskiy and L. S. Cederbaum, *Physical Review Letters*, 2011, **107**, 133401.

[41] A. Hibbert, K. L. Bell and K. A. Berrington, *Journal of Physics B: Atomic and Molecular Physics*, 1987, **20**, L349–L352.

[42] J. N. Bull and J. R. R. Verlet, *Science Advances*, 2017, **3**, e1603106.

[43] H. Hertz, *Annalen der Physik und Chemie*, 1887, **267**, 983–1000.

[44] M. Planck, *Annalen der Physik*, 1900, **306**, 719–737.

[45] A. Einstein, *Annalen der Physik*, 1905, **322**, 132–148.

[46] K. T. Compton, *Physical Review*, 1913, **1**, 382–392.

[47] D. W. Cornelius, *Physical Review*, 1913, **1**, 16–34.

[48] A. L. Hughes, *Philosophical Transactions of the Royal Society A: Mathematical, Physical and Engineering Sciences*, 1913, **212**, 205–226.

[49] E. M. Purcell, *Physical Review*, 1938, **54**, 818–826.

[50] P. Kruit and F. H. Read, *Journal of Physics E: Scientific Instruments*, 1983, **16**, 313–324.

[51] A. T. J. B. Eppink and D. H. Parker, *Review of Scientific Instruments*, 1997, **68**, 3477.

[52] E. Condon, *Physical Review*, 1926, **28**, 1182–1201.

[53] D. A. Horke and J. R. R. Verlet, *Physical Chemistry Chemical Physics*, 2012, **14**, 8511.

[54] B. Baguenard, J. C. Pinaré, C. Bordas and M. Broyer, *Physical Review A*, 2001, **63**, 023204.

[55] A. D. Buckingham, B. J. Orr and J. M. Sichel, *Philosophical Transactions of the Royal Society A: Mathematical, Physical and Engineering Sciences*, 1970, **268**, 147–157.

[56] E. P. Wigner, *Physical Review*, 1948, **73**, 1002–1009.

[57] D. M. Wetzel and J. I. Brauman, *Chemical Reviews*, 1987, **87**, 607–622.

[58] K. L. Reid, *Annual Review of Physical Chemistry*, 2003, **54**, 397–424.

[59] C. S. Anstöter, J. N. Bull and J. R. Verlet, *International Reviews in Physical Chemistry*, 2016, **35**, 509–538.

[60] D. A. Horke, A. S. Chatterley and J. R. R. Verlet, *The Journal of Chemical Physics*, 2013, **139**, 084302.

[61] J. Lecointre, G. M. Roberts, D. A. Horke and J. R. R. Verlet, *The Journal of Physical Chemistry A*, 2010, **114**, 11216–11224.

[62] C. S. Anstöter, C. R. Dean and J. R. R. Verlet, *Physical Chemistry Chemical Physics*, 2017, **advance article**, pages pending.

[63] R. F. Gunion, M. K. Gilles, M. L. Polak and W. Lineberger, *International Journal of Mass Spectrometry and Ion Processes*, 1992, **117**, 601–620.

[64] J. Schiedt and R. Weinkauf, *The Journal of Chemical Physics*, 1999, **110**, 304–314.

[65] D. J. Nelson, W. K. Gichuhi, E. M. Miller, J. H. Lehman and W. C. Lineberger, *The Journal of Chemical Physics*, 2017, **146**, 074302.

[66] C. W. West, J. N. Bull, E. Antonkov and J. R. R. Verlet, *The Journal of Physical Chemistry A*, 2014, **118**, 11346–11354.

[67] J. N. Bull, C. W. West and J. R. R. Verlet, *Chemical Science*, 2015, **6**, 1578–1589.

[68] J. N. Bull, C. W. West and J. R. R. Verlet, *Physical Chemistry Chemical Physics*, 2015, **17**, 16125–16135.

[69] J. N. Bull, C. W. West and J. R. R. Verlet, *Physical Chemistry Chemical Physics*, 2015, **17**, 32464–32471.

[70] C. W. West, J. N. Bull, A. S. Hudson, S. L. Cobb and J. R. R. Verlet, *The Journal of Physical Chemistry B*, 2015, **119**, 3982–3987.

[71] J. N. Bull, C. W. West and J. R. R. Verlet, *Chemical Science*, 2016, **7**, 5352–5361.

[72] C. W. West, J. N. Bull, D. A. Woods and J. R. Verlet, *Chemical Physics Letters*, 2016, **645**, 138–143.

[73] J. N. Bull and J. R. R. Verlet, *Physical Chemistry Chemical Physics*, 2017, **19**, 26589–26595.

[74] L. H. Stanley, C. S. Anstöter and J. R. R. Verlet, *Chemical Science*, 2017, **8**, 3054–3061.

[75] A. H. Zewail, *The Journal of Physical Chemistry A*, 2000, **104**, 5660–5694.

[76] A. H. Zewail, *Pure and Applied Chemistry*, 2000, **72**, 2219–2231.

[77] W. Sibbett, A. A. Lagatsky and C. T. A. Brown, *Optics Express*, 2012, **20**, 6989.

[78] J. R. R. Verlet, *Chemical Society Reviews*, 2008, **37**, 505–517.

[79] G. M. Roberts, J. Lecointre, D. A. Horke and J. R. R. Verlet, *Physical Chemistry Chemical Physics*, 2010, **12**, 6226.

[80] D. A. Horke, G. M. Roberts and J. R. R. Verlet, *The Journal of Physical Chemistry A*, 2011, **115**, 8369–8374.

[81] D. A. Horke and J. R. R. Verlet, *Physical Chemistry Chemical Physics*, 2011, **13**, 19546.

[82] D. A. Horke, A. S. Chatterley and J. R. R. Verlet, *Physical Review Letters*, 2012, **108**, 083003.

[83] D. A. Horke, A. S. Chatterley and J. R. R. Verlet, *The Journal of Physical Chemistry Letters*, 2012, **3**, 834–838.

[84] A. S. Chatterley, D. A. Horke and J. R. R. Verlet, *Physical Chemistry Chemical Physics*, 2012, **14**, 16155.

[85] C. R. S. Mooney, D. A. Horke, A. S. Chatterley, A. Simperler, H. H. Fielding and J. R. R. Verlet, *Chemical Science*, 2013, **4**, 921–927.

[86] D. A. Horke, Q. Li, L. Blancafort and J. R. R. Verlet, *Nature Chemistry*, 2013, **5**, 711–717.

[87] A. S. Chatterley, C. W. West, G. M. Roberts, V. G. Stavros and J. R. R. Verlet, *The Journal of Physical Chemistry Letters*, 2014, **5**, 843–848.

[88] J. R. R. Verlet, D. A. Horke and A. S. Chatterley, *Physical Chemistry Chemical Physics*, 2014, **16**, 15043–15052.

[89] A. S. Chatterley, C. W. West, V. G. Stavros and J. R. R. Verlet, *Chemical Science*, 2014, **5**, 3963–3975.

[90] D. A. Horke, A. S. Chatterley, J. N. Bull and J. R. R. Verlet, *The Journal of Physical Chemistry Letters*, 2015, **6**, 189–194.

[91] J.-X. Yu, R. R. Hallac, S. Chiguru and R. P. Mason, *Progress in Nuclear Magnetic Resonance Spectroscopy*, 2013, **70**, 25–49.

[92] T. M. Miller, J. M. V. Doren and A. Viggiano, *International Journal of Mass Spectrometry*, 2004, **233**, 67–73.

[93] Y. Xie, H. F. Schaefer-III and F. A. Cotton, *Chemical Communications*, 2002, 102–103.

[94] X.-J. Hou and M.-B. Huang, *Journal of Molecular Structure: THEOCHEM*, 2003, **638**, 209–214.

[95] A. Nakajima, T. Taguwa, K. Hoshino, T. Sugioka, T. Naganuma, F. Oho, K. Watanabe, K. Nakao, Y. Konishi, R. Kishi and K. Kaya, *Chemical Physics Letters*, 1993, **214**, 22–26.

[96] S. N. Eustis, D. Wang, K. H. Bowen and G. N. Patwari, *The Journal of Chemical Physics*, 2007, **127**, 114312.

[97] V. K. Voora and K. D. Jordan, *The Journal of Physical Chemistry A*, 2014, **118**, 7201–7205.

[98] K. S. Gant and L. G. Christophorou, *The Journal of Chemical Physics*, 1976, **65**, 2977–2981.

[99] L. Nyikos, C. A. M. van den Ende, J. M. Warman and A. Hummel, *The Journal of Physical Chemistry*, 1980, **84**, 1154–1155.

[100] C. Gahl, K. Ishioka, Q. Zhong, A. Hotzel and M. Wolf, *Faraday Discussions*, 2000, **117**, 191–202.

[101] A. W. Castleman and K. H. Bowen, *The Journal of Physical Chemistry*, 1996, **100**, 12911–12944.

[102] J. Tang, A. R. W. McKellar, F. Mezzacapo and S. Moroni, *Physical Review Letters*, 2004, **92**, 145503.

[103] T. Wende, N. Heine, T. I. Yacovitch, K. R. Asmis, D. M. Neumark and L. Jiang, *Physical Chemistry Chemical Physics*, 2016, **18**, 267–277.

[104] R. N. Barnett, U. Landman, C. L. Cleveland and J. Jortner, *The Journal of Chemical Physics*, 1988, **88**, 4429.

[105] R. N. Barnett, U. Landman, G. Makov and A. Nitzan, *The Journal of Chemical Physics*, 1990, **93**, 6226.

[106] J. V. Coe, G. H. Lee, J. G. Eaton, S. T. Arnold, H. W. Sarkas, K. H. Bowen, C. Ludewigt, H. Haberland and D. R. Worsnop, *The Journal of Chemical Physics*, 1990, **92**, 3980.

[107] L. Lehr, *Science*, 1999, **284**, 635–638.

[108] D. M. Bartels, *The Journal of Chemical Physics*, 2001, **115**, 4404.

[109] A. E. Bragg, *Science*, 2004, **306**, 669–671.

[110] N. I. Hammer, *Science*, 2004, **306**, 675–679.

[111] A. E. Bragg, J. R. R. Verlet, A. Kammrath, O. Cheshnovsky and D. M. Neumark, *Journal of the American Chemical Society*, 2005, **127**, 15283–15295.

[112] J. R. R. Verlet, *Science*, 2005, **307**, 93–96.

[113] O. Marsalek, F. Uhlig, T. Frigato, B. Schmidt and P. Jungwirth, *Physical Review Letters*, 2010, **105**, 043002.

[114] R. M. Young and D. M. Neumark, *Chemical Reviews*, 2012, **112**, 5553–5577.

[115] E. Rabinowitch, *Reviews of Modern Physics*, 1942, **14**, 112–131.

[116] A. V. Davis, M. T. Zanni, C. Frischkorn and D. M. Neumark, *Journal of Electron Spectroscopy and Related Phenomena*, 2000, **108**, 203–211.

[117] C. Frischkorn, M. T. Zanni, A. V. Davis and D. M. Neumark, *Faraday Discussions*, 2000, **115**, 49–62.

[118] M. T. Zanni, C. Frischkorn, A. V. Davis and D. M. Neumark, *The Journal of Physical Chemistry A*, 2000, **104**, 2527–2530.

[119] M. D. Elola and D. Laria, *The Journal of Chemical Physics*, 2002, **117**, 2238–2245.

[120] J. R. R. Verlet, A. Kammrath, G. B. Griffin and D. M. Neumark, *The Journal of Chemical Physics*, 2005, **123**, 4.

[121] A. Kammrath, J. R. R. Verlet, A. E. Bragg, G. B. Griffin and D. M. Neumark, *The Journal of Physical Chemistry A*, 2005, **109**, 11475–11483.

[122] D. E. Szpunar, K. E. Kautzman, A. E. Faulhaber and D. M. Neumark, *The Journal of Chemical Physics*, 2006, **124**, 054318.

[123] O. T. Ehrler, G. B. Griffin, R. M. Young and D. M. Neumark, *The Journal of Physical Chemistry B*, 2009, **113**, 4031–4037.

[124] M. K. Fischer, A. Gliserin, A. Laubereau and H. Iglev, *Journal of Biophotonics*, 2010, **4**, 178–183.

[125] R. M. Young, M. A. Yandell and D. M. Neumark, *The Journal of Chemical Physics*, 2011, **134**, 124311.

[126] R. M. Young, R. J. Azar, M. A. Yandell, S. B. King, M. Head-Gordon and D. M. Neumark, *Molecular Physics*, 2012, **110**, 1787–1799.

[127] M. A. Yandell, R. M. Young, S. B. King and D. M. Neumark, *The Journal of Physical Chemistry A*, 2012, **116**, 2750–2757.

[128] M. A. Yandell, S. B. King and D. M. Neumark, *Journal of the American Chemical Society*, 2013, **135**, 2128–2131.

[129] S. B. King, M. A. Yandell and D. M. Neumark, *Faraday Discussions*, 2013, **163**, 59.

[130] S. B. King, M. A. Yandell, A. B. Stephansen and D. M. Neumark, *The Journal of Chemical Physics*, 2014, **141**, 224310.

[131] A. Kothe, M. Wilke, A. Moguilevski, N. Engel, B. Winter, I. Y. Kiyan and E. F. Aziz, *Physical Chemistry Chemical Physics*, 2015, **17**, 1918–1924.

[132] A. B. Stephansen, S. B. King, Y. Yokoi, Y. Minoshima, W.-L. Li, A. Kunin, T. Takayanagi and D. M. Neumark, *The Journal of Chemical Physics*, 2015, **143**, 104308.

[133] S. B. King, A. B. Stephansen, Y. Yokoi, M. A. Yandell, A. Kunin, T. Takayanagi and D. M. Neumark, *The Journal of Chemical Physics*, 2015, **143**, 024312.

[134] H. Kallmann and F. Reiche, *Zeitschrift für Physik*, 1921, **6**, 352–375.

[135] G. Scoles, D. R. Miller, W. R. Gentry, H. Pauly, D. Bassi, U. Hefter, K. Bergmann, M. Zen, J. Reuss, C. J. N. van den Meijdenberg, D. J. Auerbach, M. Kappes, S. Leutwyler, K. Ploog, U. Valbusa, U. Buck, J. J. H. van den Biesen, Y. T. Lee, P. J. Dagdigian, S. Stolte, R. Düren and S. Iannotta, *Atomic and Molecular Beam Methods*, Oxford University Press, 200 Madison Avenue, New York, New York 10016, 1988, vol. 1.

[136] S. Y. T. van de Meerakker, H. L. Bethlem, N. Vanhaecke and G. Meijer, *Chemical Reviews*, 2012, **112**, 4828–4878.

[137] A. Naß and E. Steffens, *Nuclear Instruments and Methods in Physics Research Section A: Accelerators, Spectrometers, Detectors and Associated Equipment*, 2009, **598**, 653–666.

[138] M. D. Morse, in *Experimental Methods in the Physical Sciences*, Elsevier, 1996, pp. 21–47.

[139] U. Even, J. Jortner, D. Noy, N. Lavie and C. Cossart-Magos, *The Journal of Chemical Physics*, 2000, **112**, 8068–8071.

[140] N. Lavie and U. Even, *The Even-Lavie High Temperature Valve Instruction Manual*, https://sites.google.com/site/evenlavievalve/manuals, accessed 23/05/2014, 2011.

[141] C. Li, A. Lahmam-Bennani, E. M. S. Casagrande and C. D. Cappello, *Journal of Physics B: Atomic, Molecular and Optical Physics*, 2011, **44**, 115201.

[142] L. K. Jha, S. Kumar and B. N. Roy, *The European Physical Journal D*, 2006, **40**, 101–106.

[143] W. Wiley and I. McLaren, *Review of Scientific Instruments*, 1955, **26**, 1150–1157.

[144] A. T. Clark, J. P. Crooks, I. Sedgwick, R. Turchetta, J. W. L. Lee, J. J. John, E. S. Wilman, L. Hill, E. Halford, C. S. Slater, B. Winter, W. H. Yuen, S. H. Gardiner, M. L. Lipciuc, M. Brouard, A. Nomerotski and C. Vallance, *The Journal of Physical Chemistry A*, 2012, **116**, 10897–10903.

[145] J. O. F. Thompson, C. Amarasinghe, C. D. Foley and A. G. Suits, *The Journal of Chemical Physics*, 2017, **147**, 013913.

[146] E. Wrede, S. Laubach, S. Schulenburg, A. Brown, E. R. Wouters, A. J. Orr-Ewing and M. N. R. Ashfold, *The Journal of Chemical Physics*, 2001, **114**, 2629–2646.

[147] K. P. Huber, G. Herzberg, J. W. Gallagher and R. D. Johnson III, *NIST Chemistry WebBook, NIST Standard Reference Database Number 69*, U.S. Department of Commerce, accessed 08/06/2017, vol. Constants of Diatomic Molecules.

[148] K. R. Lykke, D. M. Neumark, T. Andersen, V. J. Trapa and W. C. Lineberger, *The Journal of Chemical Physics*, 1987, **87**, 6842–6853.

[149] C. R. Patrick and G. S. Prosser, *Transactions of the Faraday Society*, 1964, **60**, 700.

[150] Y. Shao, Z. Gan, E. Epifanovsky, A. T. Gilbert, M. Wormit, J. Kussmann, A. W. Lange, A. Behn, J. Deng, X. Feng, D. Ghosh, M. Goldey, P. R. Horn, L. D. Jacobson, I. Kaliman, R. Z. Khaliullin, T. Kus, A. Landau, J. Liu, E. I. Proynov, Y. M. Rhee, R. M. Richard, M. A. Rohrdanz, R. P. Steele, E. J. Sundstrom, H. L. Woodcock, P. M. Zimmerman, D. Zuev, B. Albrecht, E. Alguire, B. Austin, G. J. O. Beran, Y. A. Bernard, E. Berquist, K. Brandhorst, K. B. Bravaya, S. T. Brown, D. Casanova, C.-M. Chang, Y. Chen, S. H. Chien, K. D. Closser, D. L. Crittenden, M. Diedenhofen, R. A. DiStasio, H. Do, A. D. Dutoi, R. G. Edgar, S. Fatehi, L. Fusti-Molnar, A. Ghysels, A. Golubeva-Zadorozhnaya, J. Gomes, M. W. Hanson-Heine, P. H. Harbach, A. W. Hauser, E. G. Hohenstein, Z. C. Holden, T.-C. Jagau, H. Ji, B. Kaduk, K. Khistyaev, J. Kim, J. Kim, R. A. King, P. Klunzinger, D. Kosenkov, T. Kowalczyk, C. M. Krauter, K. U. Lao, A. D. Laurent, K. V. Lawler, S. V. Levchenko, C. Y. Lin, F. Liu, E. Livshits, R. C. Lochan, A. Luenser, P. Manohar, S. F. Manzer, S.-P. Mao, N. Mardirossian, A. V. Marenich, S. A. Maurer, N. J. Mayhall, E. Neuscamman, C. M. Oana, R. Olivares-Amaya, D. P. O'Neill, J. A. Parkhill, T. M. Perrine, R. Peverati, A. Prociuk, D. R. Rehn, E. Rosta, N. J. Russ, S. M. Sharada, S. Sharma, D. W. Small, A. Sodt, T. Stein,

D. Stück, Y.-C. Su, A. J. Thom, T. Tsuchimochi, V. Vanovschi, L. Vogt, O. Vydrov, T. Wang, M. A. Watson, J. Wenzel, A. White, C. F. Williams, J. Yang, S. Yeganeh, S. R. Yost, Z.-Q. You, I. Y. Zhang, X. Zhang, Y. Zhao, B. R. Brooks, G. K. Chan, D. M. Chipman, C. J. Cramer, W. A. Goddard, M. S. Gordon, W. J. Hehre, A. Klamt, H. F. Schaefer, M. W. Schmidt, C. D. Sherrill, D. G. Truhlar, A. Warshel, X. Xu, A. Aspuru-Guzik, R. Baer, A. T. Bell, N. A. Besley, J.-D. Chai, A. Dreuw, B. D. Dunietz, T. R. Furlani, S. R. Gwaltney, C.-P. Hsu, Y. Jung, J. Kong, D. S. Lambrecht, W. Liang, C. Ochsenfeld, V. A. Rassolov, L. V. Slipchenko, J. E. Subotnik, T. V. Voorhis, J. M. Herbert, A. I. Krylov, P. M. Gill and M. Head-Gordon, *Molecular Physics*, 2014, **113**, 184–215.

[151] T. Yanai, D. P. Tew and N. C. Handy, *Chemical Physics Letters*, 2004, **393**, 51–57.

[152] T. H. Dunning, *The Journal of Chemical Physics*, 1989, **90**, 1007–1023.

[153] D. Serxner, C. E. H. Dessent and M. A. Johnson, *The Journal of Chemical Physics*, 1996, **105**, 7231.

[154] R. J. Peláez, C. Blondel, C. Delsart and C. Drag, *Journal of Physics B: Atomic, Molecular and Optical Physics*, 2009, **42**, 125001.

[155] R. D. Mead, K. R. Lykke, W. C. Lineberger, J. Marks and J. I. Brauman, *The Journal of Chemical Physics*, 1984, **81**, 4883–4892.

[156] D. Klar, M.-W. Ruf and H. Hotop, *Chemical Physics Letters*, 1992, **189**, 448–454.

[157] A. Stolow, V. Blanchet, M. Z. Zgierski and T. Seideman, *Nature*, 1999, **401**, 52–54.

[158] P. R. Stannard and W. M. Gelbart, *The Journal of Physical Chemistry*, 1981, **85**, 3592–3599.

[159] S. Chowdhury, T. Heinis and P. Kebarle, *Journal of the American Chemical Society*, 1986, **108**, 4662–4663.

[160] M. C. McCarthy, C. A. Gottlieb, H. Gupta and P. Thaddeus, *The Astrophysical Journal*, 2006, **652**, L141–L144.

[161] J. Nguyen, Y. Ma, T. Luo, R. G. Bristow, D. A. Jaffray and Q.-B. Lu, *Proceedings of the National Academy of Sciences*, 2011, **108**, 11778–11783.

[162] A. Kumar, A. Adhikary, L. Shamoun and M. D. Sevilla, *The Journal of Physical Chemistry B*, 2016, **120**, 2115–2123.

[163] K. Westphal, J. Wiczk, J. Miloch, G. Kciuk, K. Bobrowski and J. Rak, *Organic & Biomolecular Chemistry*, 2015, **13**, 10362–10369.

[164] Y.-J. Lu, J. H. Lehman and W. C. Lineberger, *The Journal of Chemical Physics*, 2015, **142**, 044201.

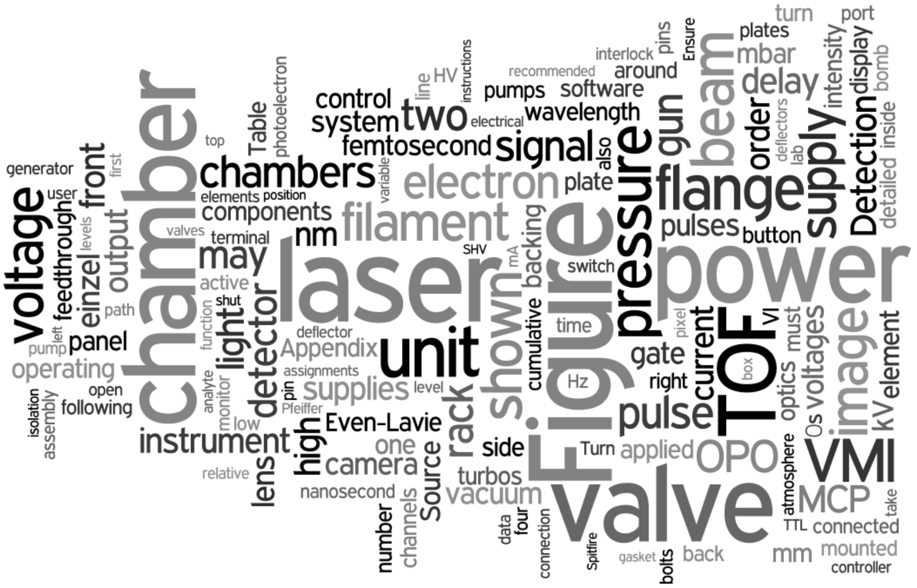

This manual contains details of the specifications of the instrument and its component parts and will help users to operate and maintain the mechanical and electronic systems of the instrument safely.

Regarding its operation for experimentation, the reader will best be able to utilise the instrument to its full potential if they fully understand how each parameter affects the unseen processes within the instrument and how these parameters are interdependent. Take the time to learn and understand what each switch and dial does so you can plan and predict how changes to the parameters ought to affect the output signal.

Regarding maintenance of the instrument, while safeguards have been built in to the design of the instrument, various delicate and expensive components are still liable to damage or break if operated outside of the recommended parameters. Please ensure you follow procedures and instructions as carefully as possible to avoid inconveniencing your own work. Similarly, although the operation of the instrument is not particularly complicated and the design was intended to be as modular and straightforward as possible, some assemblies within the instrument are somewhat fiddly and require good manual dexterity to maintain.

Appendix A

Instrument controls

A.1 Electronics

The instrument is served by a rack of a dozen power supplies that deliver the necessary voltages and currents to the electrostatic optics, detectors and other components at the appropriate timings. The following is a brief description of each unit, its function and output.

A.1.1 Pulse generator

The pulse generator or delay generator, seen in Figure A.1, is the beating heart of the experiment, dictating the relative timings of each element within the instrument. The Quantum Composers 9520 Series pulse generator hosts 8 independent output channels with variable trigger time, pulse duration and output voltage. Tables A.1 and A.2 describe the two regimes under which the experiment runs, depending on whether it is synchronised with the 10 Hz nanosecond OPO laser or the 950 Hz femtosecond laser. In fact, this delay generator serves as the time-keeper for the entire lab as it triggers both lasers and both molecular beam experiments simultaneously.

Table A.1: Channel outputs of the Quantum Composers 9520 Series delay generator when the instrument is synchronised with the 10 Hz nanosecond OPO laser. In this configuration, the other molecular beam experiment in the lab, referred to as *The Ox*, is synchronised to the 950 Hz femtosecond laser system and both can run simultaneously. The *RATE* is therefore determined by the optimised frequency of the femtosecond laser system and the duty cycle applied to channels A, B, C, E, G and H enable them to operate at 10 Hz.
* negative delay, typically around 600 - 800 µs, depending on the analyte.
** negative delay corresponding to ~93.5% of the TOF of the analyte.
*** negative delay with modulus no smaller than 230 µs. This delay controls the pump laser intensity delivered to the OPO system. The shorter the delay, the higher the intensity. The optics in the OPO can be severely damaged if the pump laser intensity is too high.

Channel	**Description**	**Width**	**Delay**	**Sync**	**Polarity**	**Output**	**Duty cycle**
A	pulse valve	5 µs	variable*	B	active high	TTL	94 off, 1 on
B	TOF plates	1 µs	variable**	C	active high	TTL	94 off, 1 on
C	VMI plates	113 ns	233 ns	H	active high	10 V	94 off, 1 on
D	femtosecond laser	5 µs	0 ns	t_0	active high	TTL	normal
E	VMI camera	10 µs	– 100 µs	C	active high	TTL	94 off, 1 on
F	*The Ox*	5 µs	0 ns	D	active high	TTL	normal
G	nanosecond laser flashlamp	2 µs	variable***	H	active low	TTL	94 off, 1 on
H	nanosecond laser Q-switch	2 µs	1.040 ms	t_0	active low	TTL	94 off, 1 on
RATE	t_0	1.05247 ms	–	–	–	–	–

Table A.2: Channel outputs of the Quantum Composers 9520 Series delay generator when the instrument is synchronised with the 950 Hz femtosecond laser system. In this configuration, the other molecular beam experiment in the lab, referred to as *The Ox*, is synchronised to the 10 Hz nanosecond OPO laser and both can run simultaneously. The *RATE* is therefore determined by the optimised frequency of the femtosecond laser system and the duty cycle applied to channels A, B, C and E enable them to operate at a reduced 190 Hz, which is a more appropriate rate for the Even-Lavie pulsed valve. Channels F, G and H operate at 10 Hz.

* negative delay, typically around 600 - 800 µs, depending on the analyte.

** negative delay corresponding to ~93.5% of the TOF of the analyte.

*** negative delay with modulus no smaller than 230 µs. This delay controls the pump laser intensity delivered to the OPO system. The shorter the delay, the higher the intensity. The optics in the OPO can be severely damaged if the pump laser intensity is too high.

Channel	**Description**	**Width**	**Delay**	**Sync**	**Polarity**	**Output**	**Duty cycle**
A	pulse valve	5 µs	variable*	B	active high	TTL	4 off, 1 on
B	TOF plates	1 µs	variable**	C	active high	TTL	4 off, 1 on
C	VMI plates	126 ns	3.064 ns	D	active high	10 V	4 off, 1 on
D	femtosecond laser	5 µs	1.040 ms	t_0	active high	TTL	normal
E	VMI camera	10 µs	− 100 µs	C	active high	TTL	4 off, 1 on
F	*The Ox*	5 µs	0 ns	H	active high	TTL	94 off, 1 on
G	nanosecond laser flashlamp	2 µs	variable***	H	active low	TTL	94 off, 1 on
H	nanosecond laser Q-switch	2 µs	1 ms	t_0	active low	TTL	94 off, 1 on
RATE	t_0	1.05247 ms	–	–	–	–	–

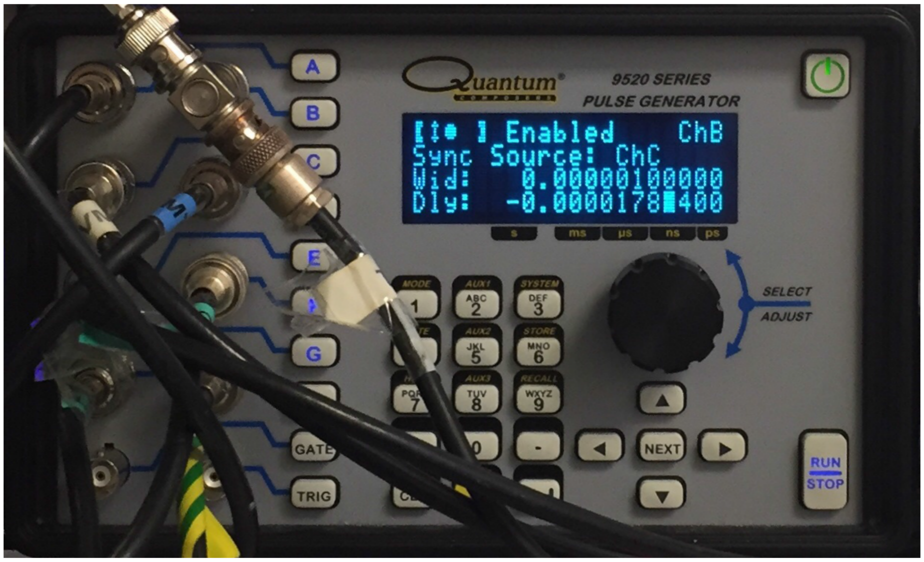

Figure A.1: The front panel of the pulse generator. Channels are selected with the buttons adjacent to their respective output ports and the trigger pulse properties are adjusted with the arrow buttons and the dial. Refer to the manual for detailed operating instructions.

A.1.2 Interlock

The interlock, shown in Figure A.2, is a device primarily responsible for protecting the delicate electronic components in the vacuum chambers. The interlock monitors two channels on the Pfeiffer MaxiGauge™ pressure monitor and will act depending on the pressures in the vacuum chambers relative to some set-points. The VAT series 108 UHV gate valve is controlled via the two square buttons on the left of the front panel. The *OPEN GATE VALVE* button illuminates when the gate valve is open. The mechanical switch on the side of the gate valve itself also indicates its status. The gate valve will only actuate if the pressures in both the Source and Detection chambers are below their respective set-points, as described in Table A.3. There is an override toggle switch next to the gate valve actuation buttons but this should only be used if the vacuum chambers on both sides of the gate valve are vented to atmosphere. The circuit diagrams for the interlock are included in the digital appendix.

The other role of the interlock is to control the power supplied to the detectors and the electron gun filament. These components are particularly susceptible to damage if they are operated at high chamber pressures. The interlock turns off the power supplies for these components when the pressures in their respective chambers rise above the set-points indicated in Table A.3.

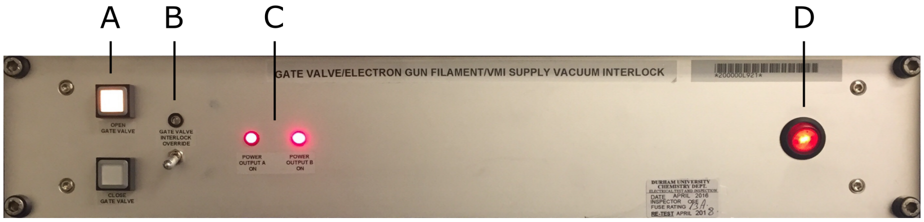

Figure A.2: The front panel of the interlock. A – gate valve actuation buttons; B – gate valve interlock override; C – power output indicator LEDs; D – power button.

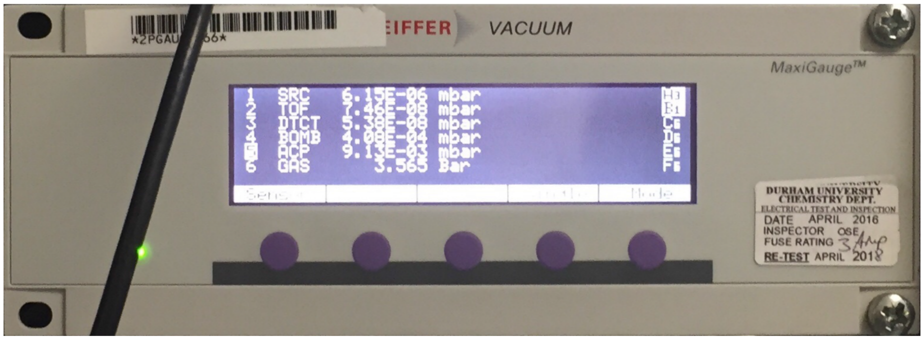

```
1  SRC   6.15E-06 mbar
2  TOF   7.46E-08 mbar
3  DTCT  5.38E-08 mbar
4  BOMB  4.08E-04 mbar
5  ACP   9.13E-03 mbar
6  GAS      3.565 Bar
```

Figure A.3: The front panel of the Pfeiffer MaxiGauge™ pressure monitor.

A.1.3 Pressure monitor

The Pfeiffer MaxiGauge™ pressure monitor, shown in Figure A.3, displays the readings from 6 channels. The channels and their associated gauges are listed in Table A.3. Set-points have been assigned to channels A and C such that if the pressure in those chambers rises above the set-point, a signal is sent to the Interlock to activate safety measures that protect the critical components of the instrument.

Table A.3: The channel assignments of the Pfeiffer MaxiGauge™ pressure monitor. If the pressure reading on channels A or C rise above their respective set-points, a signal is sent to the interlock. A set-point signal from channel A causes the interlock to shut the gate valve and turn off the electron gun filament and TOF detector power supplies. A set-point signal from channel C causes the interlock to shut the gate valve and turn off the VMI power supply.

Channel	**Name**	**Description**	**Pfeiffer gauge**	**Ultimate pressure**	**Operating pressure**	**Set-point**
A	SRC	Source chamber	cold cathode IKR 270	3×10^{-9} mbar	5×10^{-5} mbar	1×10^{-4} mbar
B	TOF	TOF chamber	cold cathode IKR 270	1×10^{-9} mbar	5×10^{-7} mbar	–
C	DTCT	Detection chamber	cold cathode IKR 270	1×10^{-9} mbar	5×10^{-7} mbar	5×10^{-6} mbar
D	BOMB	Edwards bomb backing line	Pirani TPR 280	1×10^{-4} mbar	5×10^{-4} mbar	–
E	ACP	Pfeiffer ACP40 backing line	Pirani TPR 280	5×10^{-3} mbar	1×10^{-2} mbar	–
F	GAS	gas manifold	piezo APR 266	–	variable	–

Table A.4: Typical pulse widths for the Even-Lavie valve under different operating conditions. When synchronised with the femtosecond laser, the valve and subsequent components operate under a 1 on, 4 off duty cycle, as described in Table A.2. The pulse duration and stagnation pressure in the valve must be balanced such that a measurable quantity of ions is produced in the molecular beam while maintaining a manageable gas load in the Source chamber.

Laser Frequency	**Valve frequency**	**Pulse width**
nanosecond @ 10 Hz	10 Hz	35 - 40 µs
femtosecond @ 950 Hz	190 Hz	30 - 35 µs

Figure A.4: The front panel of the Even-Lavie driver unit. Refer to the online user manual[140] for detailed operation instructions.

A.1.4 Even-Lavie pulse controller and heater

The Even-Lavie pulsed valve controller, shown in Figure A.4, amplifies the trigger signal from the pulse generator and relays it to the Even-Lavie valve. The controller delivers a linearly increasing current to the solenoid in the valve for the duration of the pulse width, which can be varied using the buttons on the front panel. It is important to note that this is not a direct measure of the gas pulse duration but what can be said is that the longer the pulse width, the more gas is released into the chamber. However, the longer the pulse width, the more likely the valve is to become magnetised. Typical pulse widths under different operating conditions are detailed in Table A.4.

The Even-Lavie valve can be heated up to 250 °C. This is especially useful for making gas samples of a substance with a low vapour pressure at room temperature. The valve itself has a 7 Ω resistive heating element coiled around its outer housing. The temperature of the valve is monitored by a K-type thermocouple and varied using a 30 W power supply in conjunction with a West 2300 proportional-integral-derivative (PID) controller, shown in Figure A.5.

The Even-Lavie trigger pulse, heater power supply and K-type thermocouple wires are bundled in a conduit and fed into the Source chamber through an off-axis 6-pin feedthrough on the same flange as the valve translator, shown in Figure A.6. This feedthrough consists of three pairs of alumel (–) and chromel (+) pins; one +/– pair is used for the valve thermocouple, the two remaining alumel pins for the heater power supply and the two remaining chromel pins for the trigger pulse. Inside the chamber the pins are connected to the relevant wires with push-fit connectors encased in a 3D printed PLA sheath. The pin assignments are shown in Figure A.7.

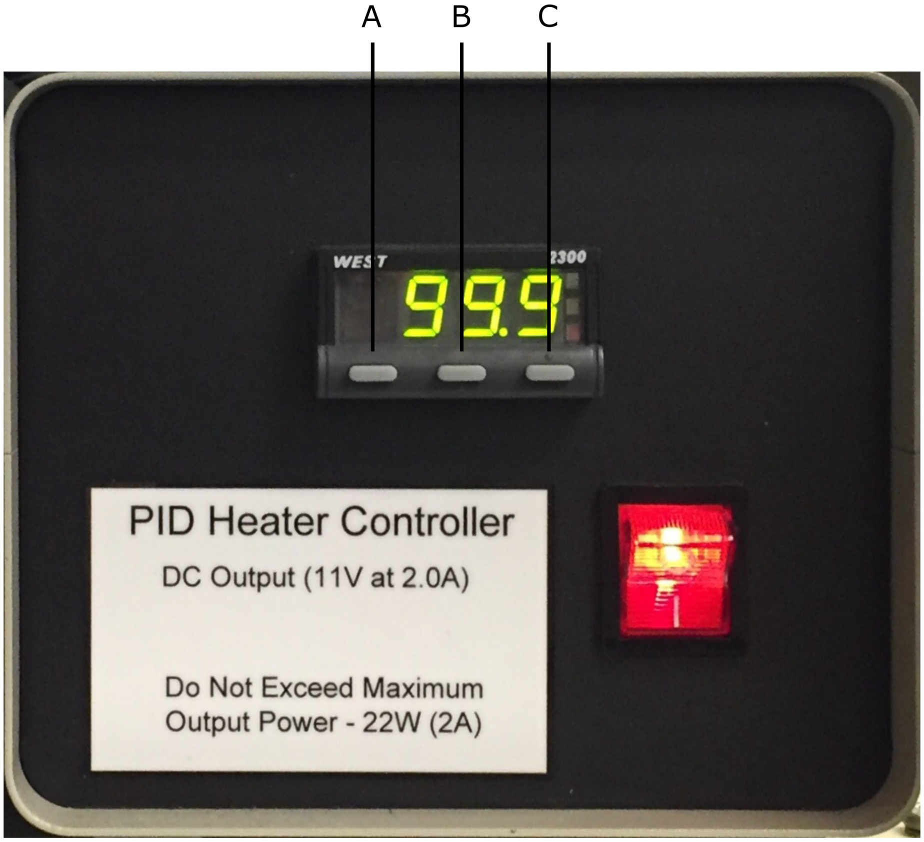

Figure A.5: The front panel of the Even-Lavie heater power supply. A K-type thermocouple monitors the temperature of the valve while the West 2300 PID controller maintains the set-point. The function button, A, switches between *PROC*, which displays the current temperature, and *SP*, which displays the current set-point. The set-point is adjusted by the down and up buttons, B and C respectively. The PID has a habit of overshooting by ~ 10°C and should therefore be turned up slowly.

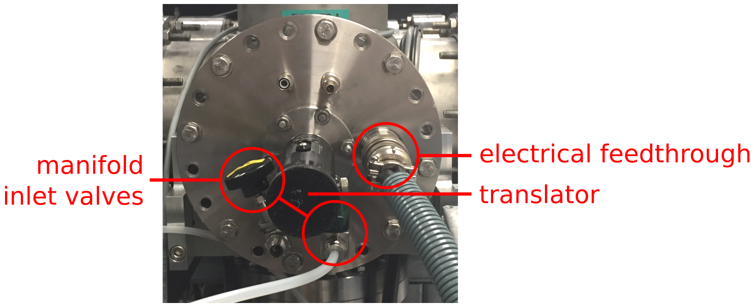

Figure A.6: The Source chamber flange that hosts the translator, the manifold system (not included in the photo) and the electrical feedthrough for controlling the Even-Lavie valve.

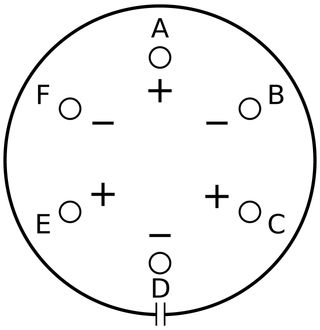

Figure A.7: The pin assignments of the 6-pin electrical feedthrough in the terminal flange of the Source chamber that hosts the connections for Even-Lavie controller and heater, shown in Figure A.6. This perspective represents the arrangement of the pins in the flange viewed from the atmosphere side.
A – chromel thermocouple wire. The wire in the chamber has yellow insulation.
B – alumel thermocouple wire. The wire in the chamber has red insulation.
C – HV valve pulse.
D – valve heating connection 1.
E – 0 V valve pulse.
F – valve heating connection 2.

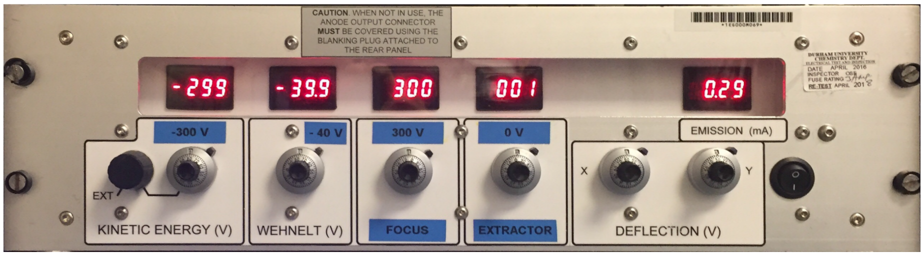

Figure A.8: The front panel of the main electron gun rack unit. From left to right, the dials control the voltages applied the filament, the Wehnelt, the focus, the extractor and the vertical and lateral deflectors near the nozzle of the gun. The ratings of each of the power supplies inside the unit and their respective recommended operating voltages are listed in Table A.5. The dial that changes the voltage at which the filament floats is labelled *KINETIC ENERGY* because this voltage determines the free space kinetic energy of the electrons in the beam. The display on the far right of the panel indicates the difference between the current flowing through in and out of the filament, which corresponds to the electron flux emitted by the filament into the electron beam.

A.1.5 Electron gun power supplies

The electron gun is controlled by three separate power supply units. The main rack unit, shown in Figure A.8, controls the voltages applied to all but one of the electrostatic elements in the electron gun assembly. The anode element is controlled by a HV power supply in a separate rack unit, shown in Figure A.9. Finally, the current passed through the filament is controlled by the rack unit shown in Figure A.10. The filament current supply floats on the voltage applied by the filament power supply in the main rack unit. The function of the electron gun is detailed in Section 2.2.1.1.1.

The main rack unit contains five individual power supplies with voltage and current ratings detailed in Table A.5. The display connected to the Wehnelt power supply is measured with respect to the floating filament voltage (labelled *KINETIC ENERGY* in Figure A.8). All the other electron gun power supply displays are measured relative to 0 V. The circuit diagrams are included in the digital appendix.

The cables between the rack units and the instrument are clustered in black plastic conduit and are connected to the vacuum chamber inside the protective perspex tube shown in Figure A.11. A 3D printed PLA sheath encloses the push-fit connectors that join these cables to the LewVac Components Ltd copper 12-pin 5 kV feedthrough, which is mounted on a CF40 flange. The pin assignments for this feedthrough are detailed in Figure A.12.

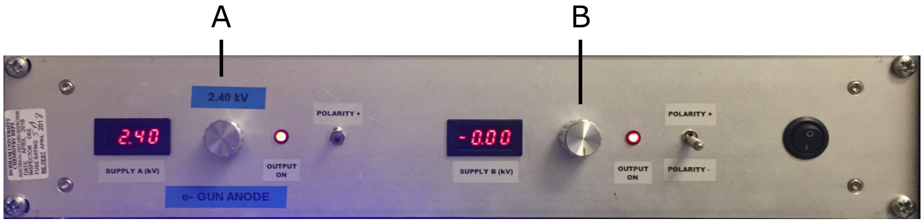

Figure A.9: The front panel of the rack unit that controls the voltage applied to the anode element in the electron gun (A). The rating and recommended operating level of this power supply are detailed in Table A.5. There is a spare second channel inside the unit whose dial and display are on the right of the panel (B).

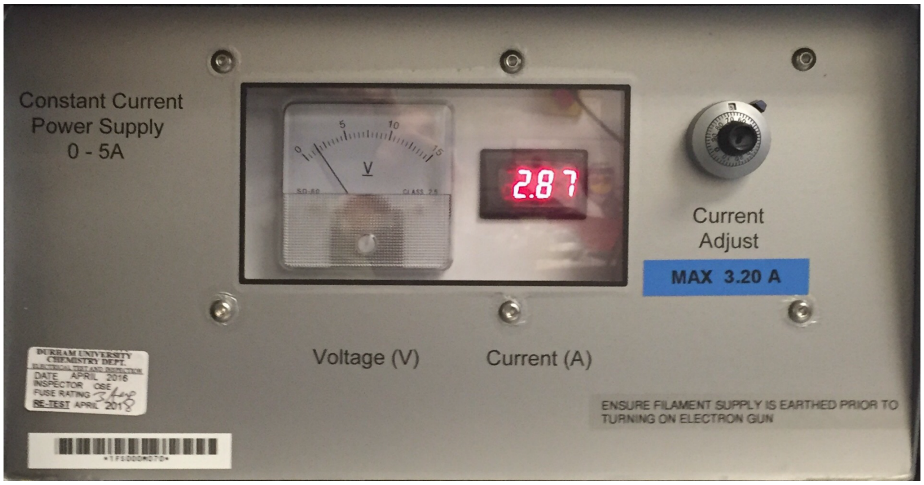

Figure A.10: The front panel of the constant current power supply that controls the current passing through the electron gun filament. This power supply floats on top of the filament voltage supplied by the main electron gun rack unit. The recommended operating level of this supply is detailed in Table A.5. This rack unit receives its power from the Interlock, ensuring that current cannot flow through the filament if the pressure in the Source chamber is above its set-point.

Table A.5: The ratings and recommended operating levels of each of the power supplies inside the electron gun control units. The operational voltage of the deflectors can be changed in order to aim the electron beam directly towards the supersonic expansion emerging from the Even-Lavie valve. Each deflector pair is controlled by a single dial that delivers an equal but oppositely polarised voltage to opposing elements.

Power supply	**Manufacturer**	**Part number**	**Voltage rating**	**Operating level**	**Reference**	**Current rating**
filament	Spellman	MS0.5N	− 500 V	− 300 V	0 V	6 mA
Wehnelt	Spellman	MS0.5N	− 500 V	− 40.0 V	filament	6 mA
extractor	Spellman	MS0.3P	+ 300 V	0 V	0 V	10 mA
anode	Applied Kilovolts	KS005PAA300	+ 5.00 kV	+ 2.40 kV	0 V	1 mA
focus	Spellman	MS1.5P	+ 1.50 kV	+ 300 V	0 V	2 mA
deflectors	Analog Devices	AD812	± 5 V	variable	0 V	50 mA
filament current	Analog Devices	AD820	+ 15 V	3.20 A	filament	–

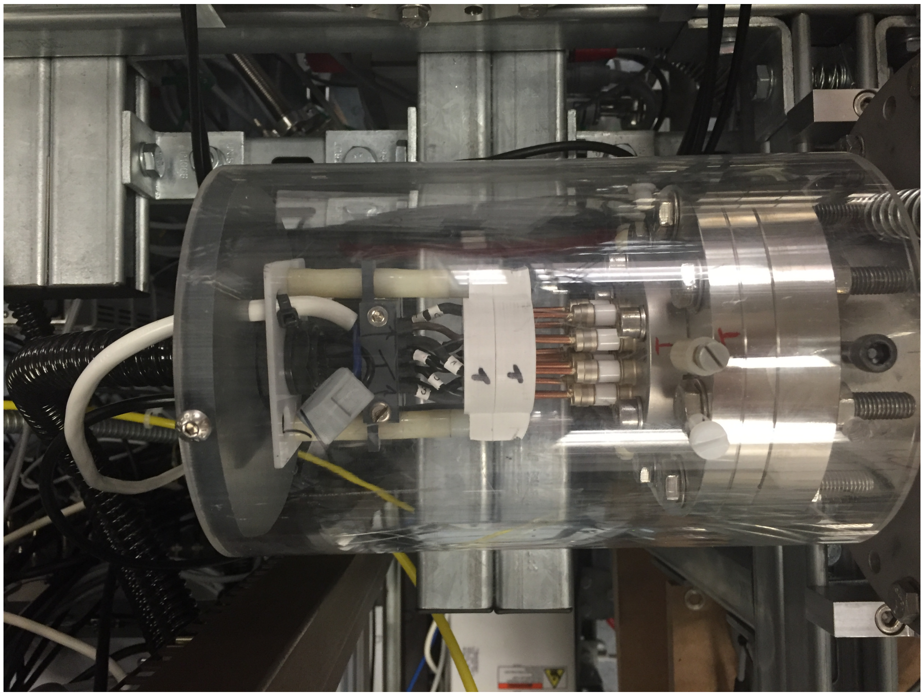

Figure A.11: The LewVac Components Ltd 12-pin feedthrough with associated connections inside its protective perspex tube seen from above. The pin assignments are detailed in Figure A.12.

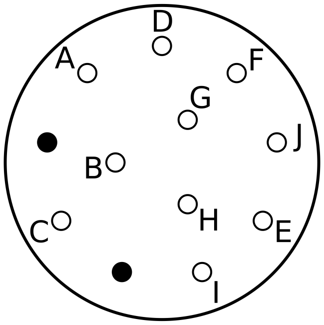

Figure A.12: The pin assignments of the 12-pin HV electrical feedthrough that serves the electron gun. The two black pins are not in use. This perspective represents the arrangement of the pins in the flange viewed from the atmosphere side.
A – Wehnelt; B – filament 1; C – filament 2: D – extractor; E – anode; F – deflector x_1; G – deflector y_1; H – deflector x_2; I – deflector y_2; J – focus.

A.1.6 Ion optics power supply

The power supplies for the einzel lenses, TOF plates and TOF deflectors are all contained in single rack unit, shown in Figure A.13. The function of these components is detailed in Sections 2.1.2.1, 2.1.2.3 and 2.1.2.2. The power supplies are clustered into groups with a single display per group. A silver selector dial adjacent to each display specifies which of the supplies in the cluster is displayed. The ratings of each of the power supplies are detailed in Table A.6. The circuit diagrams for each supply are included in the digital appendix.

Each of the 11 output channels is bipolar but the channels controlling the einzel lenses and TOF plates have toggle switches and separate output ports for each polarity on the back of the unit. As well as the four deflector elements, the six channels in the TOF deflectors cluster also include the channel that supplies the very low voltage to the einzel lens between the Source and TOF chambers and the channel that supplies the static voltage to the extractor plate in the VMI assembly. All of the channels have a toggle switch to select local or external control.

The einzel lenses are optimised for each analyte to transmit the maximum number of ions to the Detection chamber. The first lens collimates the beam emerging from the TOF plates and the second focuses the beam as it enters the Detection chamber.

The deflectors are positioned between the TOF plates and the first einzel lens. The deflector elements are controlled independently by four of the six dials in their cluster. The TOF plates extract the anions orthogonally from the direction of the supersonic expansion. Residual momentum along the original vector is compensated for by the lateral deflector elements that lie in that plane. Due to the uniform velocity of the supersonic expansion, the effect of these deflectors is sensitive to the mass of the analyte, while the vertical deflectors are less so.

The channel powering the low voltage einzel lens positioned between the Source and TOF chambers is connected to a potential divider that reduces the output voltage displayed by a factor of 10. As such, the applied voltage can be controlled by much smaller degrees. This lens affects the velocity of the ions in the supersonic expansion and therefore the relative timings of the Even-Lavie valve and TOF triggers must be adjusted accordingly.

The voltage applied to the extractor plate of the VMI assembly is fixed at −35.0 V in order to maintain VMI focus. This voltage also introduces a permanent deflective field between the VMI repeller and extractor plates that serves to

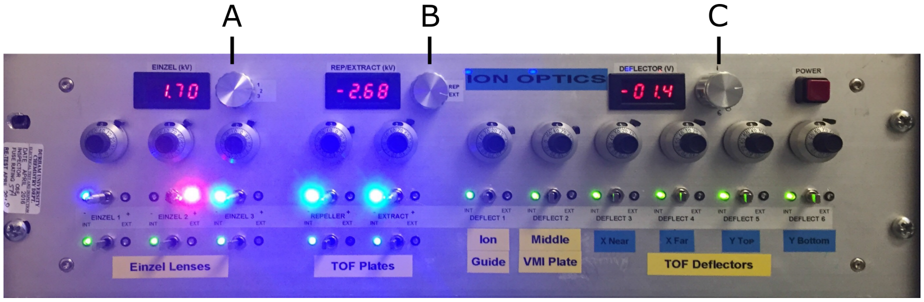

Figure A.13: The front panel of the rack unit that powers the three einzel lenses (A), the two TOF plates (B) and the six TOF deflector channels (C). The silver dial adjacent to each display is a selector for the cluster of channels below it. The ratings of each of the power supplies in the rack unit are detailed in Table A.6.

reduce the number of ions passing up through the VMI assembly and introducing noise on the detector surface.

The voltages applied to the TOF plates are first relayed from the back of the rack unit to a set of fast HV Behlke switches. These switches are mounted inside a steel box, fixed directly to a flange on the side of the TOF chamber, shown on the right in Figure A.14. This switch box also contains the connections for the earthed front TOF plate and for the middle element of the first einzel lens. The circuit diagram of the contents of this box are included in the digital appendix. The assignment of the four safe high voltage (SHV) connections that relay the voltages into the chamber is shown in Figure A.15.

The cables connected to the TOF deflectors, the earthed elements of the TOF einzel lens and the low voltage einzel lens are bundled in grey conduit and passed into the TOF chamber through an MDC Vacuum Products LLC 10-pin 700 V feedthrough, shown on the left in Figure A.14. The pin assignments are shown in Figure A.16.

The voltages applied to the second einzel lens and the VMI extractor plate are bundled in grey conduit and fed into the Detection chamber through an MDC Vacuum Products LLC 7-pin 12 kV feedthrough below the central axis in the terminal flange, as shown in Figure A.18. The pin assignments are detailed in Figure A.17.

Table A.6: The ratings and recommended operating levels of each of the power supplies inside the ion optics rack unit. All voltages are referenced to 0 V and all supplies are manufactured by Applied Kilovolts Ltd.
* The first einzel lens, positioned just after the TOF plates, typically operates at – 1 kV. The second einzel lens, positioned just inside the Detection chamber, typically operates at + 2 kV.
** The lateral deflectors are mass-sensitive and typically operate at around ±50 V. The vertical deflectors operate at lower voltages, typically ±10 V and are less mass-sensitive. The channel powering the low-voltage einzel lens between the Source and TOF chambers typically operates between – 2 and – 5 V. The channel powering the VMI extractor plate remains static at – 35.0 V.

Power supply	**Part number**	**Voltage rating**	**Operating level**	**Current rating**
einzel lenses	KS010[P/N]AA300	±5.0 kV	variable*	0.5 mA
TOF plates	HP010[P/N]AA025	±5.0 kV	– 3.0 kV & – 2.7 kV	1.0 mA
TOF deflectors	MS0.2MZZ065	±200 V	variable**	100 µA

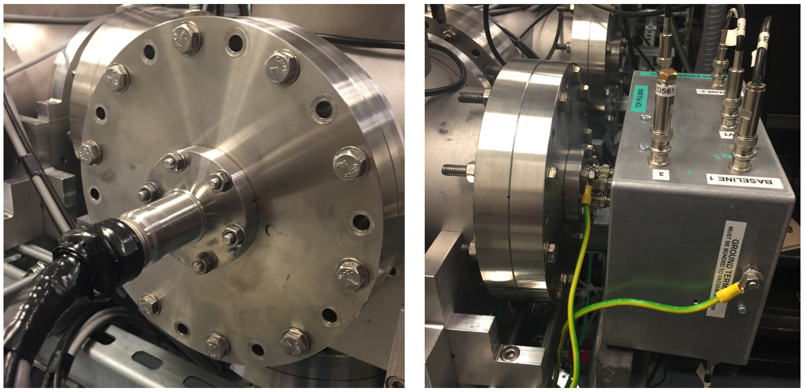

Figure A.14: The flanges on the TOF chamber that host the electrical feedthroughs. On the left is the terminal flange and the 10-pin feedthrough. On the right is the steel box in which the Behlke HV switches are mounted and the four corresponding SHV connectors.

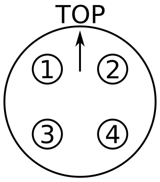

Figure A.15: The assignments of the SHV connections in the side flange of the TOF chamber to which the steel Behlke switch box is attached, shown on the right in Figure A.14. This perspective represents the arrangement of the SHV ports in the flange viewed from the atmosphere side.
1 – TOF repeller plate
2 – TOF extractor plate
3 – TOF front plate
4 – HV einzel lens middle element

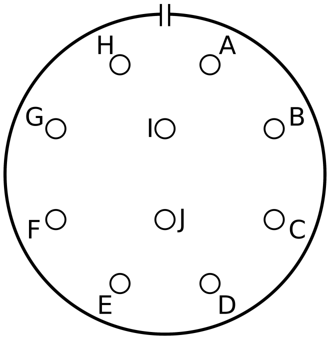

Figure A.16: The pin assignments of the 10-pin electrical feedthrough in the terminal flange of the TOF chamber, shown on the left in Figure A.14. This feedthough hosts connections for most of the ion optics in the TOF chamber. This perspective represents the arrangement of the pins in the flange viewed from the atmosphere side.
A – low voltage einzel lens element 1
B – low voltage einzel lens element 2
C – low voltage einzel lens element 3
D – low voltage einzel lens element 4
E – deflector y_1
F – HV TOF einzel lens element 3
G – HV TOF einzel lens element 1
H – deflector y_2
I – deflector x_1
J – deflector x_2

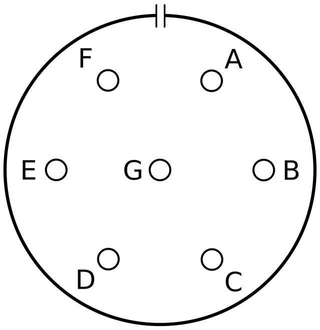

Figure A.17: The pin assignments of the off-axis 7-pin electrical feedthrough in the terminal flange of the Detection chamber. This feedthrough hosts connections for the ion optics in the Detection chamber. This perspective represents the arrangement of the pins in the flange viewed from the atmosphere side.
A – second einzel lens element 2
B – front plate of VMI optics and VMI drift tube
C – second einzel lens element 1
D – no connection
E – detector einzel lens element 3
F – middle plate of VMI optics
G – earth shielding for wire connected to B in the chamber

A.1.7 Time-of-flight detector power supply

The TOF power supply provides voltages for each of the elements shown in Figure 2.6. The function of the detector is detailed in Section 2.1.3. The rack unit, shown in Figure A.19 contains four power supplies, setting voltages for the MCP bias, MCP out, scintillator and PMT elements. The rating and recommended operational voltages of these elements is detailed in Table A.7. This rack unit receives its power from the Interlock, ensuring that the detector cannot be turned on if the pressure in the chamber is above its set-point. The circuit diagrams for these power supplies are detailed in the digital appendix.

The cables relaying these voltages to the instrument are contained within black braided conduit and enter the Detection chamber through an MDC Vacuum Products LLC 7-pin 12 kV feedthrough. This feedthrough is on the terminal flange of the Detection chamber, mounted along the central axis. The pin assignments are detailed in Figure A.20. The TOF signal from the detector is fed through an individual SHV connector to the right of the multi-pin feedthrough.

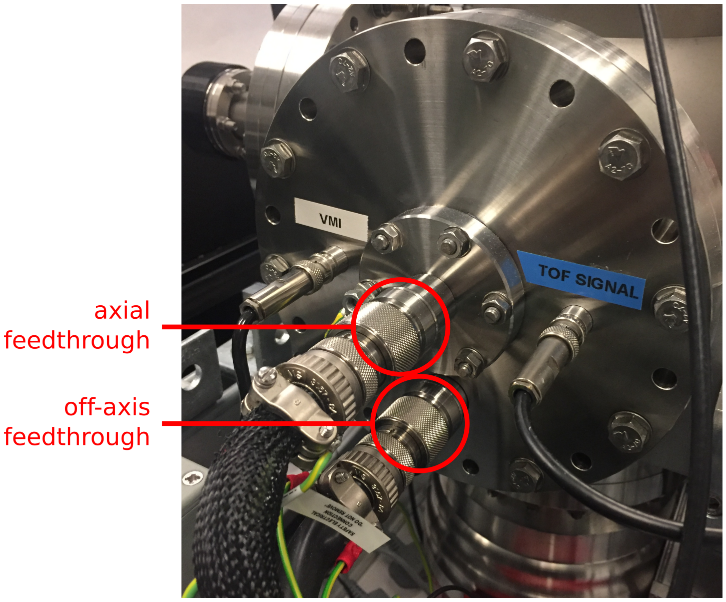

Figure A.18: The terminal flange of the Detection chamber. The axial and off-axis feedthroughs are indicated. The SHV port that relays the HV pulse to the repeller plate of the VMI is on the left. The SHV port that relays the signal from the TOF detector is on the right.

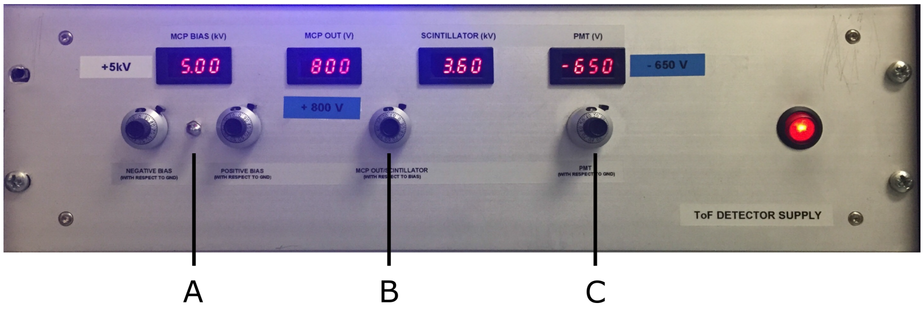

Figure A.19: The front panel of the rack unit that powers the TOF detector. The MCP bias (A) accelerates the ions toward the MCP. This supply is bipolar and can be switched using the toggle switch between the two dials. The MCP out (B) determines the amplification of the signal through the MCP. The scintillator voltage rises at a fixed ratio with the MCP out. The PMT voltage (C) determines the amplification of the signal through the PMT.

Table A.7: The ratings of each of the power supplies inside the TOF detector rack unit. All power supplies within the rack are manufactured by Applied Kilovolts Ltd. The MCP bias voltage is reversible and can be operated at a positive polarity in order to detect anions or a negative polarity for cations.

Power supply	Part number	Voltage rating	Operating level	Reference	Current rating
MCP bias	KS010(P/N)AA300	±10.0 kV	+ 5.0 kV	0 V	0.5 mA
MCP out	HFD005PAA010	+ 1.25 kV	+ 800 V	MCP bias	100 µA
scintillator	HFD005PAA010	+ 4.75 kV	+ 3.6 kV	MCP bias	100 µA
PMT	MP001N	– 1.0 kV	– 700 V	0 V	2.0 mA

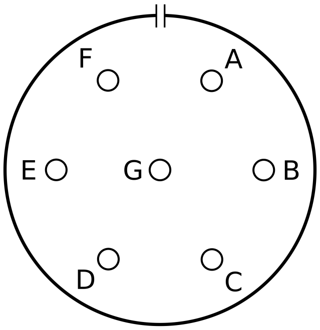

Figure A.20: The pin assignments of the axial 7-pin electrical feedthrough in the terminal flange of the Detection chamber. This feedthrough hosts connections for the various elements of the TOF detector. This perspective represents the arrangement of the pins in the flange viewed from the atmosphere side.
A – no connection
B – PMT voltage
C – no connection
D – MCP bias
E – scintillator voltage
F – MCP out
G – 0 V earthing shield

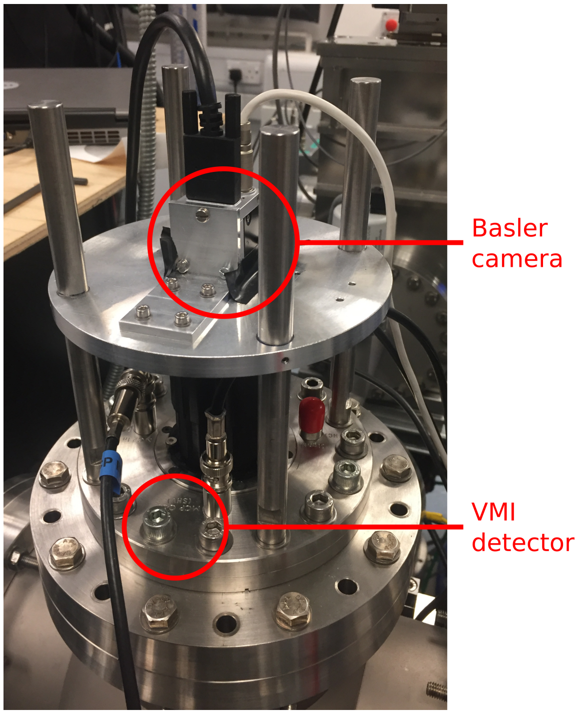

Figure A.21: The VMI detector is attached to the top flange of the Detection chamber. The Basler CCD camera is suspended directly above it, recording images of the electron strikes that manifest as flashes on the phosphor screen inside the vacuum chamber. A 3D printed PLA tube excludes ambient light from the space between the camera and the detector.

A.1.8 Velocity-map imaging power supply

The VMI power supply rack unit provides the voltages for both the VMI electrostatic optics and the VMI detector. The front panel of the rack unit is shown in Figure A.22. The technique of VMI is detailed in Section 2.1.2.4 and the function of the detector is described in Section 2.1.3 and Figure 2.6. The detector consists of a chevron MCP stack and P43 phosphor scintillator. Unlike the TOF detector, there is no PMT behind the scintillator but instead a camera external to the chamber, shown in Figure A.21, records the position of each electron strike.

The ratings and recommended operating levels of each of the power supplies in the rack unit are detailed in Table A.8. There is a connection on the detector flange, labelled *Inter* that allows for direct control of the voltage applied to the two MCP surfaces in the middle of the chevron but this connection is normally

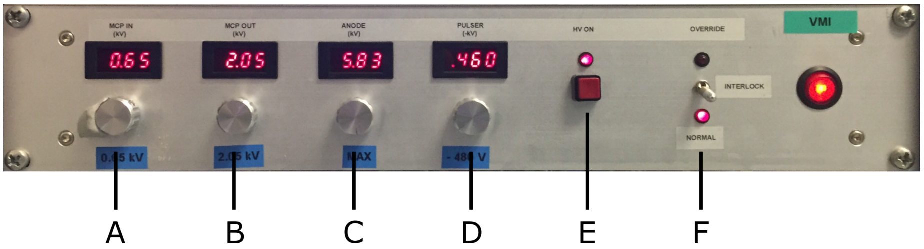

Figure A.22: The front panel of the VMI rack unit. A – MCP In is applied to both the front face of the front MCP and the topmost plate of the VMI electrostatic optics, which is also connected to the drift tube between the VMI plates and the detector. B – MCP Out voltage is applied to the rear face of the back MCP. C – Scintillator voltage is applied to the glass substrate onto which the phosphor is coated. D – Pulser voltage is applied to the repeller plate of the VMI optics the moment the analyte occupies the interaction volume. E – HV On switch enables the output from all channels. This will be off when the rack unit is first turned on but once pressed, cannot be turned off again until the unit is powered down. The accompanying LED indicates the outputs are live. F – Interlock override toggle switch. The interlock should only be overridden when the unit is being tested on the bench.

left to float without connection. This rack unit receives its power from the Interlock, ensuring that the detector cannot be turned on if the pressure in the chamber is above its set-point.

Individual SHV cables relay the voltages from the rack unit to the instrument. The flange onto which the VMI detector is mounted contains 4 SHV ports for the MCP In, MCP Out, Inter (unused) and Scintillator connections. There is also an unused bayonet Neill-Concelman (BNC) port for monitoring the time of arrival of the photoelectrons. An SHV tee-piece on the MCP In connector relays the same voltage to a pin in the off-axis multipin feedthrough mounted on the terminal flange of the Detection chamber, shown in Figure A.17. This pin is connected to the front plate of the VMI optics and the drift tube, providing a field-free drift region between the VMI optics and the VMI detector while ensuring they are not mechanically joined inside the chamber.

The Pulser voltage is delivered to a DEI PVM-1001-N pulsed HV module, shown in Figure A.23, via a capacitor bank. Refer to the user manual for detailed instructions on how to use this unit. The output from the pulser module is passed through a 68 Ω resistor capable of preserving the square profile of high energy fast pulses. The HV side of this resistor is fed into the chamber and to the VMI repeller plate through an individual SHV port in the terminal flange of the Detection chamber, just to the left of the axial multi-pin feedthrough.

Table A.8: The ratings and recommended operating levels of the power supplies in the VMI rack unit. The base voltages of the MCP Out and Scintillator supplies are configured such that a negative potential cannot be generated between successive elements. Each of the power supplies are manufactured by Applied Kilovolts Ltd and all of the voltages on the displays are measured with respect to 0 V.

Power supply	**Part number**	**Voltage rating**	**Operating level**	**Base voltage**	**Current rating**
MCP In	KS010PAA300	+ 10.0 kV	+ 650 V	0 V	0.5 mA
MCP Out	KS010PAA300	+ 10.0 kV	+ 2.05 kV	MCP In	0.5 mA
Scintillator	KS010PAA300	+ 10.0 kV	+ 5.8 kV	MCP Out	0.5 mA
Pulser	HP001NAA025	− 1.0 kV	− 480 V	0 V	10.0 mA

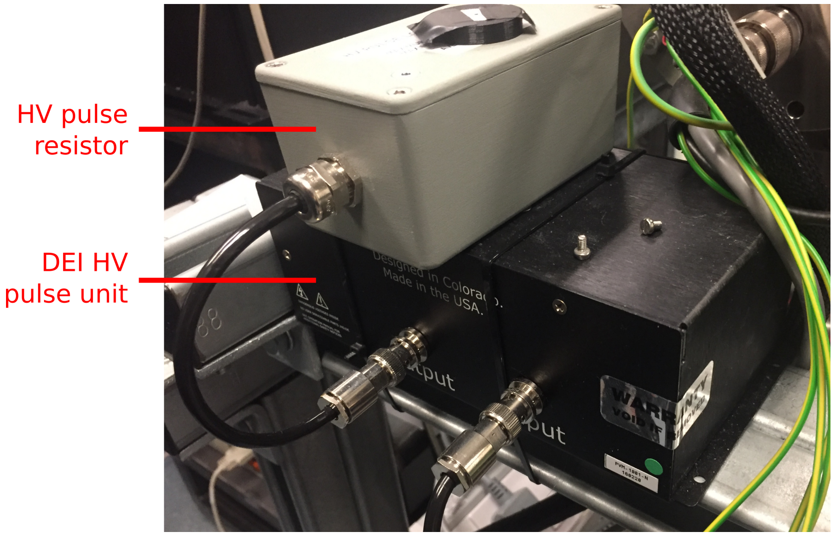

Figure A.23: The DEI pulsed HV module and accompanying HV pulse resistor that sit on the framework of the instrument beside the terminal flange of the Detection chamber.

A.2 Laser and optical setup

Two laser systems on the optical bench adjacent to the instrument provide the pulses of light necessary for PES. The optical bench is laid out differently depending on the laser pulse input. These layouts are shown in Figures A.24 and A.26.

A.2.1 Tuneable nanosecond optical parametric oscillator

The Continuum® Horizon™ I is a tuneable OPO capable of producing laser pulses anywhere in the range $192 \leq \lambda \leq 2750$ nm. In this particular setup, the OPO is pumped by a Continuum® Surelite™ SL II-10 Q-switched Nd:YAG laser operating at 10 Hz and providing 1064 nm and 355 nm pulses of ~ 5 ns duration. The water-cooled flashlamp in the Surelite laser pumps the population inversion in the gain medium. After the flashlamp is switched off, the light intensity within the cavity begins to decay. The Q-switch triggers the release of the light from the cavity. The relative timings of the flashlamp and the Q-switch, as described in Table A.1, determine the intensity of the beam. A shorter delay results in a higher beam power as the light intensity in the cavity does not decay for long before it is released.

The Horizon™ I passes the 355 nm pulses through two consecutive β-barium borate (BBO) crystals at variable angles optimised by stepper motors in order to generate the desired wavelength. In order to generate UV light, the light emerging from the BBO crystals are mixed with 1064 nm pulses from the Surelite pump laser in a second pair of BBO crystals. Refer to the manual for further details and operating instructions.

The tuneable nanosecond OPO has two output ports, one for $192 < \lambda < 400$ nm and one for $400 < \lambda < 2750$ nm. Given that all of the optics shown in Figure A.24 are required to transmit light in the UV range, each element is made of either fused silica or CaF_2. In order to ease switch-over, a pair of prisms are fixed on a magnetic mount and can be transferred between two bases positioned in front of each port. These prisms are coupled together into a periscope inside a bespoke 3D printed PLA case, shown in Figure A.25. This serves to lower the beam path by ~ 20 mm in order to match the height of the instrument laser axis. The periscope also redirects the beam orthogonal to its original path and in so doing rotates the beam profile and polarisation by 90°.

The other function of the periscope is to correct for an artefact in the beam profile of the OPO output pulses. It was noted during experiments that certain

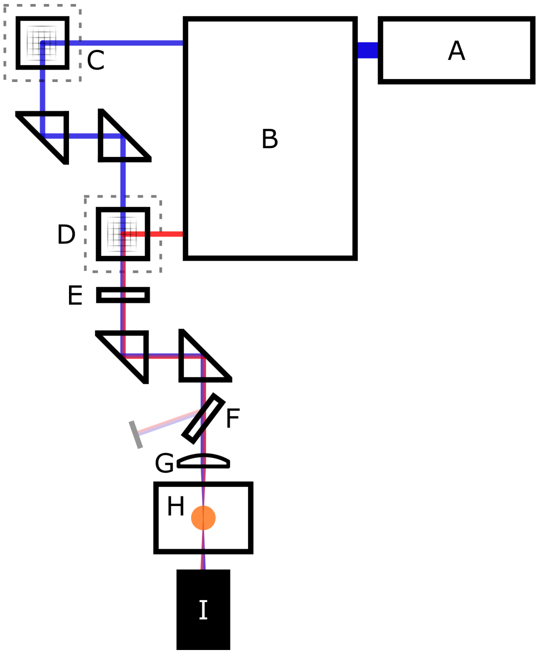

Figure A.24: An overview of the nanosecond OPO laser and the optics that deliver the pulses to the analyte in the instrument.

A – the Continuum® Surelite™ SL II-10 Q-switched Nd:YAG laser produces 1064 nm light, doubles and triples it, resulting in 532 nm and 355 nm light.

B – the tuneable Continuum® Horizon™ I OPO, pumped by the 355 nm and 1064 nm light from the Surelite™ pump laser. The OPO laser has two output ports, one for $192 < \lambda < 400$ nm and one for $400 < \lambda < 2750$ nm.

C & D – a periscope consisting of two fused silica right-angle prisms mounted in a 3D printed PLA case (shown in Figure A.25) can be moved between magnetic bases indicated by the dashed boxes positioned in front of each of the output ports of the OPO.

E – an Alphalas GmbH tuneable zero-order $\lambda/2$ phase retardation plate rotates the polarisation of the light by 90°.

F – a 1 mm thick CaF_2 window mounted at Brewster's angle (57°) provides a means to measure the rotation of the polarisation by the waveplate. The reflection is monitored on a piece of card and at its lowest intensity, the waveplate is optimised.

G – an optional plano-convex lens with a focal length of 600 mm. The lens provides the ability to increase the power density of the laser and improve the photoelectron signal level.

H – the beam passes through either a 3 mm thick CaF_2 window mounted at Brewster's angle or a 1 mm thick CaF_2 window mounted normal to the beam axis on the side of the Detection chamber, at the centre of which it interacts with the analyte.

I – the beam dump on the far side of the Detection chamber.

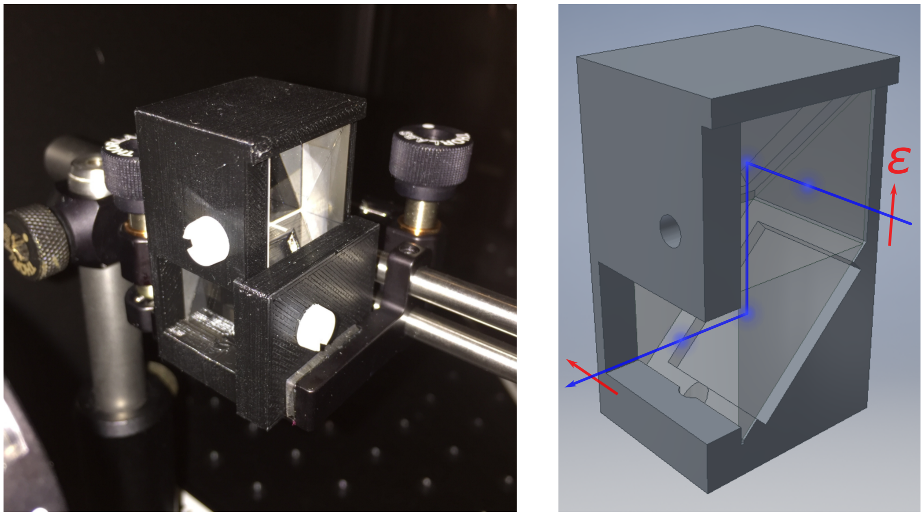

Figure A.25: The periscope consisting of two fused silica prisms mounted in a bespoke 3D printed PLA case. The laser pulse, indicated by the blue line, enters the upper prism and is translated downwards by ~ 20 mm, emerging from the lower prism perpendicular to the original beam path and rotated by 90°. The polarisation of the light, indicated by the red arrow, is also rotated by 90°.

features in the photoelectron spectra appeared and disappeared with regularity during continuous frequency scans. Upon further investigation, it was noted that the beam profile changes as a function of wavelength owing to the discreet action of the stepper motors adjusting the angle of the crystals and prisms within the OPO. The position of the most intense portion of the beam wanders back and forth along the horizontal axis, causing a concomitant variation in the photoelectron flux from multi- and multiple-photon processes.

Given that the laser pulse addresses the mass packets perpendicular to their direction of travel inside the Detection chamber, variation in laser intensity along the horizontal axis corresponds to variation in the TOF time-domain. In order to minimise the possibility of inadvertently addressing a mass packet adjacent to the analyte in the TOF spectrum, the periscope also rotates the image of the beam axially by 90° such that any variation in the beam profile occurs 'harmlessly' along the vertical axis.

However, in rotating the beam profile, the polarisation of the light is also rotated, as shown by the red arrows in Figure A.25. The polarisation of the laser relative to the VMI axis is crucial in order to measure the PAD and extract the corresponding information. In order to rotate the polarisation back by 90° while maintaining the rotated profile, an Alphalas GmbH tuneable zero-order

$\lambda/2$ phase retardation plate (PO-TWP-L2-25-UVIR, F in Figure A.24) is positioned after the periscope. This uncoated 2.5 mm thick waveplate is mounted in a tilt-turn rotation holder and can be optimised to any wavelength of light in the range $150 < \lambda \pm 5\% < 6000$ nm, which more than covers the spectral output of the OPO. The optimisation of this waveplate is achieved by monitoring the intensity of the reflection from a thin window placed in the beam path mounted at Brewster's angle.

A.2.2 Femtosecond pump-probe

In order to measure the dynamics of molecules and clusters, it is necessary to probe them on a time-scale concordant with electronic transitions and nuclear motion. A femtosecond laser generates pulses short enough to achieve this.

A layout of the femtosecond laser system used in this experiment is shown in Figure A.26. The femtosecond pulses are initially generated in the Newport Spectra Physics Tsunami mode-locked Ti:sapphire laser (B). The crystal in this laser is pumped by 532 nm continuous wave (CW) light from the Newport Spectra Physics Millenia Pro laser (A). The Tsunami generates low intensity 800 nm femtosecond pulses at 76 MHz, which contain the seed pulses delivered to the Newport Spectra Physics Spitfire ultrafast amplifier (D) for amplification. Simultaneously, the Spitfire amplifier is pumped at 950 Hz by 527 nm light from a Newport Spectra Physics Empower Nd:YLF laser (C). The seed pulses from the Tsunami are amplified in the Spitfire when they coincide with the population inversion in its Ti:sapphire crystal generated by the Empower pump laser. The output of the Spitfire is therefore ~ 200 µJ 800 nm femtosecond pulses at a repetition rate of 950 hertz.

The beam emerging from the Spitfire is telescoped (E) to increase the power density and then split (F) in order to generate two different colour pulses. In this experiment this is achieved by passing one beam through a BBO crystal (H). The two pulses are then recombined along a common beam path in order to ensure that both address the analyte in the Detection chamber (J) from the same direction. However, while separated, a variable increase in path length is applied to one beam in order to introduce a controllable discrepancy in the time of arrival between the two pulses. This is achieved with a retroreflector mounted on a Physik Instrumente Ltd delay stage (G).

Given the short duration of the laser pulses, dispersion must be considered in the design of the optical bench. The total beam path and particularly any passage through solid materials with a high refractive index must be minimised in order to maintain the short pulse duration. Therefore, unlike the optical setup for the nanosecond OPO, which uses right angle prisms to direct the beam, the femtosecond setup employs exclusively of metallic mirrors. Where UV light is incident, the mirror of choice is UV enhanced aluminium. Otherwise, protected aluminium or silver mirrors are sufficient. The convolution of two Gaussian functions with variances σ^2 is also a Gaussian with variance $2\sigma^2$. The cross-correlation of the two laser pulses yields a Gaussian profile with FWHM = 70 fs, which corresponds to a FWHM = 50 fs for each individual femtosecond pulse.

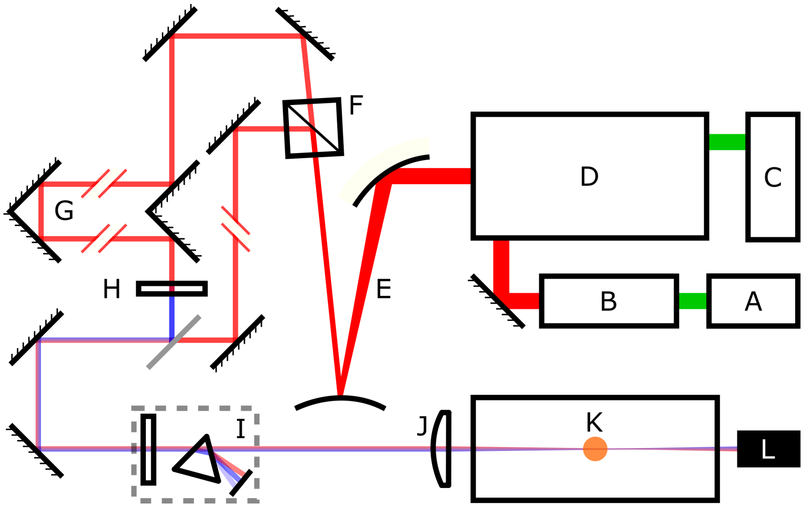

Figure A.26: An overview of the femtosecond pump-probe laser system and the optics that deliver the pulses to the analyte in the instrument.

A – Newport Spectra Physics Millenia Pro s-Series diode-pumped, CW visible laser system (0000-320A, Rev. B) produces 532 nm light.

B – Newport Spectra Physics Tsunami mode-locked Ti:sapphire laser (0000-232A, Rev. D) is pumped by the Millenia Pro and produces low-power femtosecond pulses of 800 nm light at 76 MHz.

C – Newport Spectra Physics Empower intracavity-doubled, diode-pumped Nd:YLF laser (0000-334A, Rev. B) produces 527 nm light pulses at 950 Hz with a pulse duration in the order of hundreds of nanoseconds.

D – Newport Spectra Physics Spitfire ultrafast amplifier (0000-277A, Rev. G) is pumped by the Empower laser and amplifies and compresses the femtosecond pulses provided by the Tsunami. The output is ~ 200 µJ femtosecond pulses of 800 nm light at 950 Hz.

E – the combination of a concave mirror followed by a convex mirror serves as a telescope in order to reduce the beam diameter and increase the power density.

F – a beamsplitter separates out a portion of the beam to generate a different wavelength.

G – a 150 mm Physik Instrumente GmbH delay stage provides a means to lengthen the beam path for one portion of the beam relative to the other. This in turn generates a time-delay between the arrival of two femtosecond laser pulses.

H – a BBO crystal generates 400 nm light, the second harmonic of the 800 nm pulses. The two beam paths are then recombined by a longpass dichroic mirror.

I – in order to find t_0, where the two pulses are temporally overlapped, the beams are passed through a BBO crystal. If they arrive at the same time, their frequencies are mixed and 266 nm light is generated. A prism disperses the different colours in the beam onto a piece of card and the delay stage is moved incrementally until the spot corresponding to the 266 nm light is at its brightest. The BBO crystal and prism are removable, as indicated by the dashed box around them.

J – an optional plano-convex lens with a focal length of 600 mm. The lens provides the ability to increase the power density of the laser and improve the photoelectron signal level.

K – the beam passes through a 1 mm thick CaF_2 window mounted normal to the beam axis on the side of the Detection chamber, at the centre of which it interacts with the analyte.

L – the beam dump on the far side of the Detection chamber.

A.3 Software

The software used to gather and analyse data from the instrument, as well as view and control certain parameters of its operation, was written in a collection of virtual instruments (VIs) in the National Instruments LabVIEW package. The principal device from which data is gathered is the Basler CCD camera monitoring the position-sensitive VMI detector atop the Detection chamber. This is connected to the experiment computer via USB 3.0 interface and the images it acquires are passed into the LabVIEW scripts.

Other devices attached to the instrument are also interfaced with the experiment computer. The Pfeiffer MaxiGauge, the Quantum Composers delay generator, the Horizon™ I OPO and the ISO-TECH IDS-3354 oscilloscope are also able to communicate with LabVIEW. Refer to the digital appendix for working LabVIEW VIs.

A.3.1 Frequency-resolved measurements

The VI written to perform frequency-resolved measurements contains functions for the following tasks:

- establish the parameters of the study and create a list of laser wavelengths at which to acquire data
- initialise a port connection with the OPO control software
- initialise a port connection with the camera and establish acquisition attributes
- acquire images from the camera for a fixed number of frames or until instructed and apply a threshold to isolate signal from noise
- sum the acquired frames together into a cumulative image
- save the cumulative image to a specified directory
- pass the cumulative image to the POP 8.5 sub-VI to generate a photoelectron spectrum
- reinitialise the cumulative image
- automatically move the laser to the next wavelength in the scan and wait for confirmation that the appropriate optics are installed in the OPO and that the waveplate has been optimised

An image of the dialogue box that appears when the VI is run is shown in Figure A.27 and the front-panel of the VI is shown in Figure A.28.

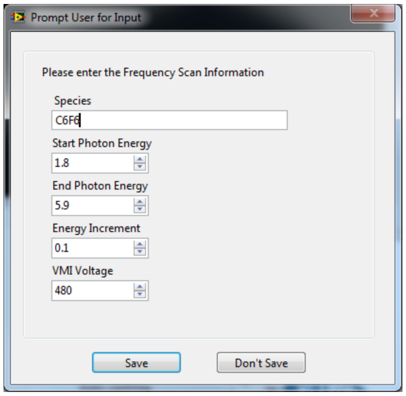

Please enter the Frequency Scan Information

Species: C6F6
Start Photon Energy: 1.8
End Photon Energy: 5.9
Energy Increment: 0.1
VMI Voltage: 480

Figure A.27: The dialogue box that appears when the frequency-resolved data acquisition VI is run. It allows the user to tell the software the subject of the study, the VMI conditions and establish the frequency scan sequence, which can be entered in units of eV or nm. All this information is incorporated into the name of the folders in which the data are saved.

A.3.2 Time-resolved measurements

The VI written to perform time-resolved measurements contains many of the same functions as the VI that controls the frequency-resolved measurements:

- establish the parameters of the study and create a list of time delays at which to acquire data
- initialise a port connection with the delay stage and allow the operator to find t_0
- initialise a port connection with the camera and establish acquisition attributes
- acquire images from the camera for a fixed number of frames or until instructed and apply a threshold to isolate signal from noise
- sum the acquired frames together into a cumulative image
- save the cumulative image to a specified directory
- pass the cumulative image to the POP 8.5 sub-VI to generate a photoelectron spectrum
- reinitialise the cumulative image
- automatically move the retroreflector on the delay stage to the next step in the scan

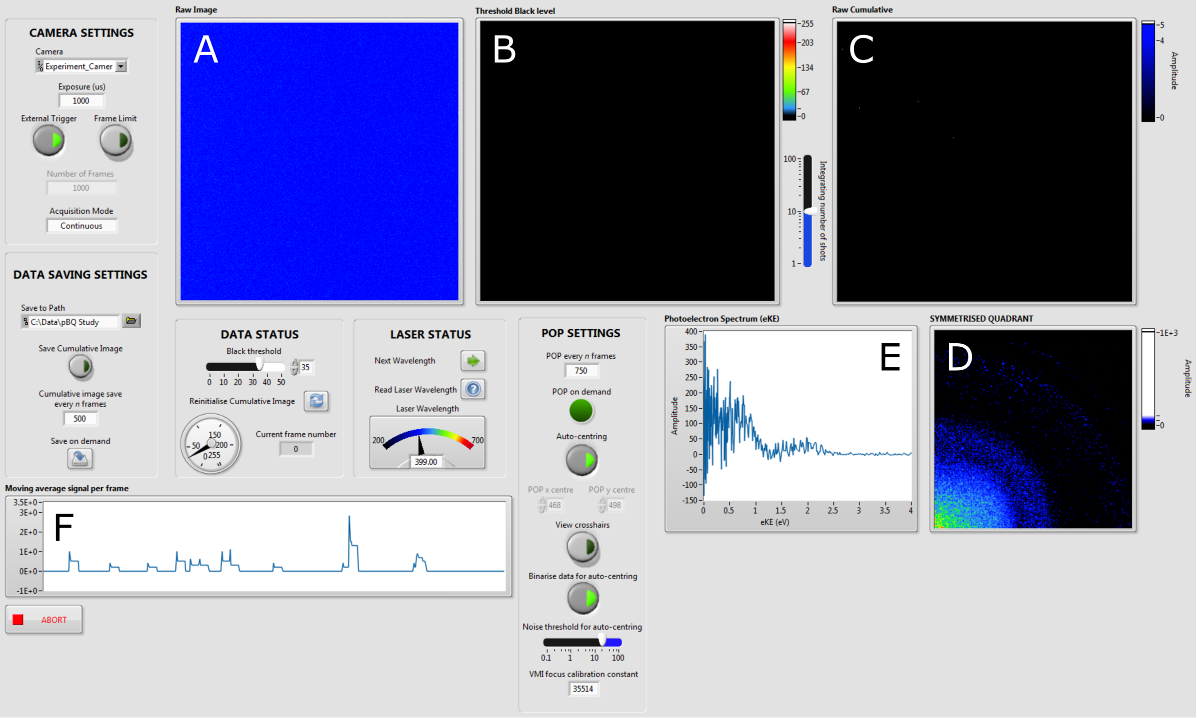

CAMERA SETTINGS

Camera: Experiment_Camer

Exposure (us): 1000

Number of Frames: 1000

Acquisition Mode: Continuous

DATA SAVING SETTINGS

Save to Path: C:\Data\pBQ Study

Cumulative image save every *n* frames: 500

DATA STATUS

Black threshold: 35

Current frame number: 0

LASER STATUS

Laser Wavelength: 399.00

POP SETTINGS

POP every *n* frames: 750

POP x centre: 468

POP y centre: 498

VMI focus calibration constant: 35514

Figure A.28: The front panel of the VI used to acquire frequency-resolved photoelectron spectra.
The *CAMERA SETTINGS* allow the user to: select the serial port to which the camera is connected; set an exposure time for each frame; determine whether the camera is externally or internally triggered; and determine whether an automatic limit is applied and the number of frames acquired per wavelength.
The *DATA SAVING SETTINGS* allow the user to: choose whether and where the data are saved; determine the frequency at which they are saved; and to save 'on demand'.
The *DATA STATUS* panel allows the user to: set the pixel intensity background threshold that distinguishes signal from noise; monitor the intensity of the most intense pixel in the image in order to prevent saturation of the camera; reinitialise the cumulative image; and monitor the current frame number.
The *LASER STATUS* panel allow the user to: change and monitor the current wavelength at which the nanosecond OPO is operating; query the laser to update the display in case the wavelength was changed outside of the LabVIEW interface; and move to the next wavelength in the scan sequence.
The *POP SETTINGS* allow the user to: change the frequency at which the cumulative image is analysed by the POP 8.5 algorithm; perform analysis 'on demand'; toggle the display of the crosshairs on the cumulative image that indicate the centre of the velocity-map; control whether the centre of the image is determined manually or automatically; and change the calibration constant ($\frac{1}{k}$) that maps the pixel number to an energy value.
The various plots display the following information:
A – the raw data acquired from the camera is an 8-bit monochrome image and is displayed here in a high-contrast format.
B – the pixel intensity background threshold is applied to the raw image and the result is displayed here. Each image has a lifetime on this plot determined by the slider to the right of the display.
C – the cumulative image overlays each image with all of the previous images in order to generate a heat map. This image is reinitialised when the camera exposure time or the laser wavelength is changed. It can also be reinitialised 'on demand'.
D – the cumulative image is folded into a symmetrised quadrant around the centre of the velocity-map.
E – the photoelectron spectrum produced by the POP 8.5 analysis of the symmetrised quadrant.
F – the signal level is monitored as a moving average of the sum of all the pixel intensities in the background-subtracted images.

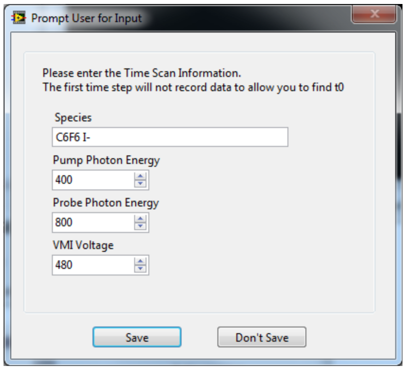

Prompt User for Input

Please enter the Time Scan Information.
The first time step will not record data to allow you to find t0

Species: C6F6 I-
Pump Photon Energy: 400
Probe Photon Energy: 800
VMI Voltage: 480

Figure A.29: The dialogue box that appears when the time-resolved data acquisition VI is run. It allows the user to tell the software the subject of the study, the VMI conditions and the pump and probe pulse colours, which can be entered in units of eV or nm. All this information is incorporated into the name of the folders in which the data are saved.

An image of the dialogue box that appears when the VI is run is shown in Figure A.29 and the front-panel of the VI can be seen in Figure A.30.

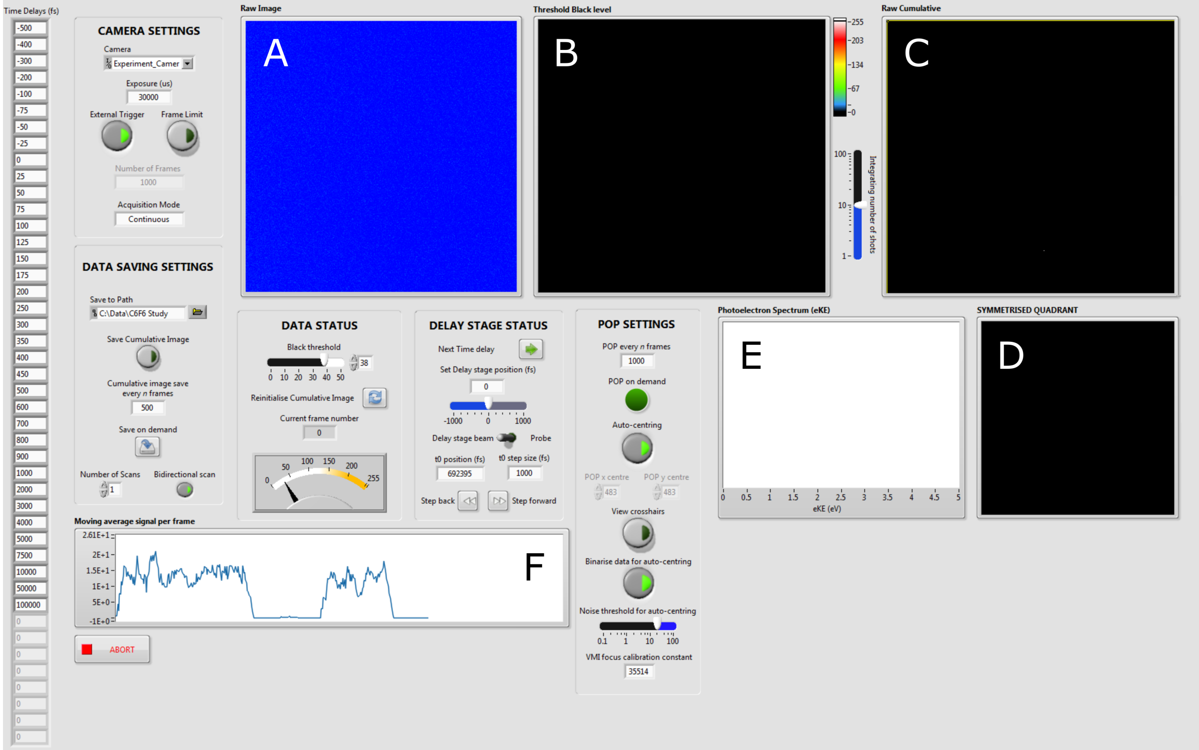

Camera: Experiment_Camer
Exposure (us): 30000
External Trigger
Frame Limit
Number of Frames: 1000
Acquisition Mode: Continuous

Save to Path: C:\Data\C6F6 Study
Save Cumulative Image
Cumulative image save every *n* frames: 500
Save on demand
Number of Scans: 1
Bidirectional scan

Black threshold: 38
Current frame number: 0

Set Delay stage position (fs): 0
Delay stage beam: Probe
t0 position (fs): 692395
t0 step size (fs): 1000

POP every *n* frames: 1000
Auto-centring
POP x centre: 483
POP y centre: 483
Binarise data for auto-centring
Noise threshold for auto-centring
VMI focus calibration constant: 35514

Figure A.30: The front panel of the VI used to acquire time-resolved photoelectron spectra.
The *TIME DELAYS* array specifies the scan sequence that the delay stage will follow. Any changes to the array after the VI has started will not take effect.
The *CAMERA SETTINGS* allow the user to: select the serial port to which the camera is connected; set an exposure time for each frame; determine whether the camera is externally or internally triggered; and determine whether an automatic limit is applied and the number of frames acquired per time delay.
The *DATA SAVING SETTINGS* allow the user to: choose whether and where the data are saved; determine the frequency at which they are saved; save 'on demand'; and determine the number and direction of time delay scans to perform.
The *DATA STATUS* panel allows the user to: set the pixel intensity background threshold that distinguishes signal from noise; monitor the intensity of the most intense pixel in the image in order to prevent saturation of the camera; reinitialise the cumulative image; and monitor the current frame number.
The *DELAY STAGE STATUS* panel allows the user to: change and monitor the current delay stage position; change and monitor the position of t_0 on the stage; tell the software which laser pulse is on the delay stage and; move to the next delay stage position in the scan sequence.
The *POP SETTINGS* allow the user to: change the frequency at which the cumulative image is analysed by the POP 8.5 algorithm; perform analysis 'on demand'; toggle the display of the crosshairs on the cumulative image that indicate the centre of the velocity-map; control whether the centre of the image is determined manually or automatically; and change the calibration constant ($\frac{1}{k}$) that maps the pixel number to an energy value.
The various plots display the following information:
A – the raw data acquired from the camera is an 8-bit monochrome image and is displayed here in a high-contrast format.
B – the pixel intensity background threshold is applied to the raw image and the result is displayed here. Each image has a lifetime on this plot determined by the slider to the right of the display.
C – the cumulative image overlays each image with all of the previous images in order to generate a heat map. This image is reinitialised when the camera exposure time or the delay stage position is changed. It can also be reinitialised 'on demand'.
D – the cumulative image is folded into a symmetrised quadrant around the centre of the velocity-map.
E – the photoelectron spectrum produced by the POP 8.5 analysis of the symmetrised quadrant.
F – the signal level is monitored as a moving average of the sum of all the pixel intensities in the background-subtracted images.

A.3.3 Photoelectron flux measurements

The VI written to perform photoelectron flux spectroscopy contains functions for the following tasks:

- initialise a port connection with the OPO control software
- initialise a port connection with the camera and establish acquisition attributes
- continuously acquire images from the camera and apply a threshold to isolate signal from noise
- start a wavelength scan in the OPO control software and plot the photoelectron flux, characterised by the total sum of the pixel intensities in the image, as a function of wavelength
- wait for confirmation at the critical switchover points that the appropriate optics are installed in the OPO

Due to the continuous nature of the scan in this VI, it is impossible to optimise the waveplate for each wavelength and therefore no meaningful photoelectron spectra can be derived. This VI also contains a code that plots as a function of wavelength the proportion of the total photoelectron signal that appears in the central region of the image where eKE ~ 0 eV. This is of interest when looking for resonance dynamics that lead to thermionic emission or delayed autodetachment. An image of the front-panel of the VI can be seen in Figure A.31.

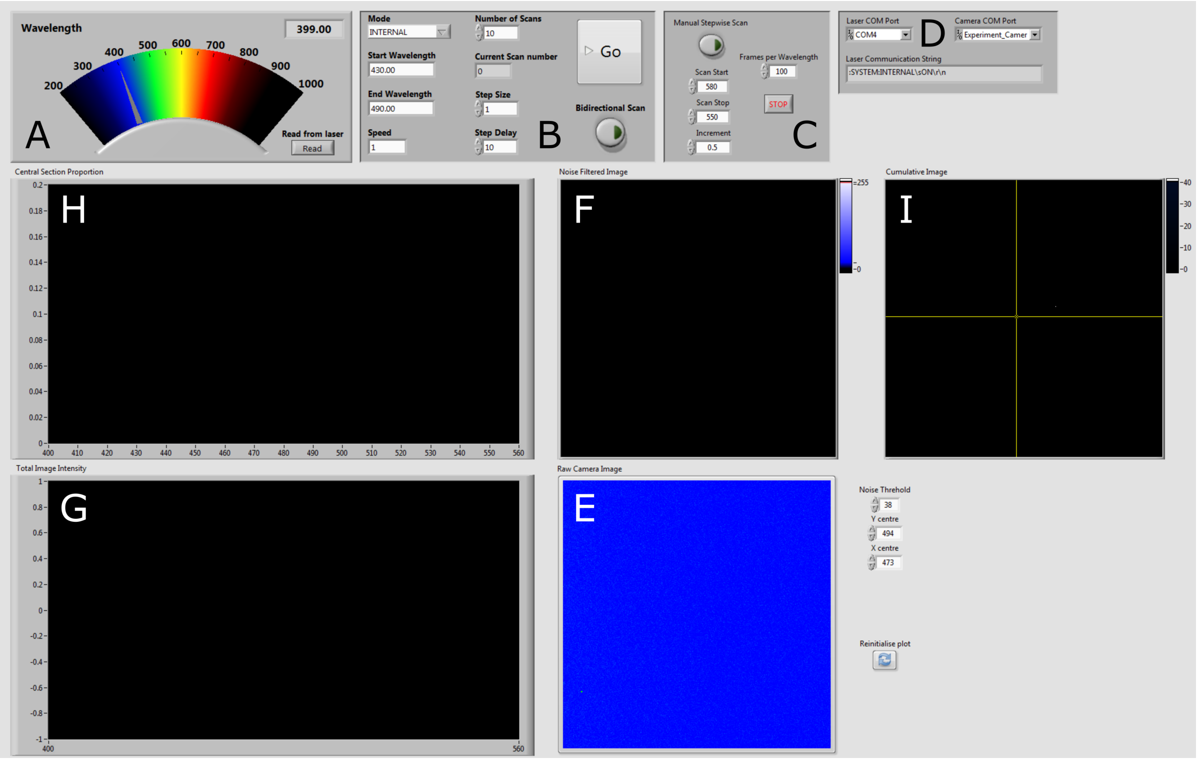

Wavelength 399.00
Mode INTERNAL
Number of Scans 10
Start Wavelength 430.00
Current Scan number 0
End Wavelength 490.00
Step Size 1
Speed 1
Step Delay 10
Frames per Wavelength 100
Scan Start 580
Scan Stop 550
Increment 0.5
Laser COM Port COM4
Camera COM Port Experiment_Camer
Laser Communication String :SYSTEM:INTERNAL\sON\r\n
Noise Threhold 38
Y centre 494
X centre 473

Figure A.31: The front panel of the VI used to measure the photoelectron flux as a function of laser wavelength.
A – a display showing the output wavelength of the nanosecond OPO laser.
B – a direct copy of the controls present in the Horizon™ software that interfaces with the OPO. These controls allow the user to go to a desired wavelength or initialise a continuous scan sequence.
C – a collection of controls to initialise a discreet stepwise scan sequence.
D – a status panel showing the serial ports connected to the camera and the Horizon™ software and a display showing the string commands sent to the Horizon™ software.
E – the raw data acquired from the camera is an 8-bit monochrome image and is displayed here in a high-contrast format.
F – the pixel intensity background threshold is applied to the raw image and the result is displayed here. The pixel noise threshold can be changed using the number box adjacent to E.
G – the photoelectron flux, which is measured as the sum of all the pixel intensities in the background-subtracted image, is plotted here as a function of the OPO wavelength. This plot can be reinitialised 'on demand' by the button on the right.
H – the proportion of photoelectrons with eKE ~ 0 eV, which are present in the central region of the velocity-map, is plotted here as a function of the OPO wavelength. The location of the centre of the velocity-map can be changed using the number boxes adjacent to E. This plot can be reinitialised 'on demand' with the button in the bottom right corner of the VI.
I – the cumulative image overlays each image with all of the previous images in order to generate a heat map.

Appendix B

Operating the instrument

The following manual will explain how to control the instrument through the electronics rack, operate the laser and maintain the vacuum and the components therein.

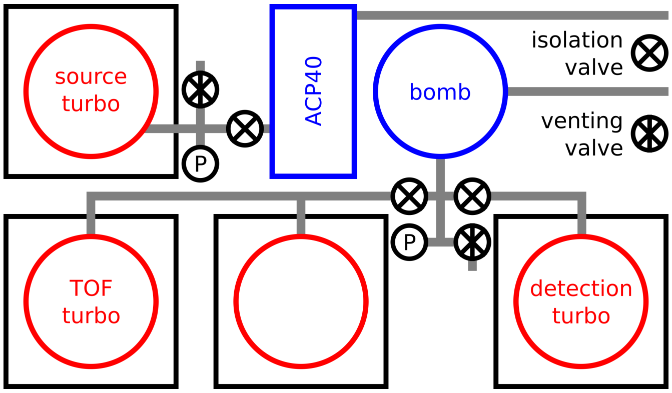

Figure B.1: A schematic of the pumping system. The turbos can be isolated from the backing pumps with the isolation valves. The pressures in the backing lines are monitored by Pirani gauges and the chambers can be vented through the venting needle valves.

B.1 Managing the vacuum

The vacuum chambers are evacuated by sequential pumping steps of distinct pressure differentials. Each of the 4 turbos maintains the high vacuum in the chambers with a pumping speed of 700 $\mathrm{l\,s^{-1}}$. The ultimate pressure of the chambers is around 1×10^{-9} mbar. The pressure in the exhaust lines of the turbos mustn't be higher than 1×10^{-1} mbar while the turbos are running. This is achieved by the backing pumps. The turbo in the Source chamber is backed by the Pfeiffer ACP40, which has a pumping speed of 40 $\mathrm{m^3\,h^{-1}}$. The turbos in the TOF, Detection and empty intermediate chambers are backed by the Edwards EPX180NE 'bomb', which has a pumping speed of 170 $\mathrm{m^3\,h^{-1}}$. This combination of turbos and backing pumps is a dry system, ensuring minimal contamination of the high vacuum from lubricant vapours. The exhaust lines from the backing pumps are vented through the ceiling line.

A diagram of the pumping system is shown in Figure B.1. A diagram of the corresponding water cooling system is shown in Figure B.2.

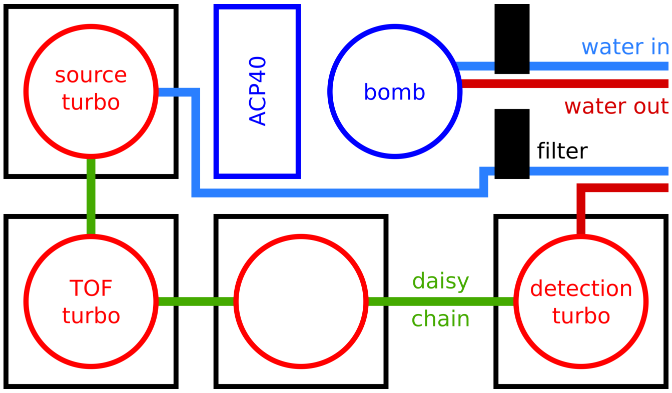

Figure B.2: A schematic of the system providing water cooling to the pumps. Each of the two loops has a filter on the inlet line to prevent contaminants from clogging the internal spaces within the pumps. The bomb has its own loop due to the high heat load it generates. The turbos are daisy-chained together.

B.1.1 The gate valve

The gate valve, shown in Figure B.3, allows the two halves of the instrument to be isolated from one another. Either side may safely be under vacuum while the other is at atmospheric pressure. This is useful because the detectors in the Detection chamber require a clean vacuum and minimum exposure to the atmosphere while the other chambers may periodically and safely be exposed to the atmosphere. The delicate MCPs in the detectors are hygroscopic and are susceptible to stress each time the chamber is cycled between atmosphere and vacuum.

The gate valve also acts as a safety device. The interlock that controls the gate valve, described in Appendix A.1.2, is connected to the Pfeiffer Maxigauge pressure monitor and will shut the gate valve automatically if the pressures in the chambers exceed predetermined set-points. Obviously, the gate valve must only be open when both sides of the valve are under vacuum (or both are safely vented to atmosphere). The actuation is achieved with a solenoid and compressed air line at the top of its rectangular housing. Warn others in the lab before operating the gate valve – the noise can be alarming if unexpected. To actuate the valve, ensure that the pressures in the chambers are at safe levels and press the corresponding white button to open or close the valve. A loud hiss and click will confirm the valve has moved and the open button on the interlock will illuminate if the valve is open. Check the mechanical indicator on the top of the gate valve to ensure the white mark is where it is expected to be. You may observe a brief spike in pressure in the Detection and TOF chambers as a small amount of gas is released from trapped volumes within the gate valve mechanism.

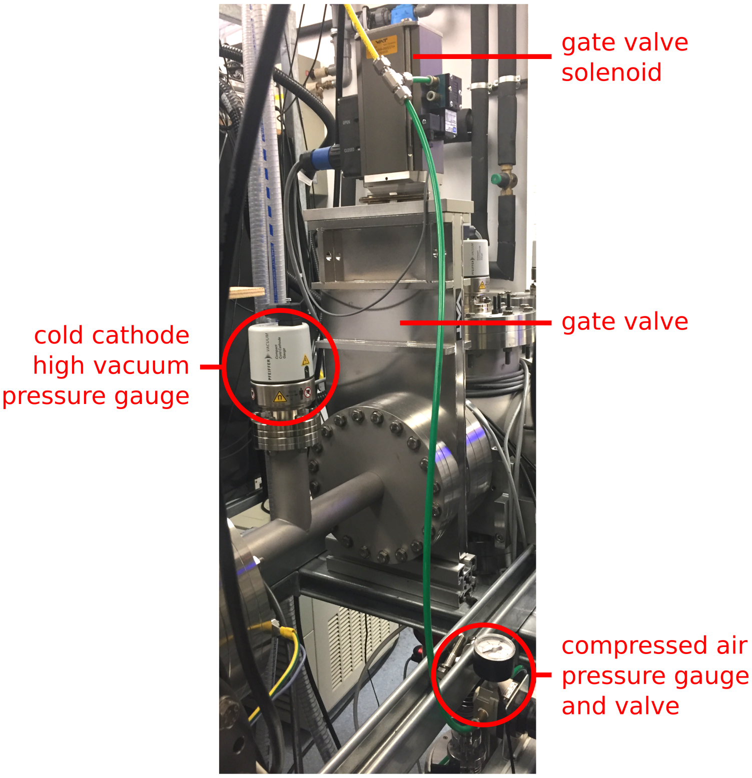

Figure B.3: The gate valve relies on a supply of compressed air to actuate. The pressure gauge and valve to control the supply are fixed to the frame of the instrument behind the electronics rack.

If the valve did not actuate, check the following:

- Is the interlock on?
- Did you press the right button to open/close the valve?
- Check the MaxiGauge. Are the pressures in all chambers below the setpoints?
- Is the compressed air line pressurised? There is a circular analogue pressure dial on the frame of the instrument behind the control rack, shown in Figure B.3. It is connected to a green nylon pneumatic line that supplies the gate valve and the bomb. It ought to read ~ 5 bar.
- If all the above are ok, try overriding the interlock and actuating the valve again.
- If the gate valve still won't actuate, consult with the manufacturer, VAT.

B.1.2 Turning on the pumps and evacuating the chambers

1. Ensure the chambers and exhaust lines are all sealed and that any valves to atmosphere are shut. Check the gate valve is shut.
2. Familiarise yourself with the Pfeiffer MaxiGauge pressure readout display. Ensure the pressure gauges in the chambers themselves are off.
3. Ensure the isolation valves between the backing pumps and the idle turbos, shown in Figures B.4 & B.5, are closed.
4. For the Edwards bomb, make sure the water in the cooling line is flowing.
5. If they are not already running, turn on the backing pumps and wait for the pressure in the backing lines to reach 1×10^{-3} mbar (Edwards bomb) or 2×10^{-2} mbar (Pfieffer ACP40). This may take 5 - 10 minutes.
6. *Slowly and carefully* ease open the valves between the backing pumps and the turbos, starting with the ACP40 and the Source chamber. This will begin to evacuate the chambers to a rough vacuum. As you proceed, do not let the pressure in the ACP40 backing line exceed $\sim$ 10 mbar so as to prevent a large pressure gradient between the adjacent chambers.
7. When the ACP40 isolation valve is fully open, repeat the process for the bomb. As you open this isolation valve, do not let the pressure in the backing line exceed 1×10^{-1} mbar especially if the Detection chamber is already under high vacuum. If this is the case, the Detection chamber turbo must be protected from pressure spikes in its backing line; you may wish to close its isolation valve while you evacuate the other chambers but do not forget to open it again. It may take 10 - 15 minutes of gradually opening these isolation valves to achieve an adequate rough vacuum. Use an appropriately placed mirror in order to monitor the pressure gauge while operating the isolation valves around the back of the instrument.
8. Once the isolation valves are fully open, allow the pressure to drop below 5×10^{-3} mbar (Edwards bomb) or 5×10^{-2} mbar (Pfeiffer ACP40). This may take about 20 minutes.
9. Turn on the pressure gauges in the relevant chambers. The display will probably show a reading of $> 1 \times 10^{-2}$ mbar.
10. Ensure the turbo controller units, shown in Figure B.6, are powered and idle.
11. Simultaneously press the ⦶ buttons on the turbo controller units to turn on the turbos in the relevant chambers, all the while monitoring the pressure gauge readouts on the MaxiGauge display. The pressure should drop rapidly to 10^{-6} mbar and slowly fall further toward 10^{-7} mbar.

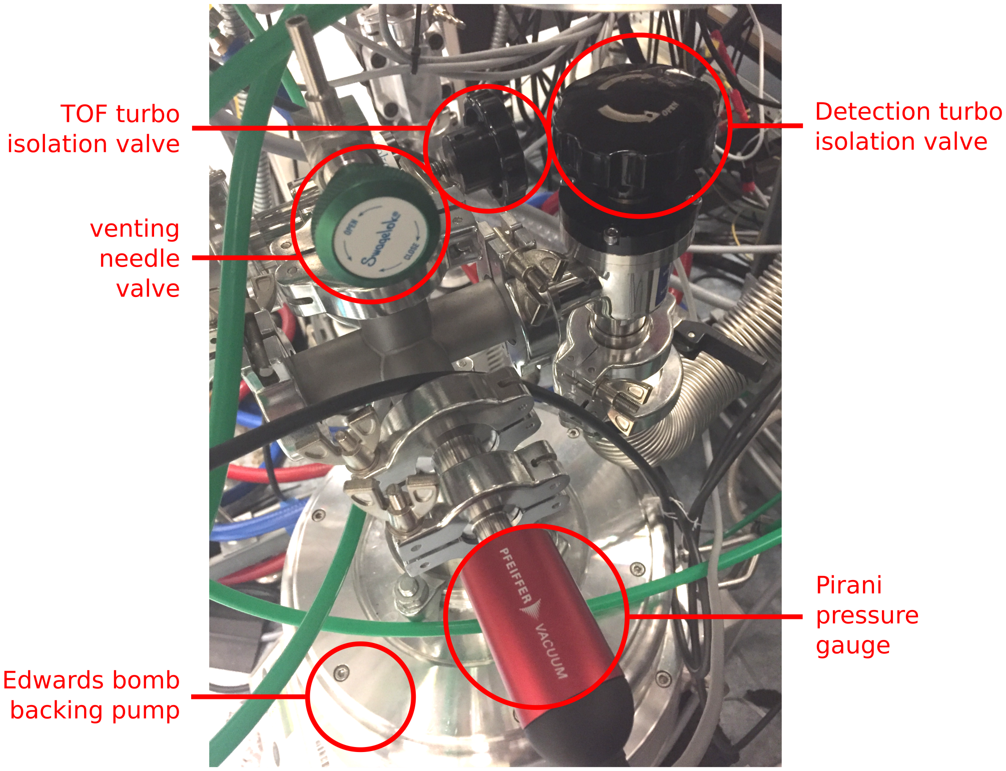

Figure B.4: The backing line system serving the Edward bomb backing pump. The isolation valves sit between the bomb and their respective turbos. The venting valve must only be opened when the bomb is switched off while returning the chambers to atmospheric conditions. The Pirani pressure gauge reports to the MaxiGauge in the electronics rack.

12. If the pressure is not dropping fast enough, check for leaks by applying MeOH to each vacuum seal in turn. If a joint is leaking, the MeOH will freeze in the gap and the pressure readout will fall suddenly and then rise as the MeOH sublimes.
13. The pressure will continue to drop over the course of several weeks but experiments may be performed after only a few hours. However, the electron gun filament and detectors must be conditioned after exposure to atmosphere. Refer to Appendix B.1.5 for details.

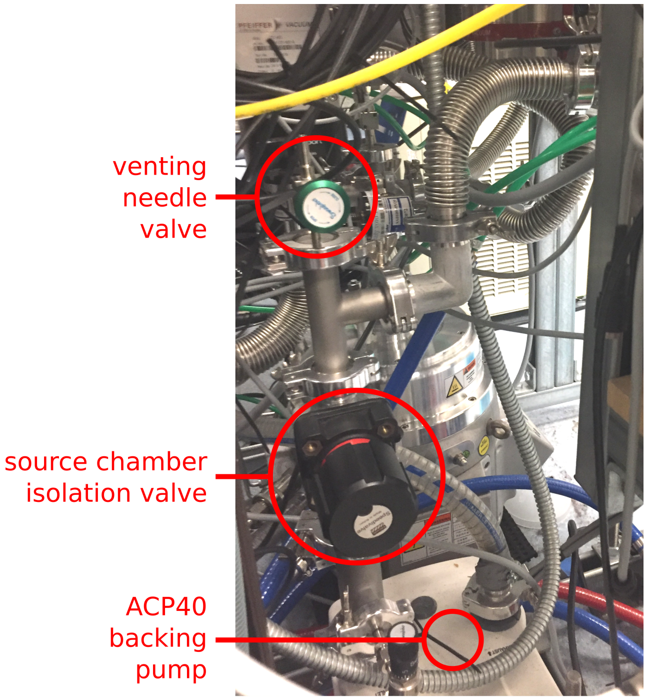

Figure B.5: The backing line system serving the ACP40 backing pump. The isolation valve sits between the ACP40 and the Source turbo. The venting valve must only be opened when returning the Source, TOF and adjacent empty chambers to atmospheric conditions.

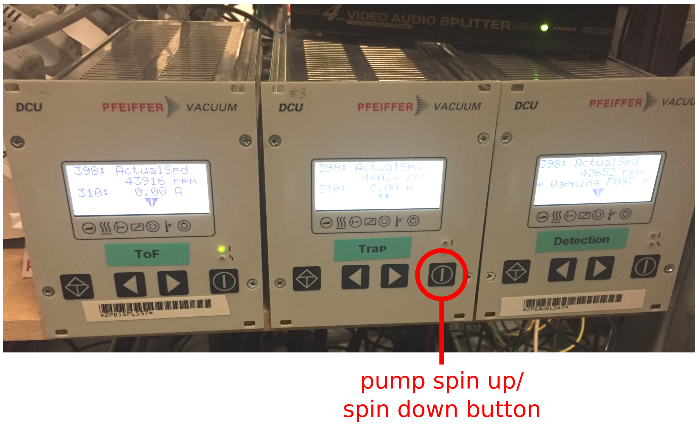

Figure B.6: The control units for the turbos. Three of them sit on the shelf under the Detection chamber and the fourth sits under the Source chamber.

B.1.3 Turning off the pumps and venting the chambers

1. Check the gate valve is shut.
2. Simultaneously switch off the turbos in the relevant chambers by pushing the ⦶ button on their controller units and immediately close the isolation valves between the turbos and backing pumps.
3. Turn off the pressure gauges in the relevant chambers using the Pfeiffer MaxiGauge.
4. Turning off the backing pumps is optional.
5. Allow the turbos to spin down. This may take up to an hour. Refer to the turbo control unit displays to monitor the speed of the turbines.
6. Once the turbines have stopped, slowly open the venting needle valve, shown in Figure B.5, to vent the chamber. Do not let gas in too quickly as it may cause the skimmer to crumple or damage the MCP detectors. Do not open the venting needle valve shown in Figure B.4 unless the bomb has been switched off.
7. Place a finger over the aperture of the venting valve to gauge whether air is still entering the chambers. Wait until atmospheric pressure is restored to the chambers before undoing any flanges.

B.1.4 Turning off the pumps in case of power failure or water shutdown

The following steps are very similar to the instructions for turning off the pumps normally:

1. Check the gate valve is shut. It should automatically shut itself in case of power failure.
2. Close the three isolation valves between the turbos and the backing pumps immediately, starting with the valves in the bomb backing line and then the ACP40. This will help to preserve the lowest pressure in the chambers while the pumps are off.
3. The turbos will already be spinning down and the whine of the turbines should be audible. However, their controllers have batteries in them and so will display the error warning associated with power failure. Push the power buttons ⏻ on the front of each unit to prevent the turbos from automatically spinning back up when power returns. Monitor the turbo control unit displays to check the speed of the turbines. They may take up to an hour to spin down.
4. Turn off the pressure gauges in the relevant chambers using the Pfeiffer MaxiGauge.
5. The backing pumps will already have turned off. They are connected to a no-voltage return (NVR) switch and ought to remain off even when the power returns. Push the rocker switch on the ACP40 to ensure it doesn't start up when the NVR is reset.
6. Push the rocker switches on the back of each turbo control unit to ensure that they remain off when power returns. Their displays will only turn off when their batteries run out.

B.1.5 Conditioning the microchannel plate detectors and electron gun filament

When the electron gun filament or detector MCPs are exposed to atmosphere, they become coated with adsorbates that may damage the components during operation if they are not first gently purged. This process is called conditioning and essentially just involves slowly turning up the voltage applied to each element to its operating level. To condition the electron gun filament, increase the current passed through it in steps of 0.25 A at intervals of 10 - 15 minutes. The pressure in the Source chamber should increase slightly as the adsorbates desorb. To condition the MCP detectors, increase the potential difference across each plate by 50 - 100 V at intervals of 10 - 15 minutes. Leave the components at operating levels for at least an hour until the pressure in the chamber is clearly dropping back towards ultimate pressure. Refer to the manufacturers' instructions for further details.

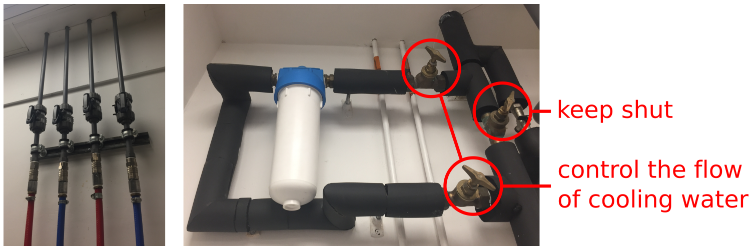

Figure B.7: The water cooling control system mounted on the south and west walls of the lab. On the left are the isolation valves for the bomb and turbo cooling lines. On the right are the stopcocks that control the rate of flow of the cooling water.

B.1.6 Power and water peripheral services

Mains power is provided to the bomb via one of the CEE industrial plug sockets on the south wall of the lab. A second CEE socket is assigned to a four-way socket strip situated on the shelf under the Detection chamber, which powers the four turbos. Two four-way socket strips issue from the ceiling-mounted Electrak power distribution boards. These strips provide power to the electronics rack and other components. A final four-way strip is plugged into a standard wall socket via a NVR unit. This strip hosts the ACP40 backing pump.

Water cooling is provided to the bomb and the turbos via two separate loops, shown in Figure B.2. The bomb has its own loop while the turbos are daisy-chained in series in a loop. Both loops have a filter on the inlet side to ensure contaminants are not able to clog the cooling passages inside the pumps. The rubber hoses are connected to push-fit terminals near the ceiling on the south wall of the lab, shown on the left of Figure B.7. The rate of flow can be controlled by the stopcocks next to the filter in the manifold system mounted high on the south side of the west wall of the lab, shown on the right of Figure B.7. The pressure gauge ought to read a little less than 1 bar of overpressure. During operation, the top surface of the bomb ought to be warm, but cool enough to rest your hand on it without discomfort. If the water cooling flow is too low, the pump will overheat and automatically spin down, which would be very damaging to the turbos if they are running.

B.2 Initiating the beam and finding signal

B.2.1 Obtaining a time-of-flight signal

Assuming the pressures in the vacuum chambers are suitable for operation and all the electronics are powered and connected, undertake the following instructions to generate a TOF spectrum.

1. Prepare a high pressure gas sample in the manifold and introduce it to the Even-Lavie valve. As you do so, check that the pressure in the Source chamber doesn't rise significantly. If it does, the valve may be leaking and the gaskets may have expired. Consult Appendix C.3.
2. Turn on the electron gun to the recommended voltages detailed in Appendix A.1.5. Make sure all the electrodes are at their full voltage before turning on the filament. A general principle that applies to any of the power supplies in the rack is that if the voltage output displayed is not stable or continuously adjustable, there is something wrong. It usually indicates that too much current is flowing through the supply and it must be fixed before proceeding. An abnormally high current would suggest that there may be a short-circuit inside the instrument or within the power supply unit itself. Disconnect the cables between the supply and the instrument to narrow down where the issue lies. In the case of the electron gun it may be that the beam current is too high or not well-contained and that it is crashing into the electrodes. This is why the electrodes must be at full operating voltage before the electron beam is formed.
3. If this is the first time of operating since exposure to atmosphere, the filament must be conditioned as described in Appendix B.1.5. Before turning up the filament current, consult the analog voltage display on the filament power supply. If it does not indicate 0 V but is rather nearer 10 V, the filament is broken or disconnected and will need fixing. See Appendix C.2. Turn up the filament current slowly; it should take at least one minute to achieve the operating voltage.
4. Switch on the pulse generator and initiate pulsing if it is not already running. Ensure that the correct timing regime is active for the laser system being used. Recommended timing regimes are described in Appendix A.1.1.
5. Turn on the ion optics electronics unit. The recommended voltages are listed in Appendix A.1.6.

6. Turn on the Even-Lavie valve controller unit and heater (if required) and set the desired parameters. Recommended conditions are listed in Appendix A.1.4. Start the valve with the red button while monitoring the pressure in the Source chamber displayed on the MaxiGauge. Look through the viewport on the top of the Source chamber to view the glow discharge in the supersonic expansion in front of the valve. Turn off the lab lights if necessary.

7. Turn on the TOF detector power supply to the recommended voltages listed in Appendix A.1.7.

8. Turn on the oscilloscope and ensure the signal cable is connected.

9. Open the gate valve, alerting others in the lab as you do so.

10. Adjust the relative timing of the Even-Lavie valve trigger pulse and the TOF plates' trigger pulse as described in Appendix A.1.1 until the oscilloscope shows some signal.

11. Adjust the following parameters to optimise the signal levels:
    - voltages of the deflectors
    - voltages of the einzel lenses
    - TOF extractor plate voltage
    - relative timing of Even-Lavie valve trigger pulse and TOF plates' trigger pulse
    - electron gun filament current
    - valve location relative to electron beam
    - gas sample pressure

12. Note that some of these parameters are interdependent and that adjusting one may require changing others to compensate. For example, by moving the Even-Lavie valve closer to the electron gun beam, the relative time delay between the pulses that trigger the valve and the TOF plates must be shortened. Cycle through the above parameters in an iterative manner to produce the greatest signal level for the desired peak.

B.2.2 Turning on the nanosecond optical parametric oscillator laser

The following steps will turn on the nanosecond OPO system described in Appendix A.2.1.

1. Ensure the *Laser On* warning light outside the lab is illuminated.
2. If not already on, toggle the power switch on the Surelite laser power unit on the floor beside the laser table, shown in Figure B.8, and turn the key to the *On* position. Wait for the display to show *Flo* and *EOn* before proceeding. The flashlamp in the Surelite laser is now being cooled by the water cooling lines. Do not press any more buttons yet.
3. Open the Horizon™ software interface on the computer (it will take about a minute to initialize if it has previously been closed) and move the laser to the required wavelength. At this point the Surelite laser isn't flashing so the dialogue box requiring the Q-switch to be off may be dismissed.
4. The switch-over point between the UV aperture on the left of the OPO unit and the visible/IR aperture on the right is 400 nm. Open the lid of the OPO and toggle optics B and D if prompted to by the software.
5. The following actions will ensure that LabVIEW can communicate with the laser. In the Horizon™ software, navigate to the *Tools > External Interface* menu and select *On*. The *Port Ready* indicator on the front window of the software should illuminate. Ensure there is a working port bridge between COM2 and COM4 in the *Free Virtual Serial Ports* utility installed on the lab computer.
6. Position the 90° prism periscope on the magnetic base in front of the correct port. This periscope rotates the image and polarisation of the laser by 90°.
7. Wait 5 - 10 minutes and then press the *Start/Stop* button on the Surelite laser power unit. Check that you can hear the ticking noise from the power unit and that you can see the faint reflection of flashing from the flashlamp around the adjustment knob on top of the laser housing. If no ticking or flashing is observed, check the delay generator is correctly triggering the power unit. If an error message is displayed on the power unit, consult the Surelite manual.
8. Wait a further 10 - 15 minutes for the flashlamp to warm up and then press the *Shutter* button on the laser power unit. This turns the Q-switch on and initiates lasing. Scattered green light should then be observable around the entrance to the OPO unit at the rear of the box.

Figure B.8: The power supply and controller for the Surelite laser.

9. When the rest of the experiment is up and running, open the relevant aperture on the OPO unit and check the beam path of the laser, adjusting the final two prisms before the chamber as necessary. Always reduce the laser power while performing alignment.

10. In order to rotate the polarisation of the laser back to the horizontal plane, it must pass through the adjustable Alphalas $\lambda/2$ waveplate. The rotation of the polarisation can be measured by placing a thin window at Brewster's angle in the beam path and monitoring the intensity of the reflection. The waveplate is adjusted when the reflection is at its least intense. This will need to be done any time the laser wavelength is changed.

11. To turn off the laser, shut the mechanical shutter over the active aperture on the OPO unit, press the *Shutter* button on the Surelite power unit, followed by the *Start/Stop* button. Turn the key to complete the shut down process.

B.2.3 Turning on the femtosecond pump-probe laser

The following steps will turn on the femtosecond pump-probe system described in Appendix A.2.2.

1. Ensure the *Laser On* warning light outside the lab is illuminated.
2. Ensure the chiller unit on the floor is on and steady at 28°C.
3. Switch on the Spitfire Pockels cells power supply unit, shown in Figure B.9, that sits on the corner of the shelf above the laser table. The Spitfire temperature and humidity controller immediately above this power supply should remain on at all times. Wait for the light emitting diode (LED) status light to stop flashing and then turn the key to switch on the Pockels cells.
4. The Empower power supply unit on the shelves under the OPO laser table extension, shown in Figure B.10, must be reset to clear a recurring fault. Turn the key to the *Off* position and then return it to the *On* position.
5. Press and hold the *Run* button on the Millenia control unit, shown in Figure B.11, until the Millenia laser switches on. It will take a few minutes to warm up. Reduce the target power output to ~ 2.5 W and wait for the measured output to reach the target. Once stable, the target power output can be raised back to 4.45 W.
6. Open the Spectra Physics software on the laptop adjacent to the laser table, shown in Figure B.11. Ensure the interface has loaded properly (the Pockels cells current reading should be around 20.0 A) and clear the faults.
7. Press and hold the *Run* button in the software window until the square indicator light on top of the Empower laser unit illuminates, which will be accompanied by an audible click. Wait for the *OSC Freq* indicator to show ~ 76 MHz and then press the *Lock OSC Freq* button.
8. The laser system will take 2 - 3 hours to warm up. The output of the laser can be monitored in the Ocean Optics spectrometer software on the laptop.
9. Ensure that the mechanical shutter in front of the Spitfire output port, which is controlled by the red stop buttons around the lab, is shut. When laser output has reached full power over the expected spectral range, press the *Reset BWD* button in the software window.
10. Open the *Channels* dialogue in the software window and enable the Pockels cells, *Channels* 3, 2 and 1 (in that order), to enable the beam to exit the output port.

Figure B.9: The power supplies that control the Spitfire femtosecond pulse amplifier. The temperature and humidity controller should remain on at all times (this image was taken as the power was being shut off). The Pockels cells power supply may take at least a minute to turn on.

11. Open the mechanical shutter and check the beam path of the laser, adjusting the final two mirrors before the chamber as necessary.

12. To turn off the laser, shut the mechanical shutter, disable Channels 1, 2 and 3 in the software and press the *Stop* button to halt the operation of the Empower. Stop the Millenia pump laser, turn key in the Spitfire power supply to disable the Pockels cells and then turn off the power supply. Do not turn off the Spitfire temperature and humidity power supply.

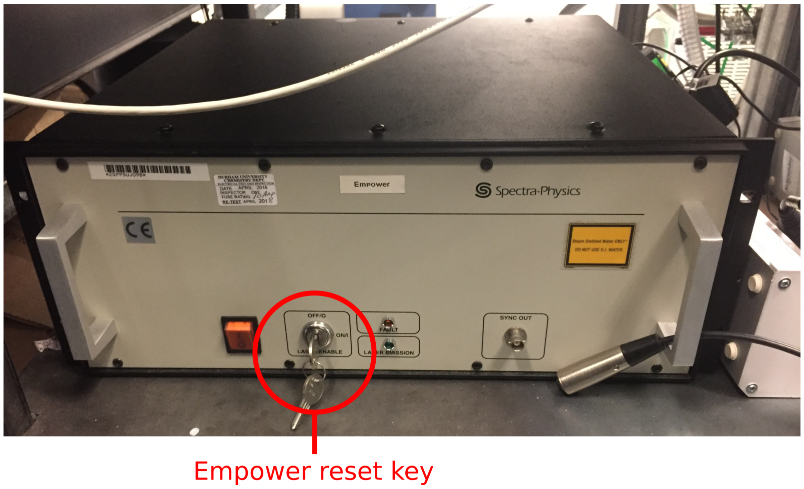

Figure B.10: The power supply for the Empower laser is located under the laser table extension on which the OPO unit sits. The key must be turned to the *Off* position and back to *On* again to clear a recurring fault before the Empower starts lasing.

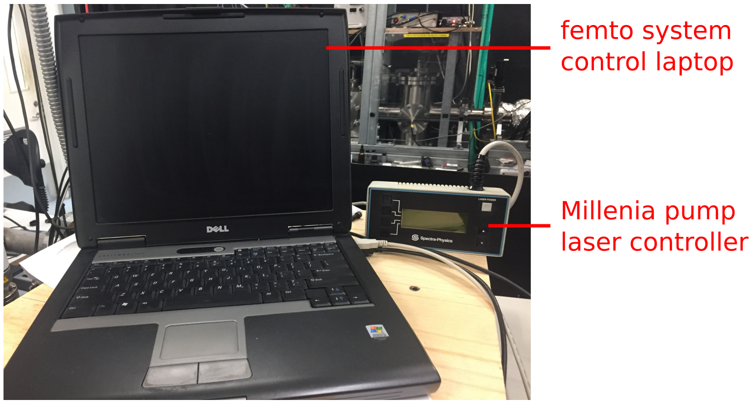

Figure B.11: The laptop that controls the femtosecond laser system and the Millenia laser control unit.

B.2.4 Obtaining a velocity-map imaging signal

Once TOF signal has been acquired and the laser has been turned on, undertake the following steps to generate a photoelectron VMI signal.

1. Open and run the relevant LabVIEW VI for performing a frequency-resolved, time-resolved or photoelectron flux measurement. There is no need to save the data while the signal levels are being optimised. If the nanosecond OPO is being used, the Horizon™ software will need to be open and listening for an *External Interface* through a port bridge. Refer to Appendix B.2.2 for instructions.
2. Block the laser path at the entrance to the chamber.
3. Turn down the filament current supply to below 3.0 A if the peaks in the TOF spectrum on the oscilloscope trace have intensity $>$ 500 mV.
4. Plug the 12 V DC power cable into the DEI HV pulser that supplies the VMI repeller plate.
5. Ensure the camera is plugged in and powered. A small green LED on the back of the housing will confirm this.
6. Turn on the VMI detector power supply and press the *HV On* button. The MCP In channel will already be at its operating voltage. Turn the other channels up slowly to just below the recommended operating voltages listed in Appendix A.1.8.
7. Adjust the relative timing of the TOF and VMI triggers on the pulse generator. This delay ought to be ~ 93.5 % of the TOF of the desired mass packet in the oscilloscope trace.
8. While monitoring the VMI detector signal levels on LabVIEW display, unblock the laser and optimise the signal levels using the following steps:
   - Although unlikely at first, high signal levels may overload the detector, which can damage it. The same problem may occur if the laser is misaligned and scatters significantly off the internal surface in the chamber. If the camera image saturates as soon as the laser enters the chamber, block the laser again and turn down the electron gun filament current and the VMI detector power supplies. Realign the laser if necessary and try again.
   - What's more likely is that there is little or no signal at first. If this is the case, start by turning up the VMI detector power supply channels to their full recommended operating voltages. At least some ion noise should become visible in the camera output.

  - Fine tune the relative timing of the TOF and VMI triggers on the pulse generator in order to maximise signal levels.
  - Carefully adjust the vertical inclination of the final mirror or prism directing the laser beam into the chamber in order to maximise its overlap with the ion beam. Adjusting the horizontal alignment is unnecessary because it is equivalent to fine tuning the timing of the pulse, which was already addressed in the previous step. Always monitor the camera output while making such adjustments to avoid damaging the VMI detector.
  - If signal levels are particularly low, the TOF extractor plate may be turned down by ~ 50 V to around − 2.63 kV thereby moving the temporal focus and point of highest ion density off the front surface of the TOF detector and into the VMI interaction volume. Adjusting the operating voltage of the einzel lens inside the Detection chamber may also increase the ion density in the interaction volume. Be aware that adjusting these two parameters will affect the TOF and relative timings will need to be corrected accordingly.
  - The signal level may fluctuate over time and if it becomes too intense for the detector, the best way to lower it is to reduce the number of ions by turning down the electron gun filament rather than turning down the detector. In this way, individual photoelectron strikes do not risk appearing too faint to exceed the noise threshold applied by the LabVIEW VI.

9. Once the photoelectron signal level is adequate, a scan of laser wavelength or pump-probe time delay can be started in the LabVIEW interface.

B.2.5 Suspending the beam and powering down

1. Stop data acquisition on the lab computer.
2. Block the laser path and switch off the laser if required.
3. Shut the gate valve.
4. Stop the Even-Lavie valve and switch off the control unit and the heater controller.
5. Turn down the electron gun filament current followed by the channels powering its electrodes. Switch off the rack units when all voltages are returned to 0 V.
6. Turn down all the channels on the detector power supplies with the exception of the MCP In voltage applied to the VMI detector. The putty securing the dial in place should preserve its setting. Switch off the rack units when all voltages are returned to 0 V.
7. Switch off the ion optics rack unit. It is not necessary to turn down the voltages on these channels.
8. Stop the pulse generator if desired.
9. Unplug the DEI HV pulser that supplies the VMI repeller plate.

Appendix C

Maintenance of the internal components

When it becomes necessary to open up a vacuum chamber for maintenance, there are a few things to bear in mind:

- Always wear nitrile gloves when handling components exposed to the vacuum. Everything has been cleaned and skin oils or moisture deposited on surfaces can outgas for months, limiting the ultimate pressure and introducing unwanted contaminants into the vacuum.
- Even with gloves on, do not touch surfaces and components that don't need to be touched. A vacuum chamber can quickly achieve the low ultimate pressure it enjoyed before venting if it remains undisturbed. One single disturbance can dramatically affect how long it takes to pump out again.
- If new components are being introduced to the vacuum, clean them by sonicating them first in soapy water, then in MeOH. Finally, rinse with MeOH and dry with paper towel and an air gun before assembly. Machine grease and other lubricants are bad for the vacuum and may create pathways for HV elements to short-circuit and discharge.
- Avoid exposing insulator materials to the path of charged particles. The surface of the insulator will become charged and may deflect the beam in such a way as to disrupt the ability to perform experiments.
- Make sure all components, particularly small ones, are securely fastened in their respective assemblies. The mesh that covers the face of the turbo in each chamber will prevent most things from dropping through but some smaller items may be able to pass through the holes. If anything is dropped through these holes, the pump will have to be removed and inverted to extract the object. This would take weeks. Don't risk it.

- The M8 nuts and bolts external to the chambers that fasten the vacuum seals together must be lubricated with molybdenum disulphide lubricant in order to prevent them from seizing. Nuts and bolts may need to be replaced periodically if the threads become damaged.

C.1 The conflat system

The CF standard is a robust system for containing a vacuum. A seal is formed when a copper gasket is crushed between two knife-edge profiles on opposing stainless steel flanges. It is very important to tighten the bolts in such a way as to ensure the gasket is evenly crushed around the circumference so that there are no leaks. To make a seal, you will need:

- 2 × 13 mm spanners
- thick protective gloves
- a fresh unused copper gasket
- stainless steel nuts and bolts of an appropriate length
- a lot of strength and energy

1. Start by placing the two sides of the junction together with a copper gasket between them.
2. Insert a few bolts and loosely do up the nuts and washers to hold it all in place.
3. Wiggle the junction until the gasket settles into the grooves of both faces and then finger-tighten the nuts, ensuring the two flanges are coaxial. There should be a uniform gap of ~ 1 mm between the faces of the two flanges in which the orange of the copper gasket can be seen.
4. If the flanges are vertical, start with the bottom 2 or 3 nuts. Tighten the nuts slightly using one 13 mm spanner on the bolt head and one on the corresponding nut.
5. Switch to the 2 or 3 bolts directly opposite on the top side of the flange and slightly tighten those.
6. Continue to the 2 or 3 bolts on the left or right of the flange and tighten. Do the same with the 2 or 3 bolts opposite.
7. Go back to the bottom bolts and tighten further. Repeat the pattern of crossing the flange to the opposite set of bolts to ensure that the gasket is crushed evenly around. As the bolts get tighter you may wish to wear the gloves in case one of your spanners slips and you strike your hand against a sharp edge of the instrument.

8. The visible gap between the faces of the stainless steel components should shrink to a fraction of a millimetre as the gasket is crushed. Eventually the nuts and bolts will be tight enough that you can just go round them in a circle incrementally tightening them until they don't tighten any more. This will require a good deal of strength and you will get tired.
9. Be aware that flanges with alignment rods embedded in them will require greater force to tighten as the rods may somewhat resist being pushed into the flange opposite.
10. Once the chamber is evacuated you may check for leaks with methanol. Squirt a little onto the joint and if the pressure suddenly drops and then rises, it indicates a leak at that point.

C.2 Electron gun filament replacement

The electron gun can be operated safely at a filament current of ~ 3.2 A. If run higher than ~ 3.5 A for longer than a day or two, it is liable to burn out. If the current suddenly drops to zero or the analogue voltage meter reads higher than 5 V in the absence of current, it is a fair indication that the filament has blown. Although replacing the filament may only take about 90 minutes with experience, taking the vacuum system up and down from atmosphere is likely to take most of a day. This is therefore a situation to avoid if possible. However, if you do need to replace the filament, consult the following instructions and the corresponding pictures in Figure C.1. You will need:

- A clear work area with good light
- A suitable container for small components
- Nitrile gloves
- Needle-nose pliers
- 2 × 13 mm spanners
- Fine-point tweezers
- 0.9 mm hex head driver
- 1.5 mm hex head driver
- 2.5 mm flat-head driver
- A fresh Agar Scientific Ltd AG054L filament

1. Stop whatever experiment is running (Appendix B.2.5) and vent the Source, TOF and adjacent empty chambers (Appendix B.1.3).
2. Loosen the perspex tube that protects the electron gun electrical connector and slide it back along the black cable conduit. Slide the cable connector off the copper pins that connect to the electron gun.
3. Using the 13 mm spanners, loosen the eight M8 bolts around the flange holding the electron gun, being careful not to let the flange slip lest the electron gun shaft be damaged by hitting the inside surface of the chamber.
4. Remove the electron gun from the chamber, being careful not to get molybdenum disulphide grease on the internal components, and place it connector-side-down on a clear and well-lit section of worktop. Instead of balancing the electron gun on its pins, find a suitable object like a dewar to stand it on.

5. Find a container for small and delicate components and put on some fresh nitrile gloves
6. Completely undo the four M2 flat-head screws around the base of the electron gun shaft. Remove the shaft and set to one side.
7. Using the needle-nose pliers, completely undo the four small nuts around the conical aperture at the tip of the gun and set to one side with their respective washers. The M2 threaded rod may drop and disappear; don't worry about this.
8. Remove the conical aperture and set to one side. Remove the four black SiN ball bearings.
9. Remove the ceramic rods insulating the M2 stud.
10. Loosen (perhaps 1/2 turn) the two M2 grub screws on each of the four deflector elements and remove each element in turn. Remove the next four SiN balls.
11. Loosen the two M2 grub screws on the next element and gently ease the element over the loose wires, being careful not to bend or pull on them. Remove the next four SiN balls.
12. Repeat the step above until you get to the Wehnelt. When lifting the last element, do not lift it completely but expose a gap large enough to get the tweezers in and disconnect the two crimp connectors on the underside of the filament.
13. Loosen the M3 grub screw on the side of the Wehnelt and remove the filament with tweezers.
14. Get a new filament and insert it into the base of the element. Ensure that the tip of the filament protrudes centrally from the pinhole by approximately 0.2 mm. If it is not central, nudge the filament until it is.
15. Gently secure the new filament in place with the grub screw. The plastic disc holding the wire is prone to crack so don't over-tighten it.
16. Reassemble the elements following exactly the reverse process. Don't forget to reattach the crimped wires to the filament itself. Be careful not to bend the wires or strip off the insulation as they pass through each element. Do not over-tighten the grub screws or the wire inside will deform and make future disassembly very difficult. If you drop any of the SiN ball bearings or M2 grub screws, there are spares in the prep room.
17. If you have to replace a wire, be sure to use 5 kV rated kapton insulated wire. Disconnect the old wire from the push-on connector at the flange, cut off the end and pull through from the top. Perform the opposite to install a new wire.

18. If the M2 stud that runs the length of the shaft slips down, push it up from below with an allen key and hold it while you tighten the conical nozzle. This will be the most fiddly part of the process.

19. Before the shaft cover is replaced, check the electrical connectivity between each element and its respective pin with a multimeter. There should be electrical continuity between the two pins assigned to the filament. Also check for any accidental shorts between elements and to ground on the flange.

20. If necessary, clean any dirty components with MeOH.

21. Place a fresh copper gasket on the flange and reattach the electron gun to the instrument. Ensure that the x and y deflectors point vertically and horizontally before tightening the M8 bolts. This can be assessed by looking at the alignment of the four nuts on the conical tip of the assembly, which line up with the gaps between the deflectors. Refer to Appendix C.1 for instructions on forming the vacuum seal.

22. Evacuate the chambers (Appendix B.1.2) and recondition the filament (Appendix B.1.5) once the pressure is below 10^{-6} mbar in the Source chamber.

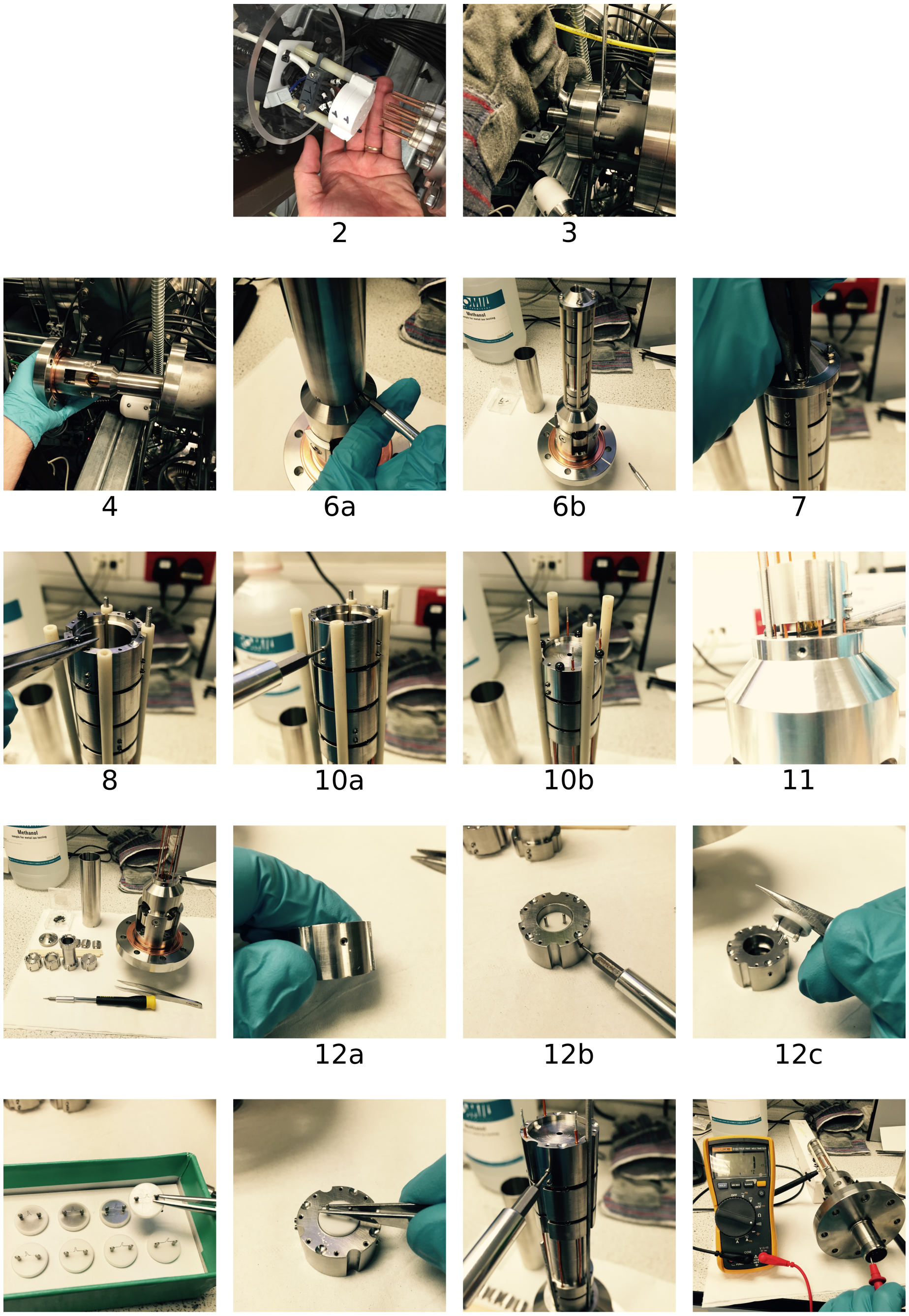

2
3
4
6a
6b
7
8
10a
10b
11
12a
12b
12c
13a
13b
15
18

Figure C.1: Pictures to guide the process of replacing the electron gun filament. The number below each image corresponds to the step number in the instructions in Appendix C.2. Larger images are available in the digial appendix.

C.3 Removing the Even-Lavie valve

The Even-Lavie valve may begin to leak if the polyamide gaskets fail. A sign of this will be that the base pressure in the Source chamber rises from ~ 10^{-8} to ~ 10^{-6} mbar when high pressure gas is introduced to the valve even though the valve is not operating. To remove the Even-Lavie valve from the Source chamber consult the following instructions and the image in Figure C.2. You will need:

- a clear work area with good light
- a suitable container for small components
- nitrile gloves
- 14 mm spanner
- 2 × 13 mm spanners
- 7 mm spanner
- 2 × 8 mm spanners
- the Even-Lavie toolkit, including fresh polyamide gaskets

1. Stop whatever experiment is running (Appendix B.2.5) and vent the Source, TOF and adjacent empty chamber (Appendix B.1.3).
2. Isolate and remove the manifold from the terminal flange of the Source chamber.
3. Remove the multipin feedthrough connector from the same flange.
4. Remove any obstacles in the Unitrunk framework that may obstruct the flange as it is removed.
5. Undo the M8 bolts securing the terminal flange of the Source chamber, leaving one on top and one on the bottom until last.
6. With one hand on the underside of the flange and the other on the translator, slowly and carefully pull the flange straight backwards, away from the chamber. Be sure to bear all of the weight as you do, so as not to bend the alignment rods.
7. Place the flange on the bench with the alignment rods facing upwards. Rather than balancing the assembly on the translator, find an object on which the surface of the flange can rest, such as an unused vacuum chamber.

8. Put on fresh nitrile gloves.
9. Disconnect the electrical connections by sliding the black PLA casing off the pins. Leave the loose PLA disk on the pins because it has an extra hole that acts as an orientation guide for the other half of the connector.
10. Undo the 1/16" swagelok union that connects the gas inlet line to the back of the valve.
11. Loosen the three M4 nuts that secure the valve to the aluminium bronze cross.
12. Carefully lift the valve away from the assembly, being sure not to strain either the gas line or any of the wires where they connect to the valve.
13. Refer to the online Even-Lavie valve manual[140] for instructions on how to disassemble and clean the valve and replace the polyamide gaskets. This process is very fiddly and should not be undertaken lightly. The potential for damaging or losing very expensive components is high – use extreme caution.
14. When the valve is reassembled, fix it back on the aluminium bronze cross and do up the M4 nuts. Check to see that the valve is properly aligned along the central axis of the flange.
15. Reconnect the 1/16" compression union, being sure to form a seal without over-tightening the joint.
16. Reconnect the electrical pins, being sure to get the alignment of the PLA casing right. Gently twist the connector until all the pins are securely in place but avoid bending the pins unnecessarily.
17. Check the electrical connectivity of each pin before proceeding.
18. Replace the copper gasket and carry the flange back over to the instrument.
19. With one hand under the flange and the other on the translator, carefully match up the alignment rods with their respective sleeves on the flange opposite. Gently push the flange into place and insert an M8 bolt at the top and bottom to bear the weight.
20. Use a long thin object to poke the copper gasket into position and wiggle the flange gently until the gasket sits in position between the two knife-edges.
21. Replace and tighten the M8 bolts around the flange as described in Appendix C.1.

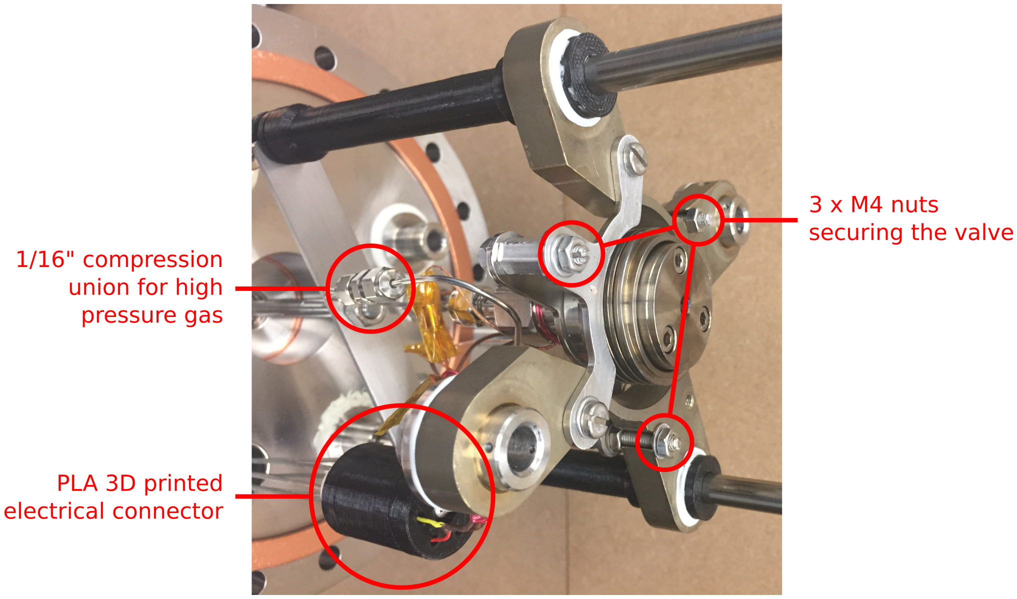

Figure C.2: The parts of the source assembly that need disassembling to access the valve.

C.4 Removing the TOF and VMI assemblies

The TOF and VMI assemblies can be removed in much the same way as the assembly in the Source chamber. However, this should be avoided as much as possible as they are more tricky to remove and replace. If it becomes absolutely necessary to do so, there are a couple of things to note about the order in which things are done.

The TOF assembly is removed from the terminal flange of the TOF chamber. However, the side flange that has the four SHV connections on it must be removed first and the four wires moved out of the way to stop them interfering as the assembly slides out of the chamber. Also, when sliding the terminal flange out, the four connections to the low voltage einzel lens (details in Appendix A.1.6) must be disconnected from the 10-pin feedthrough before the assembly can be freely removed. Be sure to reconnect these wires when placing the assembly back into the chamber.

The VMI assembly is removed from the terminal flange of the Detection chamber. However, the VMI μ-metal shield and drift tube must first be removed from the assembly, which can only be done by removing the flange on top of the chamber, on which the VMI detector is mounted. The VMI assembly is then free to slide out, mounted on the terminal flange.

Appendix D

List of apparatus & components

Table D.1: A list of key off-the-shelf components incorporated into the instrument

Description	**Manufacturer**	**Part No.**
HTL-275-1 Linear feedthrough translator	Accu-Glass Products, Inc.	102220
Tuneable zero-order $\lambda/2$ phase retardation plate	Alphalas GmbH	PO-TWP-L2-25-UVIR
Monochrome ace area scan CCD camera	Basler	acA1300-30um
Ni beam skimmer	Beam Dynamics Inc.	Model 2
Behlke fast HV transistor switches	Behlke Power Electronics	HTS 101-01
Robox® 3D printer	CEL Technology Ltd	RBX01
Camera lens	Computar®	M0814-MP2

Continued overleaf...

Table D.1 – *Continued from previous page*

Description	**Manufacturer**	**Part No.**
Surelite Q-switched Nd:YAG pump laser	Continuum®	SL II-10
Tuneable Horizon™ I OPO laser	Continuum®	–
CaF_2 UV grade laser windows	Crystran	CAFP58-3U
Negative HV pulse module	Directed Energy Inc (DEI)	PVM-1001-N
EPX180NE dry backing pump	Edwards Limited	A419-44-714
5 kV 12-pin electron gun feedthrough	LewVac Components Inc	FHP5-50C12-40CF
µ-metal shield	Magnetic Shields Ltd	MG8075
DN160CF 6-way crosses	MDC Vacuum Products LLC	407008
DN160CF viewport	MDC Vacuum Products LLC	9722012
DN160CF - DN40CF zero-length adapter	MDC Vacuum Products LLC	150083
DN160CF blank flange	MDC Vacuum Products LLC	110030
DN160CF double sided flange	MDC Vacuum Products LLC	140030
7-pin multipin feedthrough	MDC Vacuum Products LLC	9151000
7-pin multipin feedthrough	MDC Vacuum Products LLC	9152001

Continued overleaf...

Table D.1 – *Continued from previous page*

Description	**Manufacturer**	**Part No.**
6-pin multipin thermocouple feedthrough	MDC Vacuum Products LLC	9131001
10-pin multipin feedthrough	MDC Vacuum Products LLC	9131002
Millenia Pro s-Series diode-pumped CW visible laser system	Newport Spectra Physics	0000-320A, Rev. B
Tsunami mode-locked Ti:sapphire laser	Newport Spectra Physics	0000-232A, Rev. D
Empower intracavity-doubled diode-pumped Nd:YLF laser	Newport Spectra Physics	0000-334A, Rev. B
Spitfire ultrafast amplifier	Newport Spectra Physics	0000-277A, Rev. G
HiPace® 700 Turbo Pump	Pfeiffer Vacuum	PM P03 934
ACP40 dry multistage roots pump	Pfeiffer Vacuum	V8SACSFEMF
DCU 400 turbo control unit	Pfeiffer Vacuum	PM C01 823
TPG 256 MaxiGauge pressure monitor	Pfeiffer Vacuum	PT G28 760
APR 266 piezo pressure gauge	Pfeiffer Vacuum	P5 215 132 TF
IKR 270 - compact cold cathode gauge	Pfeiffer Vacuum	PT R25 751
TPR 280 Pirani pressure gauge	Pfeiffer Vacuum	PT R26 950A

Continued overleaf...

Table D.1 – *Continued from previous page*

Description	**Manufacturer**	**Part No.**
TC 400 turbo electonic drive unit	Pfeiffer Vacuum	PM C01 800A
VID240 P43 MCP detector	Photek Ltd	VID240/P43/GL
AP Long-Life™ MCP detector	Photonis	APD 2 MINI TOF 18/6/5/12 D 60:1 EDR SE
Delay stage digital translator	Physik Instrumente GmbH	M-505.6DG
Delay stage controller	Physik Instrumente GmbH	C-863 Mercury
Even-Lavie pulsed valve	Prof. Even and Mr. Lavie, Tel Aviv University	EL-7-4-2009-HRR
9520 series digital delay pulse generator	Quantum® Composers	9528 (AT35/TZ50)
20 mm UV fused silica right angle prism	Thorlabs Inc	PS608
1" UV enhanced aluminium planar mirror	Thorlabs Inc	PF10-03-F01
$f = 500$ mm UV fused silica plano-convex lens	Thorlabs Inc	LA4184
Gate valve with pneumatic actuator	VAT Vacuum Valves AG	10844-CE44
Even-Lavie valve heater PID	West Instruments	N2300

Acknowledgements

Thanks to the ERC for my funding and to Jan for his excellent supervision, investing generously in me and stretching me in my development. Thanks also to Dr James Bull for his wisdom and experience that so vitally aided the early progress of this project. Thanks to Cate Anstöter for generously spending many hours on the DFT and TD-DFT calculations that supported the experimental results. Thanks to Paul, Neil, Bryan and Kelvin in the workshops for their labour, tirelessly, diligently and skilfully working to complete the relentless stream of requests with which I have bombarded them! And to my loving wife Jo. Your support, encouragement and selfless patience have been a constant comfort and delight to me. Soli Deo Gloria.